ELECTROLYSIS OF COAL AND CARBON SLURRY SUSPENSIONS

by

MOUSTAFA REDA ABOUSHABANA

Presented to the Faculty of the Graduate School of
The University of Texas at Arlington in Partial Fulfillment
of the Requirements
for the Degree of

DOCTOR OF PHILOSOPHY

THE UNIVERSITY OF TEXAS AT ARLINGTON
December 2012

ACKNOWLEDGEMENTS

I would like to express my sincere appreciation to my research advisor Professor Krishnan Rajeshwar for his unwavering confidence in my abilities, intelligent guidance and continuous support. He has provided me tremendous knowledge and valuable advice and has been an excellent source of motivation during the entire research work. I would like to add that I felt him as a great leader rather than as a boss in every situation during my dissertation study.

I would like also to acknowledge my dissertation committee members, Prof. Frederick MacDonnell and Prof. Richard Timmons, for devoting their time and effort and giving important suggestions to improve the quality of my research work.

My special thanks go to Professor Norma Tacconi for training me in the coal project shortly after joining the group, giving me warm-hearted encouragement, friendly help, and fruitful discussions during my research. Thanks to Dr. Wilaiwan Chanmanee for acquainting me with the experimental instrumentation and Dr. Csaba Janaky for his valuable discussions and advice especially at the last part of my research work. I also thank all the members of our research group for their support.

I sincerely thank my wife, Mrs. Rasha Yousef, for her endless love and support that helped me to overcome all the difficult situations during my course work and dissertation study. Special thanks to her for sacrificing her career advance, taking care of our kids, Karim, Menatalla and Ahmad and helping them growing so healthy and lovely. I am proud of and thankful for all my family members for providing me with warm and quiet environment that helped me to concentrate on my research.

Finally, I thank the Department of Chemistry & Biochemistry and the Center for Renewable Energy Science & Technology (CREST) laboratory, and the University of Texas at Arlington, for giving me this opportunity and for financial support during this dissertation study.

December 4, 2012

ABSTRACT

ELECTROLYSIS OF COAL AND CARBON SLURRY SUSPENSIONS

Moustafa Reda Aboushabana, PhD

The University of Texas at Arlington, 2012

Supervising Professor: Krishnan Rajeshwar

In this dissertation study, different ranks of coal and carbons were tested as anode depolarizers in a three electrode electrochemical cell designed for hydrogen generation. The focus of this study was mainly Texas lignite coal (TXLC). For comparison purposes, other coals were carefully chosen to cover the range from high-rank, intermediate-rank, and to low-rank (TXLC). Carbon blacks and carbon nanotubes were also studied to gain more insight into the mechanistic aspects of the electrolysis process.

The $Fe^{3+/2+}$ redox couple was used as an oxidation mediator throughout the study. It shuttles the electrons between the coal or carbon particles and the anode surface. A standard reduction potential of 0.76 V explains the ability of Fe^{3+} species to (partially) oxidize the bulk carbon phase as well as the surface functional groups of coal and carbons. In addition, the Fe^{+2} species can be anodically regenerated at a low potential (0.8 V), that is much lower than the oxygen evolution potential. Finally, It is recognized that these species exist as aqua complexes in solution, and among the Fe^{3+} species, the dominant photoactive complex is the 6-coordinated $Fe (OH) (H_2O)_5^{2+}$ complex. The photoactivity of the $Fe(OH)(H_2O)_5^{2+}$ complex allowed the use of light as a mechanistic probe of photoelectrolysis of coal and carbons.

In the photoelectrolysis of aqueous lignite coal and carbon black slurry suspensions, UV irradiation of the anolyte in the presence of iron species, afforded enhanced currents associated with the free radical-induced oxidative attack of the coal (or carbon) surface. Useful mechanistic insights were gleaned into the factors responsible for the anode depolarization by the coal (or carbon) particles in the slurry suspension. According to a photo-Fenton-like mechanism, UV light was used to modulate chemical reactions in the solution phase generating very reactive $^{\bullet}OH$ and other reactive oxygen species (ROS) that oxidatively attack the coal matrix. It was found that the hydroxyl radicals ($^{\bullet}OH$) and the ROS photogenerated via this mechanism can enhance hydrogen production in the cathode compartment of a coal photoelectrolysis cell. GC analyses of the evolved gases in the anolyte compartment revealed the gradual increase in the amount of CO_2. Infrared (IR) spectrophotometric analysis of the samples before and after UV irradiation (in the presence of $Fe^{2+/3+}$) showed an overall increase in the surface oxygen groups and a decrease in aromaticity. These data trends are consistent with an attack of the coal matrix by the photogenerated $^{\bullet}OH$ species and other ROS. Two carbon black samples were included in this study for comparative purposes: (a) to assess the effect of oxidizability of the carbon matrix (relative to lignite coal); and (b) to examine the influence of graphitization of the carbon black on its ease of oxidation.

The consequences of chemical pre-treatment of coals of varying rank and selected carbon black samples, on their ability to generate hydrogen in an electrolytic environment were explored. Concurrently, thermal analyses (differential scanning calorimetry or DSC and thermogravimetry or TGA) were performed on these pre-treated samples to investigate the consequences in terms of corresponding alterations in thermal reactivity. The chemical pre-treatment consisted of digestion with strong acid (1 M each of $HClO_4$, H_2SO_4, or HNO_3) or by stirring the coal (or carbon black) sample with 35 % H_2O_2 overnight. The influence of H_2O_2 pre-treatment was shown to be critically dependent on the coal rank. Further, coal samples responded differently relative to carbon black surfaces in terms of how the hydrogen-generating capacity and thermal reactivity were altered by either acid or H_2O_2 pre-treatment.

The improvement of the chemical reactivity of coal samples following chemical pre-treatment was attributed to changes in surface area and surface oxygen functional groups. The surface area of coal particles was measured (via nitrogen adsorption and the BET model) before and after treatment. The surface and bulk oxygen functional groups were investigated by X-ray photoelectron spectroscopy (XPS) and IR analysis, respectively. The results showed an appreciable increase in the oxygen functional groups, specifically the carbonyl groups following the acid and H_2O_2 treatments. Multiwalled carbon nanotubes (MWCNTs) were included in the oxidation treatment to assess which oxygen functional group was responsible for the improvement of coal reactivity. Potassium permanganate ($KMnO_4$), which is a more powerful oxidizing agent than H_2O_2, was used to ensure complete oxidation of the chemically inert MWCNTs. The XPS and IR data showed a specific increase in the hydroxyl rather than the carbonyl groups. The complete absence of any improvement in the chemical and electrochemical reactivity of MWCNTs following the oxidation treatment ruled out any contribution from the hydroxyl groups to the improved reactivity of chemically pretreated coal.

Finally, economic analysis of hydrogen production by coal (dark and photo) electrolysis was performed. The analysis aimed at carrying out a sensitivity analysis that addresses the influence of variation of main system components (e.g., electricity price, operating potential, and process efficiency) on the hydrogen production cost. Economic barriers associated with the commercial application of coal electrolysis for hydrogen production were also addressed.

TABLE OF CONTENTS

LIST OF ILLUSTRATIONS

LIST OF TABLES

CHAPTER 1

INTRODUCTION

1.1 Coal Electrolysis

Coal is an intermediate solution to our ever-expanding energy needs owing to its abundance in many parts of the world and the low cost of electricity generation from it. Currently it produces about 50% of the world's electricity needs. Nine out of ten tonnes of the coal mined in the United States today are used to generate electricity. Combustion of coal is used to generate electricity with the well-known disadvantages of harmful emissions and environmental pollution. On the other hand, steam reforming of coal is a cleaner approach for extracting the stored energy (than burning it), and has long been used for hydrogen and liquid fuels production.[1,2]

An alternate approach, namely, electrolysis of coal suspensions to generate hydrogen, was originally proposed in 1979[3] and has been intensely studied in the years since.[4–22] A major advantage of this process, relative to steam reforming, is that it requires only mild temperatures and ambient pressure and produces pure streams of hydrogen and carbon dioxide. The process looks promising specially under the unprecedented constrains posed on the coal conversion processes and the urgent need for carbon dioxide emission control.[23] In other words, the modern coal conversion technologies need to find efficient ways of extracting the energy stored in coal without contributing to the greenhouse pool.

Compared to coal which is a primary source of energy, hydrogen is an energy carrier and can be considered as one of the cleanest forms of energy. The energy stored in its chemical bonds is released when hydrogen combines with oxygen to produce water as a reaction product. Hydrogen can be used in different scenarios. Almost half of the hydrogen produced globally is used for ammonia production. Refineries use the second largest part of hydrogen for chemical conversion processes such as converting heavy hydrocarbons into gasoline and diesel fuel.[24] In fuel cells, however, hydrogen is used as a fuel to produce direct current electricity.

Steam methane reforming (SMR) is the most widely used and most economical process for producing hydrogen. Although SMR is a complex process involving many different catalytic steps that produce carbon monoxide and carbon dioxide, the primary greenhouse gases, it will continue to be the technology of choice for the mass production of hydrogen until another more environmentally friendly and cost effective technology is developed.

Coal electrolysis, as an alternative way of producing hydrogen, has a lot of mechanistic aspects that are still incompletely understood due to the complexity of coal structure and its components. The different behavior of coal described in the literature may reside with the unique nature of coal structure which is mainly determined by its plant origin and the conditions of its formation.

1.2 Coal Structure and Ranks

1.2.1 Macromolecular structure

Coal is characterized by an extensive network of pores that renders it unique between the other fossil fuels. Such a network facilitates the accessibility of reactant molecules to the organic matter of coal as a result of an appreciable volume of pore and increased surface area. The mass transfer of reactant molecules across the pores network is of great consideration in coal reactivity. Figure 1.1 shows the major constituents in coal structure, namely, organic matter, fragments of plant debris (macerals), inorganic inclusions and an extensive pore network. The organic matter represents almost 85-90% (w/w) of dry coal and differs from one sample to the other according to the precursor plant material. The inorganic content of dry coal represents the remaining 5-15% and is mainly composed of aluminosilicates and pyrites. As the organic matter dominates the coal structure, the nature of functional groups, especially the oxygen functional groups, have a great influence on coal reactivity.[25]

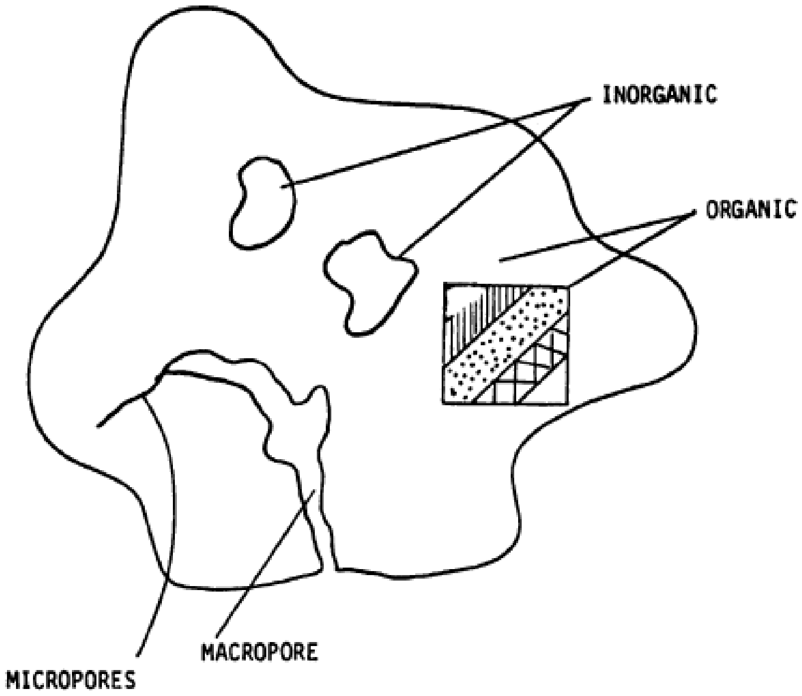

Figure 1.1 Diagram showing the macromolecular coal structure.[25]

1.2.2 Chemical structure

The atomic hydrogen-to-carbon ratio in coal is 0.9. It is roughly half that of petroleum and oil shale and shows that coal is hydrogen deficient. Compared to petroleum, coal has a very different chemical structure, with higher levels of aromatic and other unsaturated species. Being solid, coal has a high molecular weight, much higher than that of natural gas or petroleum. Coal is somewhat similar to polymers (main constituents of plastics); a typical structure is illustrated below in Figure 1.2.

A second dominant feature is the high level of organic oxygen in coal, one oxygen for every five carbon atoms, more than 10 times the oxygen levels in petroleum. These abundant oxygen forms strongly influence coal's structure and reactivity. Oxygen occurs mainly as phenolic or ether groups. Carboxylic and carbonyl groups are less predominant.[26] Nitrogen exists primarily as pyridine or pyrrolic type rings.

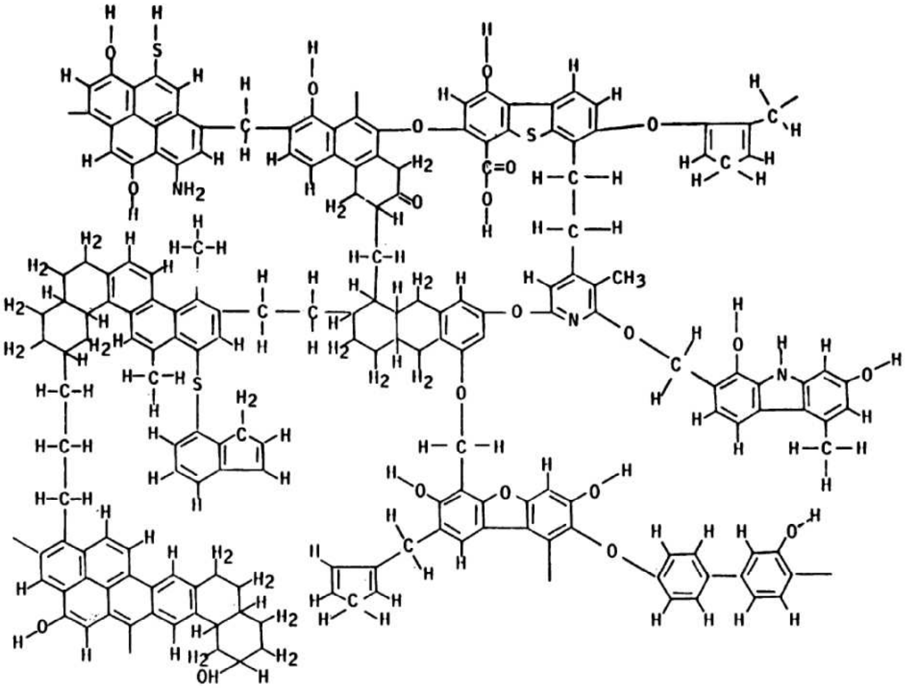

Figure 1.2 The primary chemical groups in a bituminous coal (as proposed by Wiser).[25]

1.2.3 Coal ranks

Coal is classified into four general categories or "ranks." They range from lignite through sub-bituminous and bituminous to anthracite, reflecting the progressive response of individual deposits of coal to increasing heat and pressure. The amount of energy stored per unit mass of coal as well as its heating value depends mainly on its carbon content, but other factors also influence. The amount of energy in coal is expressed in either British thermal units per pound (Btu/lb) or KJ/kg. A Btu is the amount of heat required to raise the temperature of one pound of water by one degree Fahrenheit. About 90 percent of the coal in the U.S. falls in the bituminous and sub-bituminous categories, which are lower in rank than anthracite and mostly contain less energy per unit mass. Bituminous coal dominates in the Eastern and Mid-continent coal fields, while sub-bituminous coal is generally found in the western part of the U.S. and Alaska.[27]

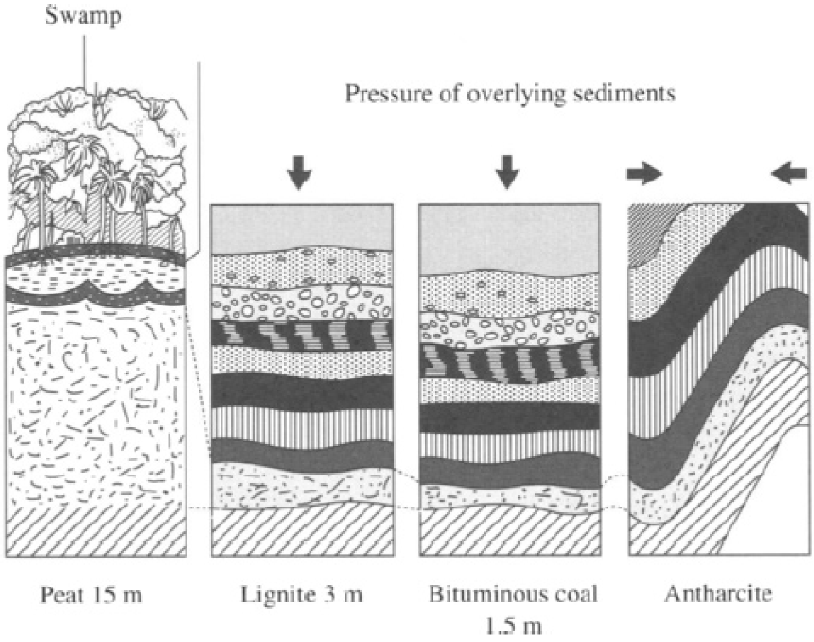

Figure 1.3 Stepwise formation of different coal ranks from peat. [28]

Lignite ranks the lowest and is the youngest of the coals. Most lignite is mined in Texas, but large deposits are also found in Montana, North Dakota, and some Gulf Coast states. Lignite, sometimes called brown coal, has the lowest carbon content and heat value. It is mainly used for electric power generation.

Table 1.1 shows the different ranks of coal which have been classified according to their carbon content and heating value. The elementary composition changes with increasing coal rank. The carbon content, amounting to roughly 71 wt% in lignite, increases to more than 92 wt% in anthracite, whereas hydrogen, initially at 5 wt%, drops to below 3 wt%, and oxygen, initially at 22 wt% drops to 2 wt%. The aromatic carbon content increases with increasing the rank.[26] The changing elementary composition is also reflected in the carbon / hydrogen ratio, which is approximately 14% for lignite and increases to more than 45% for anthracite.

Table 1.1 Classification of Coal by Rank[28]

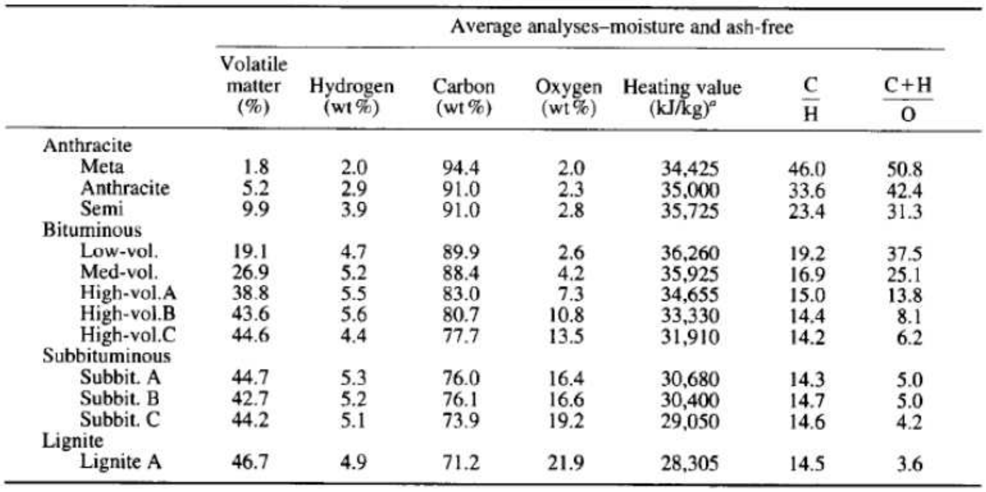

	Average analyses–moisture and ash-free						
	Volatile matter (%)	Hydrogen (wt%)	Carbon (wt%)	Oxygen (wt%)	Heating value (kJ/kg)[a]	$\frac{C}{H}$	$\frac{C+H}{O}$
Anthracite							
Meta	1.8	2.0	94.4	2.0	34,425	46.0	50.8
Anthracite	5.2	2.9	91.0	2.3	35,000	33.6	42.4
Semi	9.9	3.9	91.0	2.8	35,725	23.4	31.3
Bituminous							
Low-vol.	19.1	4.7	89.9	2.6	36,260	19.2	37.5
Med-vol.	26.9	5.2	88.4	4.2	35,925	16.9	25.1
High-vol.A	38.8	5.5	83.0	7.3	34,655	15.0	13.8
High-vol.B	43.6	5.6	80.7	10.8	33,330	14.4	8.1
High-vol.C	44.6	4.4	77.7	13.5	31,910	14.2	6.2
Subbituminous							
Subbit. A	44.7	5.3	76.0	16.4	30,680	14.3	5.0
Subbit. B	42.7	5.2	76.1	16.6	30,400	14.7	5.0
Subbit. C	44.2	5.1	73.9	19.2	29,050	14.6	4.2
Lignite							
Lignite A	46.7	4.9	71.2	21.9	28,305	14.5	3.6

[a] To convert kJ/kg to Btu/lb, divide by 2.326.

1.3 Electrocatalysis of Coal Oxidation

Consensus has emerged that electrooxidation of the coal surface involves reversible (or quasi-reversible) redox mediators such as $Fe^{3+/2+}$ that are already present in the coal matrix.[13,14] The iron redox mediator shuttles electrons between coal and the anode surface where the coal surface is getting oxidized by iron(III) ions and the resulting iron(II) ions are oxidized at the electrode surface.

An undoubtedly over-simplified scheme for the chemical and electrochemical processes taking place during coal electrolysis is as follows where the coal is simply represented as C(s) and the oxidized surface of it is denoted as $C_{(ox)}$(s):

At the anode:

$$Fe^{2+} \rightarrow Fe^{3+} + e$$

$$C(s) + 2H_2O(l) \rightarrow CO_2(g) + 4H^+ + 4e$$

In solution:[29]

$$Fe^{3+} + C(s) + mH_2O(l) \rightarrow [C_{(ox)}(s), CO_2(g), CO(g)] + 2mH^+ + Fe^{2+}$$

At the cathode:

$$2H^+ + 2e \rightarrow H_2(g)$$

Several redox mediators have been deliberately added to the suspension such as $V^{5+/3+}$, $Mn^{3+/2+,}$ $Ce^{4+/3+}$, $Fe^{3+/2+}$, I^{3-}/I^-, and $Fe(CN)_6^{3-/4-}$ by previous researchers.[6,30] The redox catalyst is mainly aimed at having as low a standard electrode potential as possible which would still oxidize coal at a fast rate. This redox pair must be completely soluble in aqueous acid solutions and must have a relatively large heterogeneous electron transfer rate constant.[30] A tradeoff exists between the rate of the catalytic reaction and the operating potential required for coal electrolysis. Redox mediators with relatively high standard reduction potential show faster reaction rates with coal at the expense of higher applied potential that is needed for electrolysis.[30]

For this study we opted to use the $Fe^{3+/2+}$ redox couple as an oxidation mediator. The rationale for this choice was the ability of Fe^{3+} species to (partially) oxidize the bulk carbon phase as well as the surface functional groups of coal. In addition, it can be anodically regenerated at a low potential (0.8 V), much lower than the oxygen evolution reaction. Finally, Fe(II) / Fe(III) species are soluble in water and in acidic solutions and chemically stable over a long period of time under normal storage conditions.

1.4 Controlled Current Techniques

Chronopotentiometry (CP), the most basic constant current experiment, involves the application of a current step across an electrochemical cell while the potential response of the cell is monitored as a function of time (Figure.1.4). The change in potential as a response to the current step is controlled by the change of concentration profiles of the redox species with time.[31]

Consider the electron transfer reaction:

$$O + e \rightarrow R$$

Prior to the application of the current step, the concentration of the electroactive oxidized species (O) is the same everywhere i.e. the electrode surface concentration and the bulk concentration of (O) are equal. The initially measured potential is then the open circuit potential which depends mainly on the standard reduction potential of the redox pair and obeys the Nernst equation:

$$E = E^{\acute{o}} + \frac{0.059}{n} \log \frac{C_O}{C_R}$$

where C_O and C_R are the surface concentration of (O) and (R), respectively.

Once the (reducing) current step is applied, electrochemical reduction of (O) into (R) takes place to support the applied current. Consequently, the concentration of (O) at the electrode surface decreases while the concentration of (R) at the electrode surface increases. This sets up a concentration gradient for both (O) and (R) between the bulk solution and the

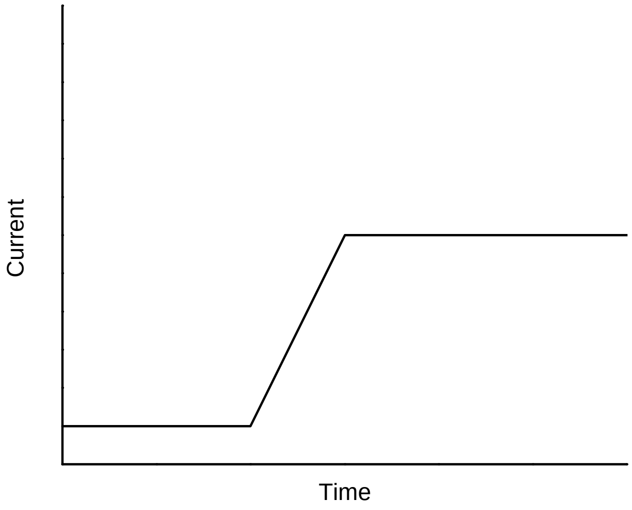

Figure.1.4 Current excitation step in chronopotentiometry.

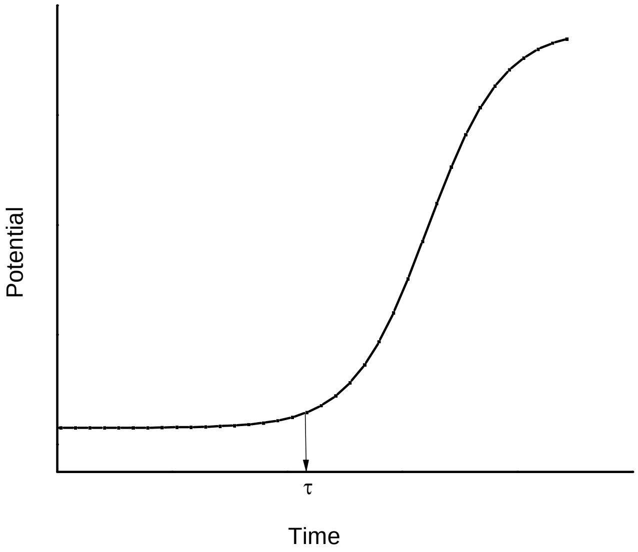

Figure.1.5 Potential change response in chronopotentiometry.

electrode. As the concentrations of both (O) and (R) vary with time, so do the potential. Actually, as long as the concentration of (O) does not reach zero at the electrode surface, the value of the potential will be more or less around the formal potential of the redox pair as shown in the initial part of the potential-time plot (Figure 1.5). Once the concentration of (O) at the electrode surface becomes zero as a result of electrochemical reduction (Figure 1.6), the applied current can no longer be supported by this electron transfer reaction, so the potential changes to the redox potential of another electron transfer reaction. Provided that no other electroactive species exists in solution, an electron transfer reaction with the electrolyte will take place resulting in a large change in the potential. This is indicated as a sharp inflection from low to high value on the potential-time curve (Figure 1.5).

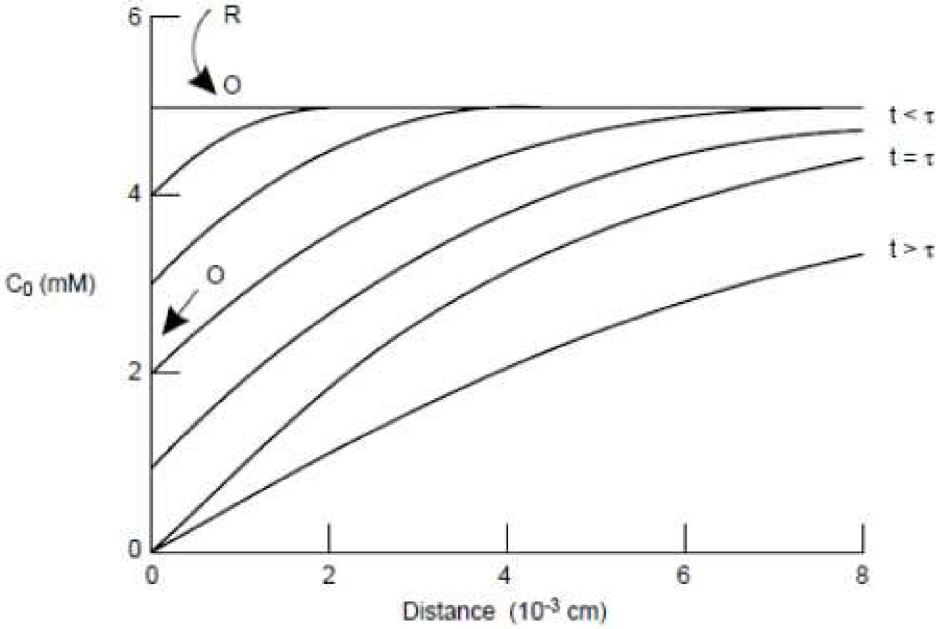

Figure 1.6 Concentration-distance profiles for the electrochemical reduction of (O) to (R) under the effect of a constant current step.[31]

The time (τ) required for the concentration of (O) at the electrode surface to reach zero depends upon the value of the applied current step (i) and decreases as (i) is increased. Sand□s equation defines the quantitative relationship between (i) and (τ):

$$i\tau^{\frac{1}{2}} = \frac{nFACD^{\frac{1}{2}}\pi^{\frac{1}{2}}}{2}$$

n: number of electrons transferred in the electrochemical reaction

F: Faraday's constant = 96,485.3365 C/mol.

C: bulk concentration of electroactive species

D: diffusion coefficient of electroactive species

Whenever the excitation current step is kept constant, the square root of electrolysis time (τ) varies with the bulk concentration of the electroactive species for the same electrochemical reaction.

One advantage of CP measurements is avoiding the interference from the charging current which normally develops as a result of potential changes during the experiment. The magnitude of the charging current is not constant and goes up with higher rates of change in potential. This reduces the amount of current available for the Faradic reaction and renders the measurement less reliable. Since the potential stays almost constant and centered around the formal potential value of the electroactive species and does not change abruptly except at the end of the CP experiment, the adverse effect of the charging current on the measurement is almost cancelled

Another advantage of CP measurements is that the electrolysis time (τ) is independent of the form of diffusion to the electrode surface, as the Sand equation holds for both spherical and planar electrodes.

Finally the CP experiments are well suited for studying and characterizing the electrode reaction. Studying the variation of the ($i\tau^{\frac{1}{2}}$) parameter with the excitation current step (i) helps in drawing a conclusion about the nature of the electrode reaction.

For a catalytic reaction such as the iron mediated coal electrolysis, $(i\tau^{\frac{1}{2}})$ varies with (i) in a specific way. The value of the chemical reaction rate constant will have a noticeable effect on the $i\tau^{\frac{1}{2}}$ value whenever the electrochemical reaction is run at sufficiently low current value. As the current value become higher and higher, the $i\tau^{\frac{1}{2}}$ value will depend only on the surface concentration of the electroactive species and follow Sand equation. In other words, if the rate constant of the chemical reaction is very small, its effect on $i\tau^{\frac{1}{2}}$ value can be neglected. For all the advantages mentioned above, the coal electrolysis reaction was studied under galvanostatic conditions.

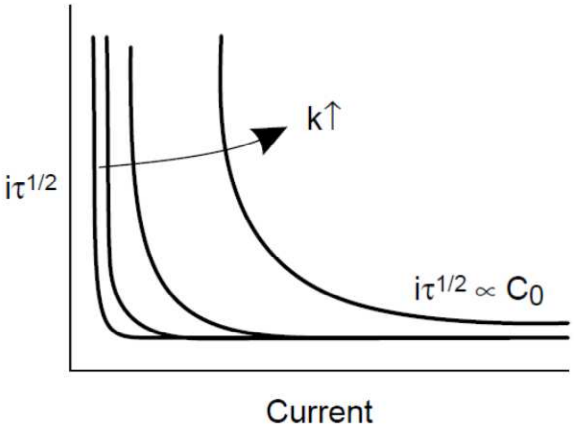

Figure 1.7 Variation of $(i\tau^{\frac{1}{2}})$ with (i) for Catalytic Reaction[31]

1.5 Thermal Analysis Techniques

The term thermal analysis (TA) is frequently used for analytical techniques that describe the behavior of a sample as a function of temperature and involve differential scanning calorimetry (DSC), differential thermal analysis (DTA), thermogravimetry (TGA), thermo-mechanical analysis (TMA) and dynamic mechanical analysis (DMA).[32]

Here we will focus mainly on the TGA and DSC experiments as they are the ones that would be extensively applied during this study. While TGA measures the change in the mass of

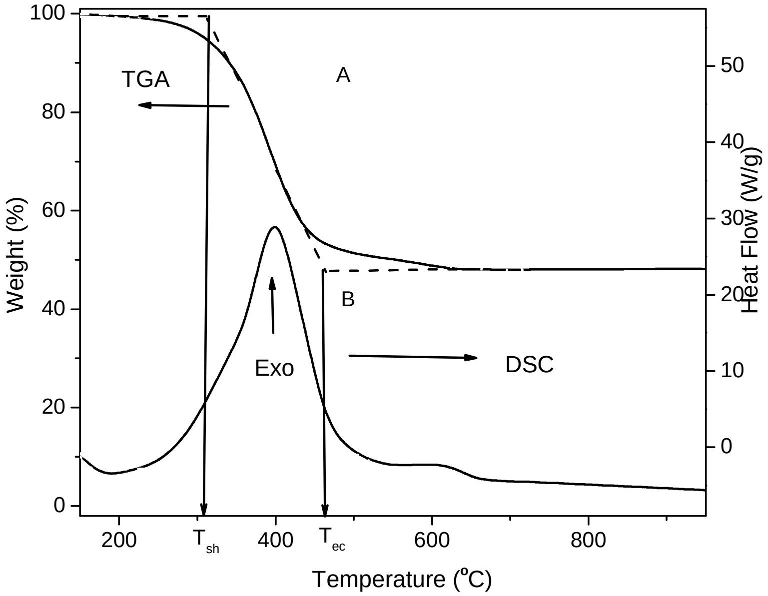

Figure 1.8 Typical thermogravimetric and differential scanning calorimetry curves.

the sample as it is heated (Figure 1.8), DSC measures the energy changes that occur as a sample is heated together with the temperature at which these changes occur. TGA examines the mass change of a sample in one of two modes, the scanning mode, where the mass change is recorded as a function of temperature and the isothermal mode, where the mass change is studied as a function of time. While some thermal events cause a change in the mass of the sample such as desorption, absorption, sublimation, vaporization, oxidation, reduction and decomposition, others do not, such as melting, crystallization and glass transition. The experimental conditions employed during TGA runs have a profound effect on the mass change characteristics of a material. Factors such as sample mass, volume and physical form, the shape and nature of the sample holder, the nature and pressure of the atmosphere in the sample chamber and the scanning rate all have great influence on the characteristics of the recorded TGA curve.

TGA is not a black box technique and hence establishing the optimum conditions for analysis is essential for reliable results. The experimental conditions should be recorded and maintained within a given series of samples, so that curves from different experiments can be compared in a meaningful way.

TGA curves are normally plotted with the mass change percentage on the y-axis and temperature (T) or time (t) on the x-axis. A one-stage reaction process recorded in the scanning mode is shown in Figure 1.8(A). The reaction is characterized by two temperatures, T_i sometimes called T_{sh} (temperature of self-heating) and T_f or T_{ec} (end of combustion temperature). T_{sh} is the lowest temperature at which the onset of a mass change starts. Similarly, T_{ec} is the lowest temperature at which the mass change process is completed.

The data gleaned from the normal TGA run depends on the shape of the curve. Figure 1.9 shows seven main categories of TGA curves. Type (A) curves show no mass change over the entire temperature range of the experiment. This takes place when the decomposition temperature of the material is greater than the maximum temperature of the experiment. In such a case, DSC can be used to look for non-mass-changing processes. Type B curves show large initial mass loss followed by a mass plateau. This behavior normally corresponds to the evaporation of volatile components, drying and desorption processes. The third category, type C, is a single-stage decomposition reaction where the decomposition temperatures (T_{sh} and T_{ec}) are used to characterize the curve. Type D curves mark multi-stage decomposition processes when the reaction steps are easily resolved. Type E curves, on the other hand, show up whenever the individual reaction steps are not well resolved. In such a case the DTG (differential TGA) experiments are often preferred as the characteristic temperatures can be determined more accurately. Surface oxidation in the presence of an interacting atmosphere leads to a mass increase as shown in type F curve. The final category, type G, takes place when surface oxidation is followed by decomposition of the reaction products.

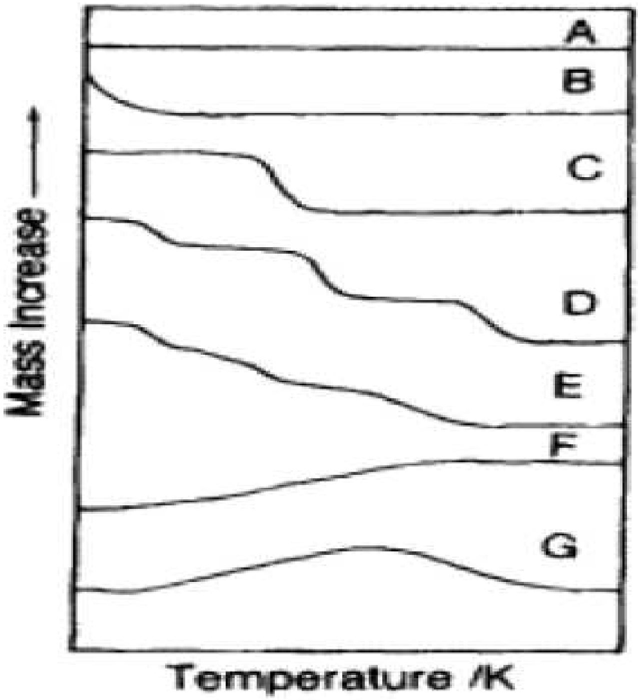

Figure 1.9 Classification of TGA curves.[32]

In quantitative DSC, the temperature difference between the sample and reference is measured as a function of temperature or time, under controlled temperature conditions. The temperature difference is proportional to the change in the heat flux. In other words, the main property that is measured by DSC is heat flow, the flow of energy into or out of the sample as a function of temperature or time. The unit used is W/g of sample on the y-axis (Figure 1.8 B). Since W has units of J/s this is literally the flow of energy in unit time. The actual value of heat flow measured is not absolute and depends largely on the effect of the reference. It is very important that a stable baseline is obtained so that any changes can be measured. The starting point of the curve on the y-axis should be set at or close to zero.

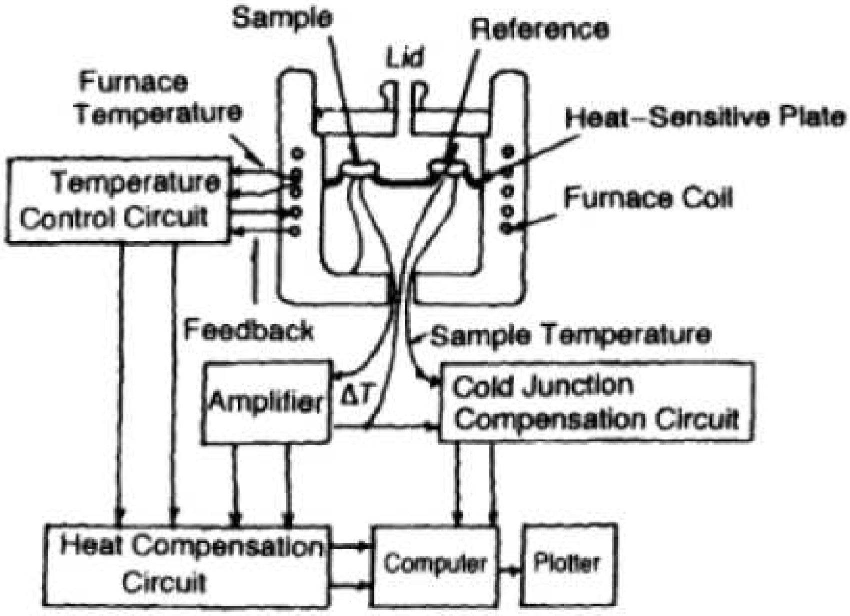

Figure 1.10 Schematic diagram of a differential scanning calorimetry instrument.[32]

1.6 Spectroscopic Techniques

1.6.1 Infrared spectroscopy

Infrared (IR) spectroscopy is a technique based on the vibrations of the atoms of a molecule. An IR radiation is normally passed through the sample to determine what fraction of the incident radiation is absorbed at a particular energy. The energy at which any peak in an absorption spectrum appears corresponds to the frequency of a vibration of a part of a sample molecule. Depending on the choice of the sampling technique a variety of samples can be analyzed. Liquids, solutions, pastes, powders, films, fibers, gases and surfaces can all be analyzed.[33]

The introduction of Fourier-transform spectrometers was one of the most important advances in IR spectroscopy. The mathematical process of Fourier transformation has dramatically improved the quality of infrared spectra and has minimized the time required for data acquisition.

The selection rule for IR spectroscopy is that the electric dipole moment of the molecule must change during the vibration to show infrared absorptions. The larger this change, the more intense will be the absorption band. A molecule can only absorb radiation when the incident IR radiation has the same frequency as one of the fundamental modes of vibration of the molecule. This leads to increasing the vibrational motion of a small part of the molecule rather than the entire molecule. An understanding of molecular symmetry and group theory is crucial for assigning IR bands.

The interpretation of IR spectra is not that easy and may be complicated by a number of factors. These factors involve overtone, combination bands, Fermi resonance and coupling. They should be taken into account when looking at spectra as they can result in important changes and misinterpretation of bands. Fourier transform IR (FTIR) spectroscopy is very useful in probing the functional groups in coal and thus provides additional insight into coal structure. For complex heterogeneous structures like coal, band assignments should be based on comparison with standard patterns reported in the literature.

1.6.2 Raman spectroscopy

Raman spectroscopy uses a single frequency laser radiation to irradiate the sample. The radiation scattered from the molecule, one vibrational unit of energy different from the incident beam is measured. Thus, unlike infrared absorption, the energy difference between the ground and excited states in Raman scattering does not need to match the energy of incident radiation. The basic selection rule for intense Raman scattering is that the vibrations should cause a change in the polarizability of the electron cloud around the molecule. The largest changes and the greatest scattering usually results from symmetric vibrations. In infrared absorption, on the other hand, the most intense absorption is caused by asymmetric vibrations.[34]

Infrared and Raman spectroscopies are often complementary and usually used together to give a better view of the vibrational structure of a molecule. Raman scattering is normally expressed as a shift in energy from that of the exciting radiation and is often expressed in cm^{-1} units. The most interesting features lie in the 3600-200 cm^{-1} range.[34]

Raman spectroscopy has been extensively used to obtain information about the degree of ordering and crystallinity in carbonaceous materials. Raman bands, mainly the G (graphite) and D (defect) bands at 1582 cm^{-1}and 1357 cm^{-1}, respectively, can provide such information. The D band represents sp^3 bonds (tetrahedral configurations) or it may represent disorder in hybridized sp^2 bonds (graphene edge configurations). G band represents sp^2 bonds (planar configurations). The G` mode (2600-2700 cm^{-1}) is the second overtone of the defect-induced D mode (Figure 1.11).[35]

The ratio between the D band and G band is normally used to study the quality of bulk samples.[36] Similar intensity of both bands is an indication of a high quantity of structural defects. More details about the use of Raman spectroscopy to study the effect of different oxidation treatments on multi-walled carbon nanotubes (MWCNT) will be given in Chapter 4.

1.6.3 X-ray photoelectron spectroscopy

X-ray photoelectron spectroscopy (XPS), previously known as electron spectroscopy for chemical analysis (ESCA), is widely used to examine the surface of a material in its "as received" state, or after some treatment. XPS is based on the photoelectric effect. The energy of an incident X-ray photon overcomes the binding energy of a core-level electron which is then excited and ejected from the analyte. The kinetic energies of the ejected photoelectrons, are measured by an electron spectrometer (Figure 1.12).[37]

The binding energy of the photoelectron is characteristic of the orbital from which it originates. A wealth of information about the sample can be obtained by analyzing the ejected photoelectrons. A typical XPS spectrum is a plot of the number of electrons detected versus the binding energy of the electrons detected. Each element produces a specific set of XPS peaks at specific binding energies that can be used for its direct identification. Typically, the peaks in the range from 0 eV to ~15eV in binding energy are attributed to valence electrons. The core-level electron ejection appears at higher binding energies.

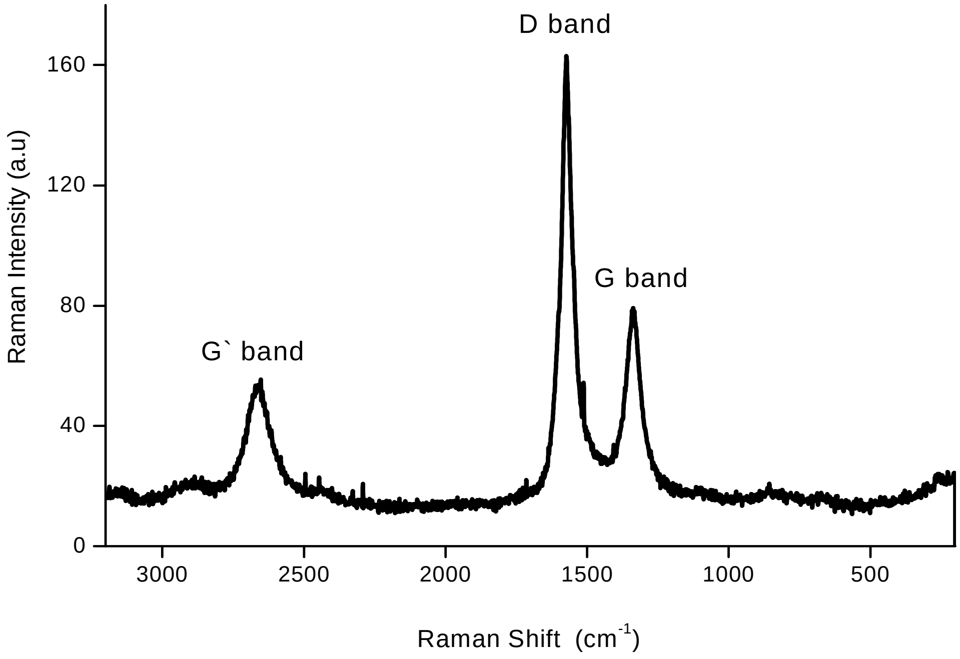

Figure 1.11 Raman spectrum of a multi-walled carbon nanotube (MWCNT) sample.

Qualitative elemental identification for the entire periodic table elements (except H and He) can be achieved. Survey scans are obtained by recording low resolution spectra over a broad binding energy range and aimed at simple identification of elements. Information about the chemical (oxidation) state of elements is commonly carried out by acquisition of high resolution spectra in binding energy regions of interest followed by peak-fitting.

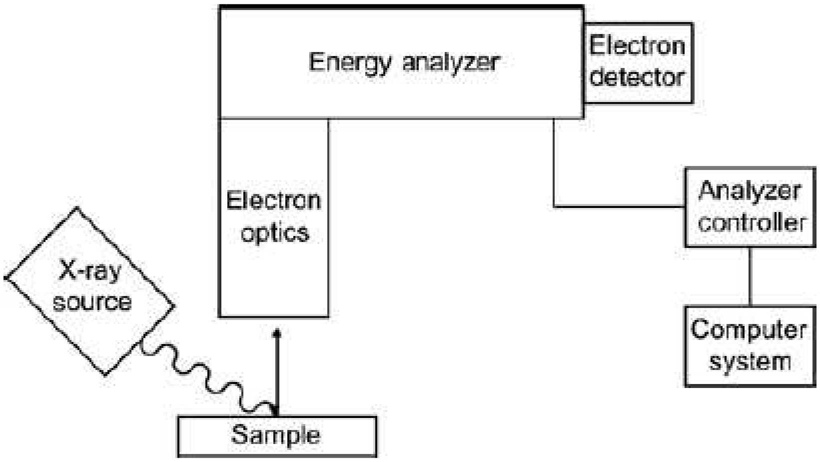

Figure 1.12 Schematic design of an X-ray photoelectron spectrometer.[37]

Atoms of the same element in different chemical states can be identified by XPS. Surrounding species can affect the binding energies of the core electrons; these changes are called “chemical shifts.” and are generally less than 10 eV. Only the photoelectrons produced in the top several nanometers of the sample are observed at their characteristic energies. This corresponds to approximately 10 atomic layers of surface.

CHAPTER 2

PHOTOELECTROLYSIS OF COAL AND CARBON BLACKS

2.1 Literature Review

Fenton's reagent was discovered about 100 years ago, but its application as an oxidizing reagent for destroying toxic organics was not applied until the late 1960s. Fenton reaction processes are known to be very effective in removing water pollutants and converting them completely into CO_2. During Fenton reaction, dissociation of H_2O_2 and the formation of highly reactive hydroxyl radicals takes place with subsequent attack and destruction of the organic pollutants.[38]

Advanced oxidation techniques (AOT) is the general term given to the oxidation processes that involve the generation of radical intermediates. Hydroxyl radicals (oxidation potential: 2.8 V) are so strong oxidizing agents that they can non-specifically oxidize target compounds at high reaction rates (of the order of $10^9\ M^{-1}s^{-1}$).[39] Fenton's oxidation process is one of the most widely applicable AOT. It depends on the use of a mixture of H_2O_2 and ferrous iron to generate hydroxyl radicals according to the reaction

$$Fe^{2+} + H_2O_2 \rightarrow Fe^{3+} + OH^{\bullet} + OH^{-}$$

The decomposition of H_2O_2 is catalyzed by the ferrous iron (Fe^{2+}) to produce hydroxyl radicals. The generation of the radicals involves a complex reaction sequence in an aqueous solution. Walling[40] simplified the overall Fenton chemistry by accounting for the dissociation of water.

$$2Fe^{2+} + H_2O_2 + 2H^{+} \rightarrow 2Fe^{3+} + 2H_2O$$

According to this scheme, the presence of H^+ is required for the decomposition of H_2O_2 and to produce the maximum amount of hydroxyl radicals. Various organic substrates (RH), can be attacked by the hydroxyl radicals. For example, hydroxyl radicals can add to the aromatic or heterocyclic rings (as well as to the unsaturated bonds of alkenes or alkynes). Thus, the Fenton reaction has been lately tested as a potential method for wastewater treatment. [41]

The efficiency of the Fenton process can be improved by combining it with UV light, in the so-called photo-Fenton reaction. The increased efficiency was attributed to the decomposition of the photo-active $Fe(OH)^{2+}$ complex which leads to the production of two hydroxyl radicals for each molecule of H_2O_2 decomposed.[41]

$$Fe(OH)^{2+} + h\nu \rightarrow Fe^{2+} + {}^{\bullet}OH$$

Below, we present the first example of the effects of ultraviolet (UV) illumination on the anolyte in a coal (lignite) electrolysis cell. Since the first report in 1979 on the “electrochemical gasification” of coal water slurry (or coal electrolysis) as a method of hydrogen production, there has been intense interest on this topic. Mechanistically, a consensus has emerged for components leached from the coal matrix into the aqueous medium (e.g., $Fe^{2+/3+}$) that serve as redox mediators to shuttle the electrons between the coal particles and the anode surface. It occurred to us that light can be used as a mechanistic probe of this hypothesis especially given that a photo-Fenton-like mechanism[41] can be used to generate potent free radicals in solution even without an additive such as hydrogen peroxide. We show below that hydroxyl radicals (${}^{\bullet}OH$) and other reactive oxygen species (ROS) photogenerated via this mechanism can enhance hydrogen production in the cathode compartment of a coal photoelectrolysis cell.

Light has been used by previous authors in other scenarios with coal (or carbon) slurries in water.[42–44] Thus UV-irradiated and platinized titanium dioxide (Pt-TiO_2) was used in conjunction with active carbon or lignite to generate H_2, CO_2, and O_2 from aqueous suspensions. The water-gas shift reaction over platinized, powdered TiO_2 was also found by the same research group to be photocatalytic.[44] In all these cases, however, the excitation light activated the oxide semiconductor generating electronic carriers that then influenced electrochemical processes at the particle-solution interfaces. Contrastingly, in the present study, light was used to modulate chemical reactions in the solution phase generating very reactive ${}^{\bullet}OH$ species and other ROS that oxidatively attack the coal matrix.

Two carbon black samples were also included in this study for comparative purposes: (a) to assess the effect of oxidizability of the carbon matrix (relative to lignite coal); and (b) to examine the influence of graphitization of the carbon black on its ease of oxidation.

2.2 Experimental

A sample of lignite for this portion of the dissertation study was obtained from Jewett, Texas, and ground to pass a 200 mesh sieve. Ultimate analysis data for this lignite coal yielded 38.30 % C, 2.75 % H, 11.25 % O, 0.66 % N, 0.90 % S, 30.73 % moisture, and 15.52 % ash. The surface area (as measured via nitrogen adsorption and the BET model) was 3.24 m^2/g, which included 0.82 m^2/g of micropore area and 2.42 m^2/g of external surface area. Two samples of carbon black were obtained from Sid Richardson Carbon & Energy Co (Fort Worth, TX): SRC-401 and SRC-159HN. The latter had been graphitized prior to use by heating at 1800 °C for 1 h followed by treatment with conc. HNO_3 for another hour. These samples had ash contents less than 1.0 % and 0.5 % and surface areas of 59 m^2/g and 260 m^2/g, respectively.

Ferrous sulfate 7-hydrate (AR) and ferric ammonium sulfate 12-hydrate (AR) were from J.T. Baker and Mallinckrodt, respectively. Sulfuric acid was supplied by Alfa Aesar. All chemicals were used as received and all aqueous solutions and slurry suspensions were prepared using de-ionized water.

The custom-designed photoelectrolysis cell had two compartments separated by a fritted glass membrane that prevented metal ions and coal particles from passing to the cathode compartment but yet allowing electrolytic contact between the two compartments. A stainless steel sheet (2.89 cm^2) was used as the working electrode (anode) except for the galvanostatic experiments where a Pt anode (11 cm^2 area) was used. A Pt wire, dipped in 1 M H_2SO_4, was used as a counter electrode. The reference electrode was an Ag/AgCl/3 M NaCl electrode; all potentials below are quoted relative to this reference electrode. The anode compartment was made of quartz to allow UV light from the illumination source to reach the anolyte. The anolyte solution was continuously stirred with a magnetic stirrer to keep the lignite coal or carbon black particles in suspension.

The anolyte was illuminated using an ozone-free 450-1000 W Model 66355 Xe arc lamp (Newport-Oriel). The radiant output of the lamp was 192 mW/cm^2 translating to a photon flux of 4.2 x 10^{17} photons/s.cm^2 over the wavelength range: 250-700 nm. To minimize heating effects from the infrared component of the lamp output, a quartz water filter was placed between the photoelectrolysis cell and the lamp. The water was replaced with an aqueous suspension of coal particles for the blank experiments (see below) to maintain the light flux almost the same as that of the samples.

The reaction mixture contained variable amounts (specified below) of Fe(II) and Fe(III) species dissolved in either 0.01 M or 1 M H_2SO_4. The pH was adjusted to 1.3 using 1 M NaOH. Although the optimum pH for the photo-Fenton-like reaction is known to be in the range: 2-3,[14] the pH was intentionally kept at 1.3 in this study to avoid precipitation of iron (III) hydroxides. The lignite coal and carbon black dose in the slurry suspensions for the galvanostatic experiments was 20 g/L unless otherwise noted (i.e., in the blank experiments where the lignite coal or the black were omitted). A much lower dose of 0.2 g/L was chosen for the experiments with UV irradiation because higher coal or carbon black levels would have otherwise blocked the light from reaching the anolyte bulk.

A CH Instruments Model CHI600C electrochemical analyzer was used for the galvanostatic and voltammetry experiments. To monitor and quantify the amount of CO or CO_2 evolved during the photochemical reaction, a specially designed UV quartz reactor was used.[15] This reactor, as described in detail elsewhere, [45] ensures effective mixing of the suspension, cooling and allows for periodical collection of aliquots for GC analyses. SRI 310C gas chromatograph fitted with a ShinCarbon ST column and a thermal conductivity detector was used for evolved gas analyses. Infrared spectrophotometric analysis of the lignite coal samples was carried out using a Bruker Alpha instrument.

2.3 Results and Discussion

2.3.1 Iron redox and photochemistry

In this study, an externally added $Fe^{2+/3+}$ redox mediator was employed to shuttle the electrons between the anode and the lignite coal (or carbon black) surface.[46] Figure 2.1 contains results from galvanostatic experiments (constant current: 50 mA) for two blank solutions and one test suspension containing lignite coal. Blank 1 was 1 M H_2SO_4 while Blank 2 consisted of 100 mM each of Fe (II) and Fe(III) species dissolved in 1 M H_2SO_4. The test suspension contained in addition lignite coal particles suspended in it. The contrasting chronopotentiometric profiles in Figure 2.1 between Blank 1 on the one hand, and Blank 2 and the test suspension on the other, underline the advantage with the use of coal and $Fe^{2+/3+}$ as anode depolarizers.[7,47,48]

The electrolysis of water can be sustained at a potential as low as ~0.8 V as opposed to the Blank 1 case where the anode potential reaches ~1.8 V to sustain the imposed current flow in the cell.

The upswing in the anode potential at times longer than ~170 min (for Blank 2) and ~250 min for the test suspension diagnoses the saturation of oxidative capacity in the medium, and the potential now moves toward that corresponding to neat water electrolysis to sustain the current flow. Note that the upswing is delayed for the test suspension relative to Blank 2. This trend can be rationalized by the notion that the addition of lignite coal to the medium increases the oxidative capacity relative to the neat $Fe^{2+/3+}$ case, diagnostic of the susceptibility of the lignite coal surface to be oxidized by Fe (III) species in solution.

More germane to this study is what happens when the anolytes are irradiated by the UV light source. The current-potential curves labeled ‘a’ and ‘b’ in Figure 2.2 show the voltammetric behavior for the iron redox solution (with the Fe(II) and Fe(III) concentrations now at 200 mM and 300 mM respectively) in 0.01 M H_2SO_4 “in the dark” and under illumination (for 30 min) respectively. The wave associated with the $Fe^{2+/3+}$ redox couple is markedly enhanced under illumination of the anolyte. This trend is consistent with the net photoconversion of Fe (III) to Fe (II) species that can then be oxidized at the anode.

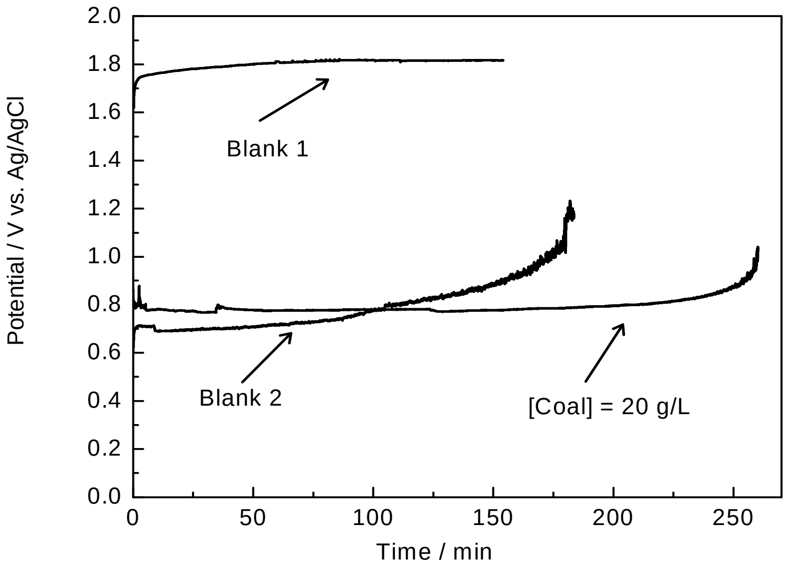

Figure 2.1 Galvanostatic profiles for two blank solutions and a lignite coal suspension with added iron redox mediator.

2.3.2 Experiments with Lignite Coal and Carbon Black

Curves labeled ‘c’ in Figures 2.2A-C show the voltammetric behavior of lignite coal and the two samples of carbon black (SRC-159and SRC-401) in the presence of 200 mM Fe^{2+}/300 mM Fe^{3+}/0.01 M H_2SO_4 and UV illumination. The curves ‘a’ and ‘b’ are the blank runs (see above) reproduced in all the three frames for comparison. Worthy of note are the following trends:

(a) In all the three cases, the onset potentials for the current-potential curves are markedly shifted in the negative direction relative to the blank cases.

(b) The mass transport-limited plateau currents (associated with the $Fe^{2+/3+}$ couple) are significantly enhanced (by ~15%) for the coal suspension case (Figure 2.2A) and ~12% and ~33 % for the two carbon black samples respectively (Figures 2.2B and 2.2C) relative to the irradiated blanks.

(c) Both the onset potential shift and the plateau currents are ordered thus: SRC-401 > lignite coal = SRC-159HN.

Clearly the above trends are rooted in the further conversion of Fe (III) to Fe(II) species in the presence of lignite coal or carbon black in the medium. Another way of mechanistically interpreting these trends is that the (oxidizable) lignite coal or carbon black particles scavenge (intercept) the free radicals generated by the photo-Fenton-like mechanism (see below) before they can oxidize the Fe(II) species to Fe(III) species. The fact that the SRC-401carbon black sample affords a higher plateau current than lignite coal can be rationalized on the basis of both the much higher (oxidizable) carbon content of the black and the higher surface area relative to the (low grade) coal. On the other hand, and interestingly enough, the higher current observed for SRC-401 relative to SRC-159 is not rooted in surface area differences; in fact, SRC-401 has a lower surface are (Experimental section). The structure of the two carbon blacks, i.e., the degree to which the carbon particles are joined in aggregate clusters or chains is also comparable as measured by the oil absorption number (ASTM D2414). Clearly, graphitization of the black surface (as in the SRC-159 case) lowers its susceptibility toward oxidation leading to the observed difference between SRC-401 and SRC-159HN. By extrapolation, the conclusion is inevitable that surface area differences alone cannot account for the (electron transfer) reactivity differences between the lignite coal and the two carbon black samples.

Figure 2.3 contains results showing the effect on plateau current of the illumination time both for Blank 2 (as in curve ‘b’ in Figure 2.2 but for variable times) and for a suspension containing lignite coal in addition. The effect of illumination clearly saturates at times longer than ~20 min beyond which competing effects from back-reactions start to play a balancing role in the current flow. Curve ‘c’ in Figure 2.3 illustrates the temperature evolution in the photoelectrolysis cell as concomitantly monitored in these experiments.

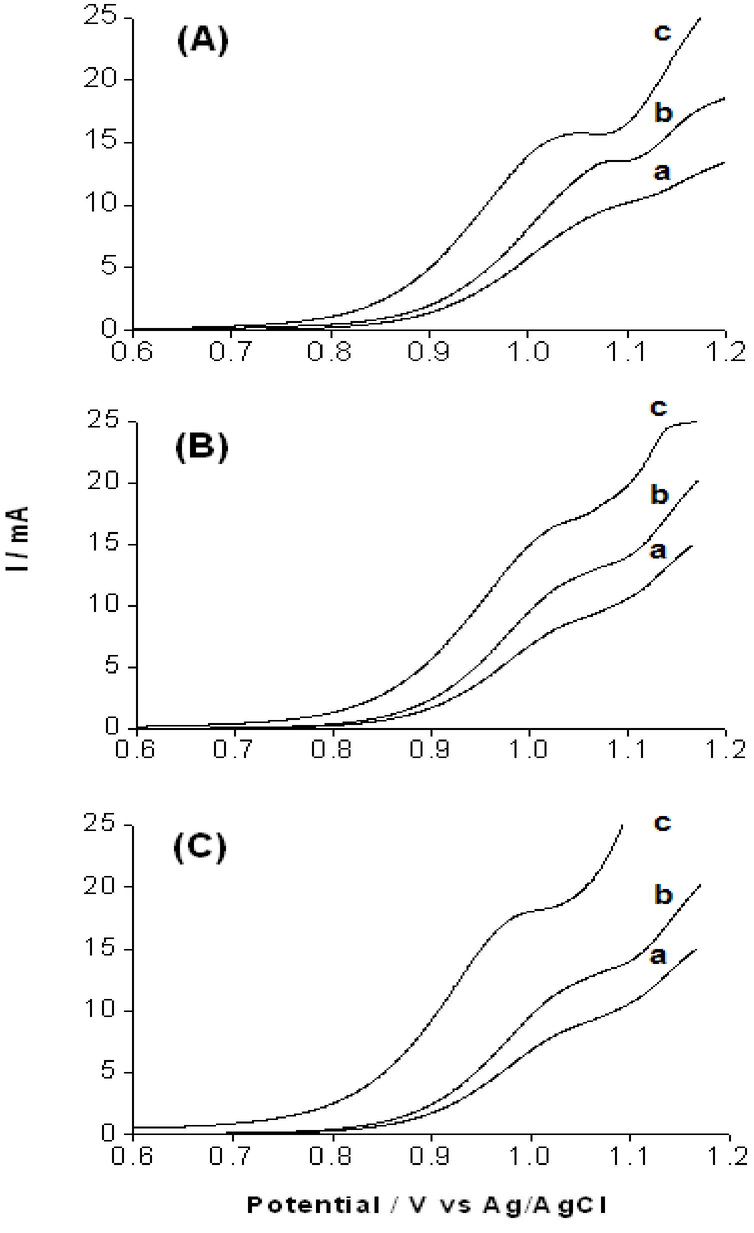

Figure 2.2 Linear sweep voltammograms (potential scan rate: 3 mV/s) for lignite coal (A), SRC-159carbon black (B), and SRC-401 carbon black (C). Refer to text for notation of curves ‘a’, ‘b’, and ‘c’.

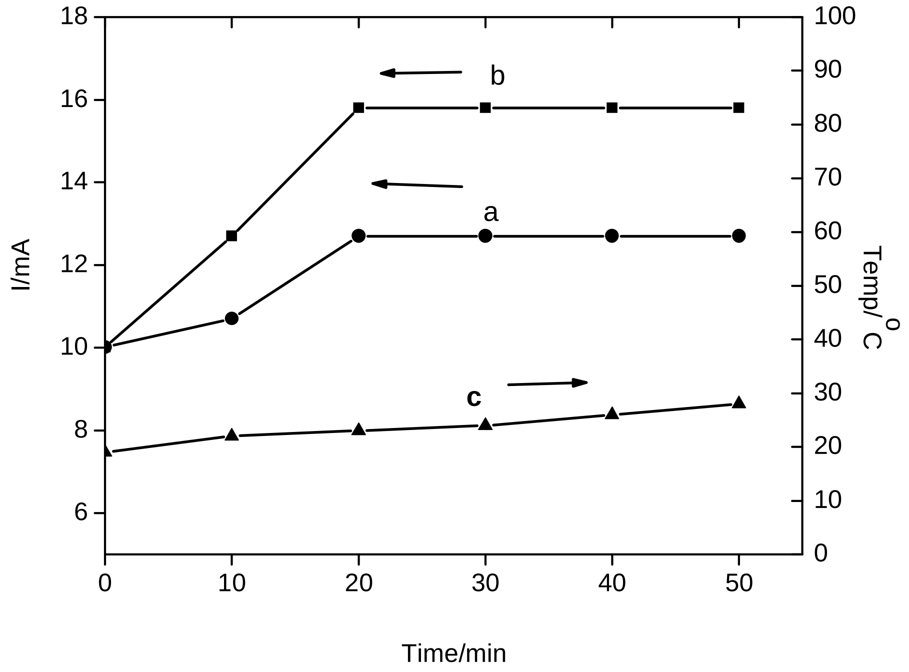

Figure 2.3 Photocurrent-time profiles (measured at 1.10 V, see Figure 2.2) for: (a) 0.2 M Fe(II)+ 0.3 M Fe(III) in 0.01 M H_2SO_4+x min UV irradiation; and (b): a + 0.02 g/mL lignite coal. The temperature changes in the photoelectrolysis cell are mapped in (c).

Clearly, the current enhancements noted above cannot be trivially attributed to anolyte heating (and consequent mass-transport enhancement) as a result of the irradiation.

Finally, the lignite coal sample was subjected to prolonged UV irradiation under comparable chemical conditions as in the photoelectrolysis cell. GC analyses of the evolved gases in the anolyte revealed the gradual increase in the amount of CO_2. After 4 h of illumination, another peak for CO started to appear.

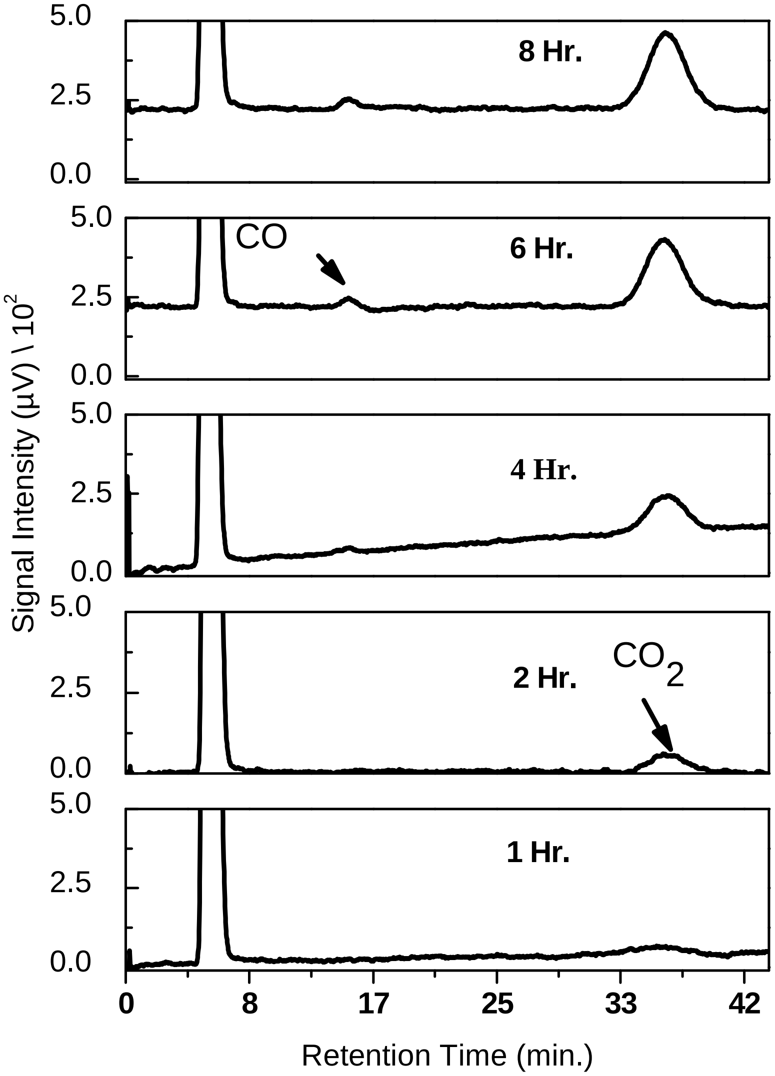

Figure 2.4 GC analysis of the gases evolved during the photochemical oxidation of coal slurry (0.02 g %).

2.3.3 General Discussion

The iron redox species were shown above as Fe^{2+} and Fe^{3+} only for notational convenience. It is recognized that these species exist as aqua complexes in solution, and among the Fe(III) species, the dominant photoactive complex is $Fe(OH)^{2+}$ [strictly, the 6-coordinated $Fe(OH)(H_2O)_5^{2+}$ complex]. On UV irradiation, the following complex chain of reactions takes place according to the photo-Fenton-like mechanism:[49]

$$\mathrm{Fe(OH)}^{2+} + h\upsilon \rightarrow \mathrm{Fe}^{2+} + {}^{\bullet}\mathrm{OH} \qquad (1)$$

$$\mathrm{Fe}^{2+} + {}^{\bullet}\mathrm{OH} \rightarrow \mathrm{Fe(OH)}^{2+} \qquad (2)$$

$$\mathrm{Fe(OH)}^{2+} + {}^{\bullet}\mathrm{OH} \rightarrow \mathrm{Fe}^{2+} + \mathrm{H_2O_2} \qquad (3)$$

$$\mathrm{Fe}^{3+} + \mathrm{H_2O_2} \rightarrow \mathrm{Fe-OOH}^{2+} + \mathrm{H}^{+} \qquad (4)$$

$$\mathrm{Fe-OOH}^{2+} \rightarrow \mathrm{Fe}^{2+} + {}^{\bullet}\mathrm{OOH} \qquad (5)$$

$$\mathrm{Fe}^{3+} + {}^{\bullet}\mathrm{OOH} \rightarrow \mathrm{Fe}^{2+} + \mathrm{O_2} + \mathrm{H}^{+} \qquad (6)$$

It is worth noting again that the free radicals and H_2O_2 are generated in the above scheme even without externally added peroxide distinguishing this from the classical Fenton reaction[16] case. Thus highly oxidizing species such as $^{\bullet}OH$, H_2O_2, and other ROS such as $HO_2^{\bullet}$ are generated in reactions 1, 3, and 5 above. And all these are capable of oxidizing the lignite coal or carbon black surface accounting for the results seen in Figures 2.2 and 2.3 above.

Finally, it is pointed out that the enhanced currents seen on UV illumination of the anolyte (Figures 2.2 and 2.3) offer a practical strategy toward enhancing the hydrogen yield in the coal (or carbon) electrolysis scheme although the associated electrical costs of operating the lamp must be factored in any economic analysis.

2.4 Conclusion

In summary, this part of dissertation study has demonstrated that UV irradiation of the anolyte in a coal (or carbon) electrolysis scheme in the presence of iron redox species, affords enhanced currents associated with the free radical-induced oxidative attack of the coal (or carbon) surface. Useful mechanistic insights have also been gleaned into the factors responsible for the anode depolarization by the coal (or carbon) particles in the slurry suspension.

CHAPTER 3

CHEMICAL PRE-TREATMENT OF COAL AND CARBON BLACKS

3.1 Introduction

In what follows, the consequences of chemical pre-treatment of coals of varying rank and selected carbon black samples, on their ability to generate hydrogen in an electrolytic environment are explored. Concurrently, thermal analyses (differential scanning calorimetry or DSC and thermogravimetry or TGA) were performed on these pre-treated samples to investigate the consequences in terms of corresponding alterations in thermal reactivity. The chemical pre-treatment consisted of digestion with strong acid (1 M each of $HClO_4$, H_2SO_4, or HNO_3) or by stirring the coal, carbon black or multiwalled carbon nanotube (MWCNT) sample with 35 % H_2O_2 overnight. The influence of H_2O_2 pre-treatment is shown below to be critically dependent on the coal rank. Further, coal samples respond differently relative to carbon black surfaces in terms of how the hydrogen-generating capacity and thermal reactivity are altered by either acid or H_2O_2 pre-treatment. The chemical groups that are responsible for such enhancement and how it affects both the chemical and electrochemical processes involved in coal electrolysis are also explored.

The introduction of oxygen functional groups, especially the carbonyl groups, on the coal surface would selectively improve the chemical reactivity of coal and hence facilitates the elctron transfer between coal and iron (III) ions. MWCNTs were also included because of their chemical stability and well-defined chemical structrure which makes it easier to trace and identify any surface functional groups created as a result of different treatments. MWCNTs have been separately subjected to more powerful oxidation treatment with $KMnO_4$ to effect surface modification. We also separately quantify the contribution of TXLC and the redox mediator to the anodic current in an iron mediated electrolytic environment.

3.2 Experimental

3.2.1 Chemicals, materials, and electrolysis cell

Three types of coal and two types of carbon black samples were used in this part of the dissertation study (Table 2.1). The focus of this study was Texas lignite (as in our previous companion study reported elsewhere[50]), for comparison purposes, the coals were carefully chosen to cover the range from high-rank (DECS21), intermediate-rank (DECS10), to low-rank (TXLC). Proximate analysis data on these coals are given in Table 2.2. All the coal samples were finely ground and sieved to pass 200 mesh before use. The two carbon black samples were obtained from Sid Richardson Carbon & Energy Co (Fort Worth, TX) and are hereafter designated: SRC-401 and SRC-159 respectively (Table 2.I).

Table 3.I Designations of Coal and Carbon Black Samples Included in this Study

Sample	Texas lignite coal	Sub-bituminous coal	Anthracite coal	Carbon black	Partially graphitized carbon black
Designation	TXLC	DECS10	DECS21	SRC-410	SRC-159

The latter carbon black sample had been graphitized prior to use by heating at 1800 ℃ for 1 h followed by treatment with conc. HNO_3 for another hour. These samples had ash contents less than 1.0 % and 0.5 % and surface areas of 59 m^2/g and 260 m^2/g, respectively.

The MWCNTs were provided by Cheaptube (USA) and produced by chemical vapor deposition (CVD) using iron as the catalyst. Multiwalled carbon nanotubes (MWCNTs) rather than single walled carbon nanotubes (SWCNTs) were chosen for this study due to their wider availability, reduced strain, and relatively low production costs. The average diameter of these multi-walled carbon nanotubes ranged from 20 to 30 nm.

Ferrous sulfate 7-hydrate (AR) was from J.T. Baker. Ferric ammonium sulfate 12-hydrate (AR), sulfuric and nitric acid were from Mallinckrodt. Sulfuric acid and hydrogen peroxide (35 % w/v) were supplied by Alfa Aesar. All chemicals were used as received and all aqueous solutions and slurry suspensions were prepared using de-ionized water.

The three-electrode electrolysis cell consisted of a glass beaker containing a Pt foil (11 cm^2 area) anode. The coal or carbon black slurries were stirred with a magnetic stirrer to keep the particles in suspension and to maintain a constant flux of the mediator redox species (see below) to the electrode surface. A glass tube ending with a fritted glass disc (to prevent metal ions and coal particles from passing to the cathode compartment but yet allowing electrolytic contact between the two compartments) contained the catholyte (1 M solution of the corresponding acids) and a Pt wire cathode. The cathode tube was sealed from the other end except at a small aperture that allowed the collection of hydrogen over the surface of water in an inverted cylinder setup. The reference electrode was an Ag/AgCl/3 M NaCl electrode; all potentials below are quoted relative to this reference electrode. For the galvanostatic polarization experiments, the reaction mixture contained a fixed amount (40 ml) of 0.1 M solution of Fe(II) / Fe(III) mixture dissolved in 1 M H_2SO_4.

Table 3.2. Proximate and Ultimate Analysis Data for the Studied Coal Samples

Designation	TXLC	DECS10	DECS21
Coal Rank	Lignite	Sub-bituminous	Anthracite
Proximate analysis (dry)			
% Ash	22.40	12.56	11.15
% Vol. matter (dry)	44.20	41.76	4.51
% Fixed carbon	33.40	45.77	84.34
Ultimate analysis (dry)			
% Carbon	55.29	68.73	80.26
% Oxygen	16.09	13.30	3.82

The coal, carbon black and MWCNT dose in the slurry suspensions was 20 g/L (coal and carbon black) and 4 g/L, respectively, in the galvanostatic polarization experiments in both galvanostatic polarization and voltammetric experiments unless otherwise noted.

3.2.2 Acid digestion, H_2O_2 and $KMnO_4$ pre-treatments

Acid digestion of TXLC and SRC-401 was carried out in a beaker by boiling 1.6 g of the sample in 80 ml of 1 M acid ($HClO_4$, H_2SO_4 or HNO_3) for 20 min with stirring. The treated slurries were cooled and quantitatively transferred (without filtration) to the electrochemical cell. For the voltammetric runs, no externally-added iron redox mediator (see below) was used, while 40 ml aliquot of 0.1 M solution of Fe(II) / Fe(III) mixture in 1 M H_2SO_4 was added prior to the galvanostatic polarization runs. In all cases the final volume of the slurry was adjusted to 80 ml with an appropriate amount of the corresponding 1 M acid. For TGA and X-ray photoelectron spectroscopy (XPS) analyses, the acid-digested slurries were filtered and thoroughly washed with distilled water till the washings were neutral to pH paper, and then dried at 110 ℃ overnight. Wet oxidation with H_2O_2 was performed by simply stirring the samples with 35 % H_2O_2 overnight. The oxidized slurries were then filtered and thoroughly washed with distilled water and dried at 110 ℃ overnight. The pristine MWCNTs were chemically oxidized in H_2SO_4/500 wt% $KMnO_4$ and subsequently named (MWCNT-K). After oxidation, the samples were thoroughly washed and dried before characterization to monitor the change in their surface groups. It should be mentioned here that TXLC samples cannot withstand the $KMnO_4$ treatment and have been dissolved completely and cannot be subsequently separated from the oxidizing agent.

3.2.3 Instrumentation

AMETEK Solartron Multichannel Cell Test System Model 1470E and CH Instruments Model CHI 600C electrochemical analyzer were used for the galvanostatic and voltammetric experiments respectively. Simultaneous TGA/DSC analyses were performed on a TA Instruments Model SDT Q600. Variables such as sample mass, gas flow rate and heating rate were kept constant between runs to make comparisons meaningful. Raman spectra were acquired using a Thermo Fisher Raman micro spectrometer. The excitation source was a He–Ne laser (633 nm, 1.96 eV), focused (50x objective) to a spot size of approximately 2.1 μm. The spectral resolution was 5.8-8.8 cm^{-1} and the laser power was 5 mW. Fourier-transform infrared (FTIR) spectra were recorded using an IR Prestige-21 (SHIMADZU) FTIR spectrometer. The samples were mixed with potassium bromide (KBr), pressed into pellets of 1 mm thickness and measured in the absorption mode. A Kratos Axis 165 Ultra instrument was used for XPS; other details of the spectroscopic analyses are given elsewhere.[45]

3.3 Results and Discussion

3.3.1 Redox mediation of coal oxidation

Consensus has emerged that electrooxidation of the coal surface involves reversible (or quasi-reversible) redox mediators such as $Fe^{3+/2+}$ that are already present in the coal matrix. An undoubtedly over-simplified scheme for the chemical and electrochemical processes taking place during coal electrolysis is as follows where the coal is simply represented as C(s) and the oxidized surface of it is denoted as $C_{(ox)}(s)$:

At the anode:

$$Fe^{2+} \rightarrow Fe^{3+} + e$$

$$C(s) + 2H_2O(l) \rightarrow CO_2(g) + 4H^+ + 4e$$

In solution:

$$Fe^{3+} + C(s) + mH_2O(l) \rightarrow [C_{(ox)}(s), CO_2(g), CO(g)] + 2mH^+ + Fe^{2+}$$

At the cathode:

$$2H^+ + 2e \rightarrow H_2(g)$$

Several redox mediators have been deliberately added to the suspension such as $V^{5+/3+}$, $Mn^{3+/2+}$, $Ce^{4+/3+}$, $Fe^{3+/2+}$, I_3^-/I^-, and $Fe(CN)_6^{3-/4-}$ by previous researchers.[6,29] For this study we opted to use the $Fe^{3+/2+}$ redox couple as an oxidation mediator. The rationale for this choice was the ability of Fe^{3+} species to (partially) oxidize the bulk carbon phase as well as the surface functional groups of coal. In addition, it can be anodically regenerated at a low potential (0.8 V), much lower than the oxygen evolution reaction. Finally, Fe(II) / Fe(III) species are soluble in water and in acidic solutions and chemically stable over a long period of time under normal storage conditions.[13]

3.3.2 Acid digestion of Texas lignite coal and carbon black

3.3.2.1 Voltammetric Experiments

The linear sweep voltammetric curves in Figure 3.1 show that the applied potential required for initiating the oxidation of TXLC slurry varies according to the type of 1 M acid used in the digestion step. For both 1 M $HClO_4$ and I M $H_2SO_{4,}$ oxidation of the coal slurry started at an applied potential of 0.43 V and became mass-transfer limited at about 0.8 V. On the other hand, digestion with 1 M HNO_3 rendered the oxidation process more difficult with a required applied potential of 0.85 V and an absence of the mass transfer limited region due to overlap with the water oxidation wave. In all the cases, the anodic current is attributable to the oxidation of Fe^{2+} (leached from the inorganic content of the coal matrix) at the anode surface.[51] The higher anodic current density in 1 M $HClO_4$ case compared to the H_2SO_4 case can be simply attributed to the better ability of 1 M $HClO_4$ to dissolve the iron content of the coal matrix.

A study of the effect of digestion time in 1 M H_2SO_4 on the limiting current density at 0.8 V was carried out and the results are shown in Figure.3.2. After a boiling time of 15 min, the limiting anodic current density did not change, indicating the complete leaching of iron content of TXLC. Therefore a digestion time of 20 min was considered sufficient for all acid digestion treatments. The absence of any anodic current at 0.8 V in 1 M HNO_3 is due to the complete chemical oxidation of Fe^{2+} to Fe^{3+} species by the oxidizing acid during the digestion step. Although the ability of boiling HNO_3 to oxidize Fe^{2+} to Fe^{3+} is well known, we carried out a cyclic voltammetry (CV) experiment to confirm this hypothesis. Figure 3.3 shows the CV curves for an equimolar (1 mM) $Fe^{2+/3+}$ mixture in 1 M H_2SO_4 before (b) and after (c) boiling with HNO_3 acid in addition to a blank of 1 M KNO_3 solution (a). As the potential was scanned in the positive direction, curve (c) shows the absence of any initial anodic current compared to curve (b), marking the complete conversion of Fe^{2+} into Fe^{3+} as a result of the HNO_3 treatment. Correspondingly the cathodic peak (curve c) which corresponds to the reduction of Fe^{3+} into Fe^{2+} is well-defined and shows a higher cathodic current relative to curve (b).

3.3.2.2 Galvanostatic Polarization Experiments

Figure 3.4 contains results from galvanostatic polarization experiments (constant current: 50 mA, implying a current density of 4.5 mA/cm^2) for two blank solutions (a, c) and three test suspensions (b, d and e) containing acid-treated TXLC. Blank 1 consisted of 40 mL

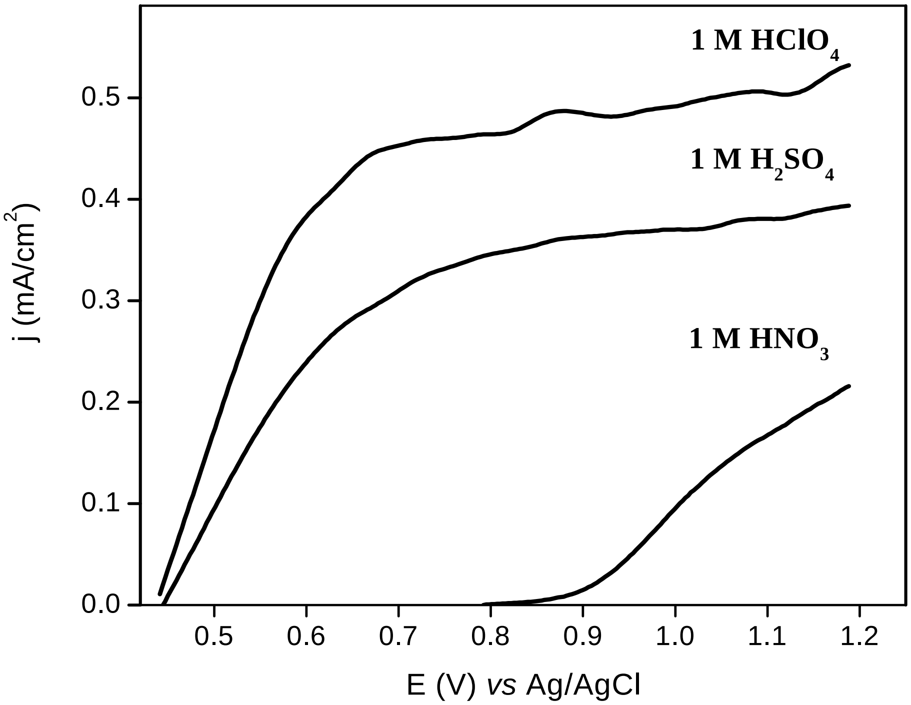

Figure 3.1. Linear sweep voltammograms (potential scan rate: 3 mV/s) for 20g/L TXLC slurries after digestion in different 1 M acids without externally added iron redox mediator.

aliquot of 0.1 M each of Fe(II) and Fe(III) species in 1 M H_2SO_4, while Blank 2 contained the stated amount of the redox mediator and 2 % (by mass) dose of untreated TXLC in 1 M H_2SO_4. The test suspensions contained the acid-treated slurry in addition to the redox mediator.

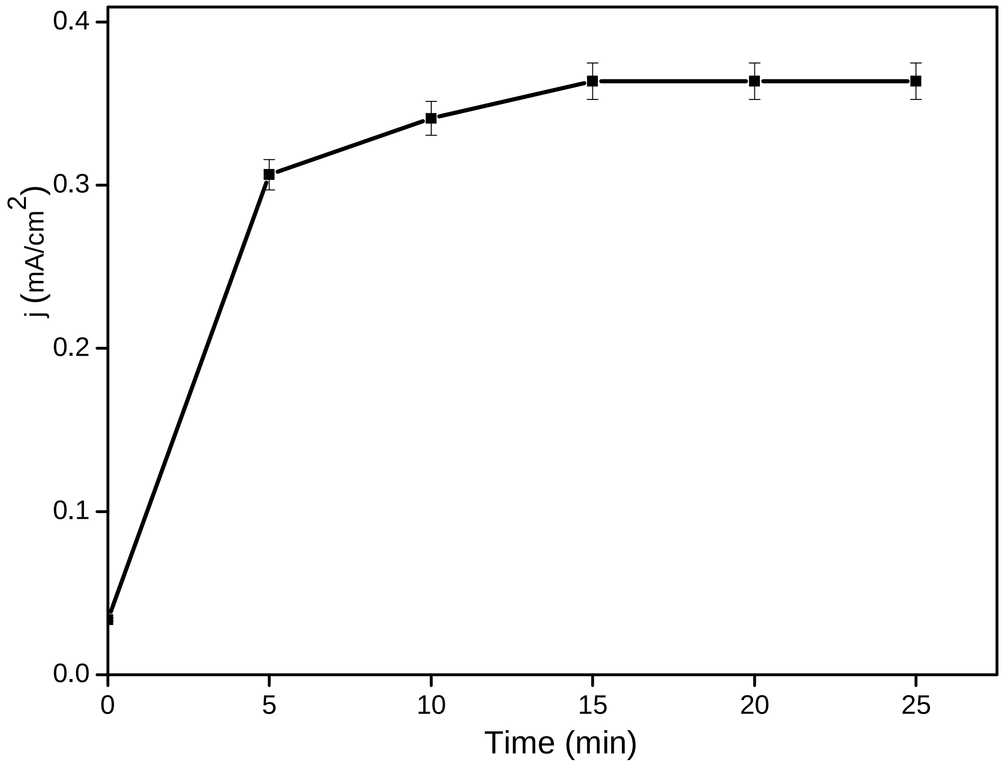

Figure 3.2. Effect of acid digestion time on the limiting current values for stirred TXLC slurries (20 g/L in 1 M H_2SO_4) at room temperature (data from Figure 3.1).

In interpreting these profiles, note that there are two plateaus, namely ca. 0.6 V and ca. 1.6 V; where the potential remains constant. These regimes are associated with Fe (II) oxidation and water oxidation at the anode surface respectively. The longer the plateau (with respect to the time axis) at the lower potential, the higher is the H_2 electrolytic yield from the coal electrolysis.

A shorter time span (before the potential jumps) signals that all the oxidizable species on the coal are used up.

The difference in the chronopotentiometric profiles (longer polarization time in Blank 2) between Blank 1 (curve a) and Blank 2 (curve c) can be attributed to:

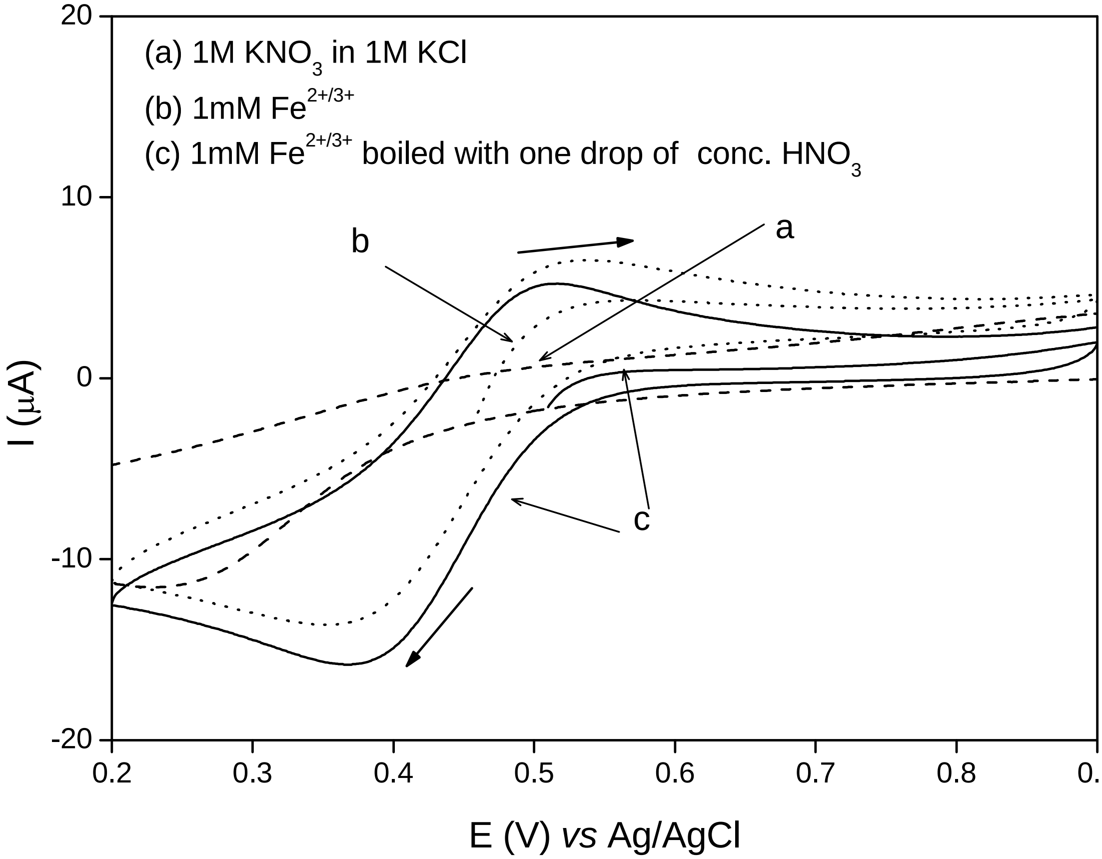

Figure 3.3 Cyclic voltammograms (scan rate: 3 mV/s) for blank (a) and equimolar 1mM $Fe^{2+/3+}$ mixture in 1 M H_2SO_4 before (b) and after boiling with one drop of conc. HNO_3 (c).

i) The extra amount of Fe (II) leached out of the TXLC matrix during the run which can depolarize the anode surface for a longer time.

ii) The extra amount of Fe (II) that can be regenerated as a result of the redox reaction between Fe (III) and TXLC particles.

iii) The ability of TXLC particles to depolarize the electrode surface in a direct electrochemical reaction. In fact direct electrochemical reaction of coal at the anode surface may be attributed to the oxidizable organic compounds leached out of the coal matrix. However, in this instance, the chronopotentiometric profile would show an additional inflection (at 1.4 V)[16] rather than the transition points corresponding to Fe(II) oxidation (at 0.6 V) or water oxidation (at 1.6 V) shown here. A more palatable explanation centers around the ability of the leached oxidizable organic compounds to react faster with Fe (III) (to regenerate more Fe (II) species for the electrode reaction) in addition to electrochemical oxidation of the functional groups on the coal particle surfaces.

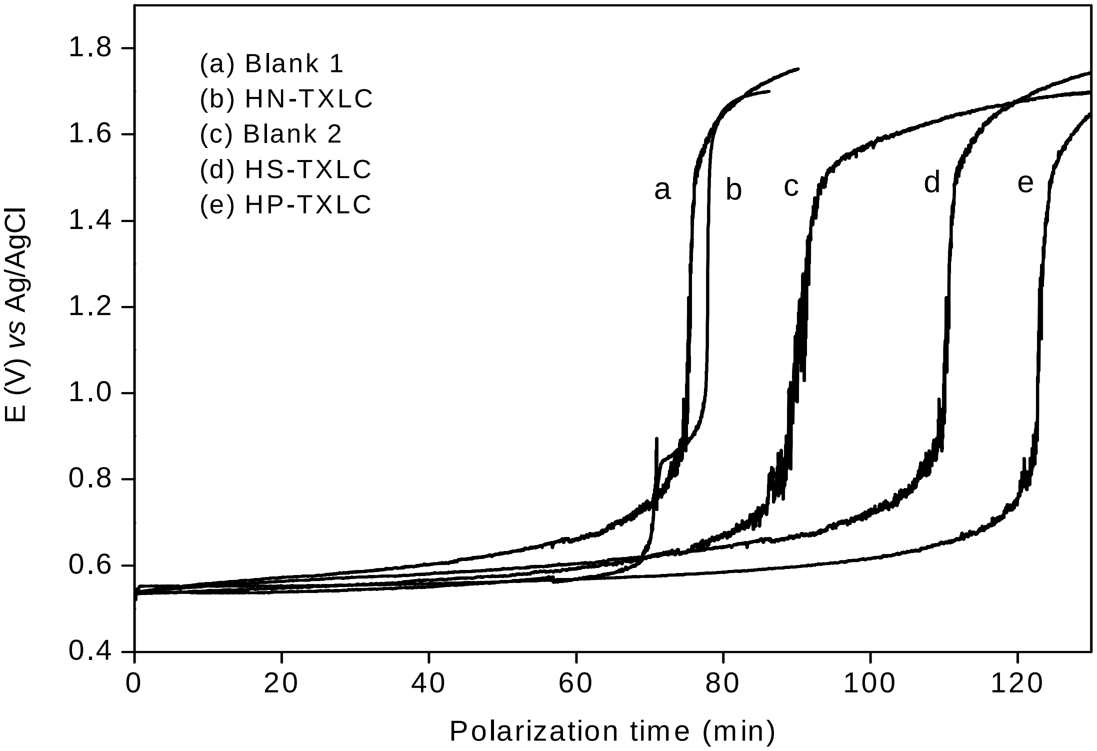

Figure 3.4 Galvanostatic polarization profiles for blank solutions (refer to text) and acid pre-treated TXLC suspension with externally added iron redox mediator.

The comparison between Blank 2 (curve c) which corresponds to as-received TXLC and the H_2SO_4-treated TXLC (HS-TXLC) (curve d) or $HClO_4$-treated TXLC (HP-TXLC) (curve e) samples shows the beneficial effect of coal pre-treatment on the polarization time and hence the amount of hydrogen generated at the cathode. The $HClO_4$ treatment was found to be better than H_2SO_4 treatment as indicated by a larger increase in polarization time. Table 3.3 shows a comparison between the different treatments in terms of the polarization time and the amount of hydrogen generated at the cathode. The better performance of HP-TXLC sample can be related to the better ability of $HClO_4$ to dissolve the pyrite and the other forms of iron (II) in coal and also to its better oxidizing power. In addition to the factors i), ii), and iii) identified above, mechanical disintegration of the coal particles (and consequent exposure of new surfaces) as a result of the acid pre-treatment can also play a crucial role. Such a picture would be consistent with the increase in the N_2 surface area measured after the pre-treatment (see below).

Thus the net result of acid pre-treatment can reside in a number of inter-related factors:

a) Improving the accessibility of Fe (III) to more reactive sites in the coal matrix. The kinetics of coal surface oxidation by reaction with Fe(III) is profoundly affected by the ability of Fe(III) to reach the coal reactive sites. According to the model advanced by previous authors[12], the reactive sites on the coal particle surfaces are divided into three categories with varying ease of accessibility. The acid digestion treatment is expected to convert most of the less accessible sites into the more accessible ones.

Table 3.3 Effect of Acid Digestion Treatment on the Iron Mediated Galvanostatic Polarization Behavior of TXLC Slurries

Digestion Acid	Polarization Time (min)	Volume of Hydrogen (mL)	% Increase in H_2 Generation
None (Blank 1)	70	22	0
None (Blank 2)	90	28	28
1M H_2SO_4	110	34	57
1M $HClO_4$	125	39	78
1M HNO_3	70	22	0

b) Increasing the surface area of coal particles and hence exposing more reactive surface groups to chemical or electrochemical reaction. The surface area of coal particles was measured (via nitrogen adsorption and the BET model) before and after treatment and the $HClO_4$ treatment was found to increase the surface area of TXLC from 3.24 m^2/g to 4.26 m^2/g. Such an increase in surface area is normally accompanied by an equivalent increase in the volume of pore space leading in turn, to improved coal reactivity.

c) Increasing the number of surface oxygen functional groups which would improve the reactivity of coal either with Fe (III) or with the anode surface. The effect of acid treatment on the surface oxygen functional groups was investigated by XPS analysis of the TXLC samples before and after digestion with 1M $HClO_4$ and the results are shown in Table 3.4. The appreciable increase in surface oxygen functional groups following the acid treatment is another factor that contributes to the improvement of chemical and electrochemical reactivity of TXLC. Aliphatic sites in the lignite macromolecule structure are the most susceptible to the attack by such an oxidizing acid treatment. Actually those aliphatic structures are highly abundant in the low-rank lignite coal (such as TXLC) structure. Their amount decreases when the coal rank is increased and can be easily converted into volatile compounds by the acid pre-treatment.[52]

Table 3.4 Effect of $HClO_4$ Acid Pre-treatment on the Surface Area and O/C ratio of TXLC and SRC-401 Samples

Sample	BET surface area(m^2/g)		O/C ratio (XPS data)	
	Before	After	Before	After
TXLC	3.2	4.2	3.8	7.7
SRC-401	59	60	2.6	5.6

The HNO_3-treated samples (HN-TXLC) constitute a rather special case because of the redox reactivity of the nitro groups themselves. Thus the last comparison that should be considered here is the behavior of HNO_3-treated TXLC sample (HN-TXLC) (curve b) compared to the untreated TXLC sample (curve c) in Figure 3.4. The shorter polarization time shown in the

HNO_3 case may be explained by the ability of boiling HNO_3 to completely oxidize the pyritic and other Fe (II) forms in TXLC. In such a case, an equivalent amount of nitrite ion should be produced:

In solution:

$$2Fe^{2+} + NO_3^- + 2H^+ \rightarrow 2Fe^{3+} + NO_2^- + H_2O$$

At the anode:

$$NO_2^- + H_2O \rightarrow NO_3^- + 2H^+ + 2e$$

This nitrite ion can be oxidized at the anode surface during the galvanostatic polarization run and appears as the first inflection point (at ~70 min) in Figure 3.4 that follows the Fe (II) oxidation plateau. Although the reaction between boiling HNO_3 and the Fe(II) content of coal is well-known and even officially used for its quantitative determination, it cannot alone account for that reduction of the polarization time when going from curve (c) to curve (b) in Figure. 3.4.

Other factors include the nitration and loss of organic matter as a result of HNO_3 acid treatment. Here the oxidation process does not stop at the stage of creating more oxygen functional groups (that would in turn improve the TXLC reactivity), but subsequent decomposition of those groups into volatile compounds is likely to take place,[23] rendering, in fact, the TXLC surface *less* reactive to oxidizing agents.

For comparison with the TXLC behavior, similar galvanostatic polarization experiments were repeated with SRC-401 (Figure 3.5). The first and most important conclusion can be drawn by comparing the Blank 2 experiment in Figure 3.4 (curve c) and Figure 3.5 (curve e). The longer polarization time in the SRC-401 case may be attributed to either its better ability to depolarize the anode surface or higher reactivity with the iron redox mediator. The higher carbon content as well as the larger surface area of SRC-401 is the underlying cause for its better chemical and electrochemical reactivity. Table 3.5 shows that all the acid treatments have reduced the polarization time to varying degrees compared to the untreated SRC-401 (curve e).

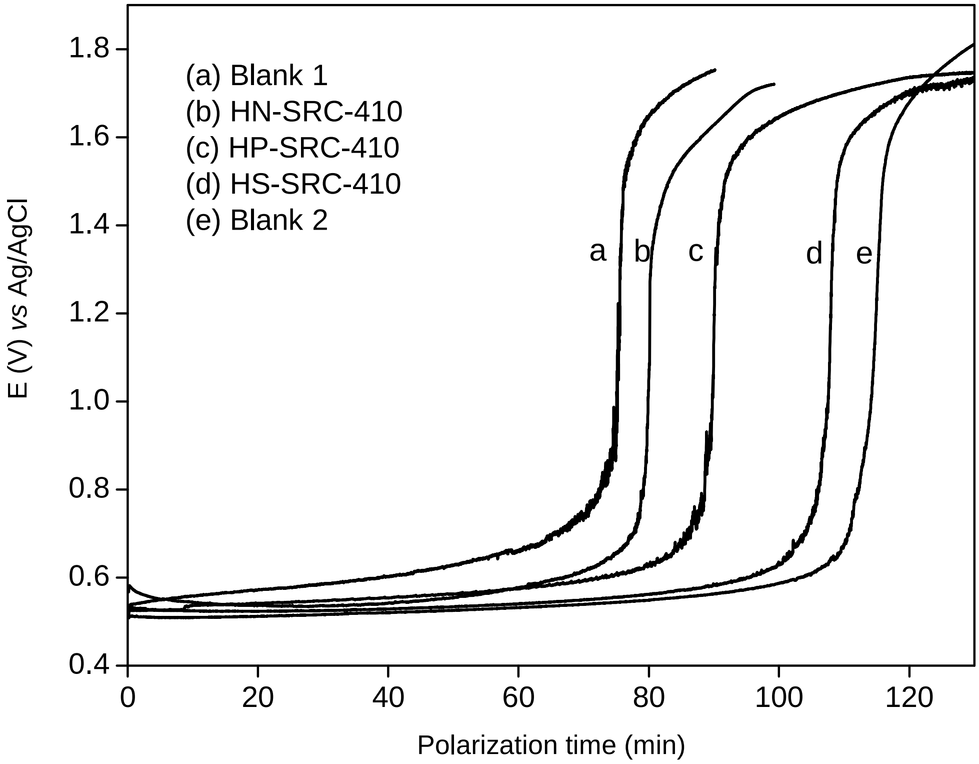

Figure 3.5 Galvanostatic polarization profiles for blank solutions (refer to text) and acid pre-treated SRC-401 suspension with externally added iron redox mediator.

Table 3.5 Effect of Acid Digestion Treatment on the Iron Mediated Galvanostatic Polarization Behavior of SRC-401 Slurries

Digestion Acid	Polarization Time (min)	Volume of H_2(ml)	% increase in H_2 generation
None (Blank 1)	70	22	0
None (Blank 2)	115	36	64
1M H_2SO_4	107	32	53
1M $HClO_4$	90	28	28
1M HNO_3	80	25	14

The greatest reduction in polarization time was observed in the HNO_3 treated SRC-401(HN-SRC-410). In addition, unlike the first inflection that appears with the HN-TXLC case in Fig. 3.4, HNO_3 treatment of SR-401 does not result in this feature (curve b, Fig. 3.5) due to the absence of any Fe (II) content in the SRC-401 sample. The surface area of the acid treated SRC-401 was decreased and the O/C ratio was increased as a result of acid digestion (Table 3.4). Both effects can result in the observed inversion of the polarization time trend compared to the TXLC case.

3.3.2.3 Consequences of Acid Pre-treatment on Thermal Reactivity

To have a more clear idea about the differential behavior of the untreated and acid pre-treated TXLC and SRC-401 samples, DSC and TGA characterization of TXLC and SRC-401 samples was carried out. An additional carbon black sample (SRC-159) was introduced here to confirm the effect of HNO_3 treatment on the thermal reactivity of the studied samples.

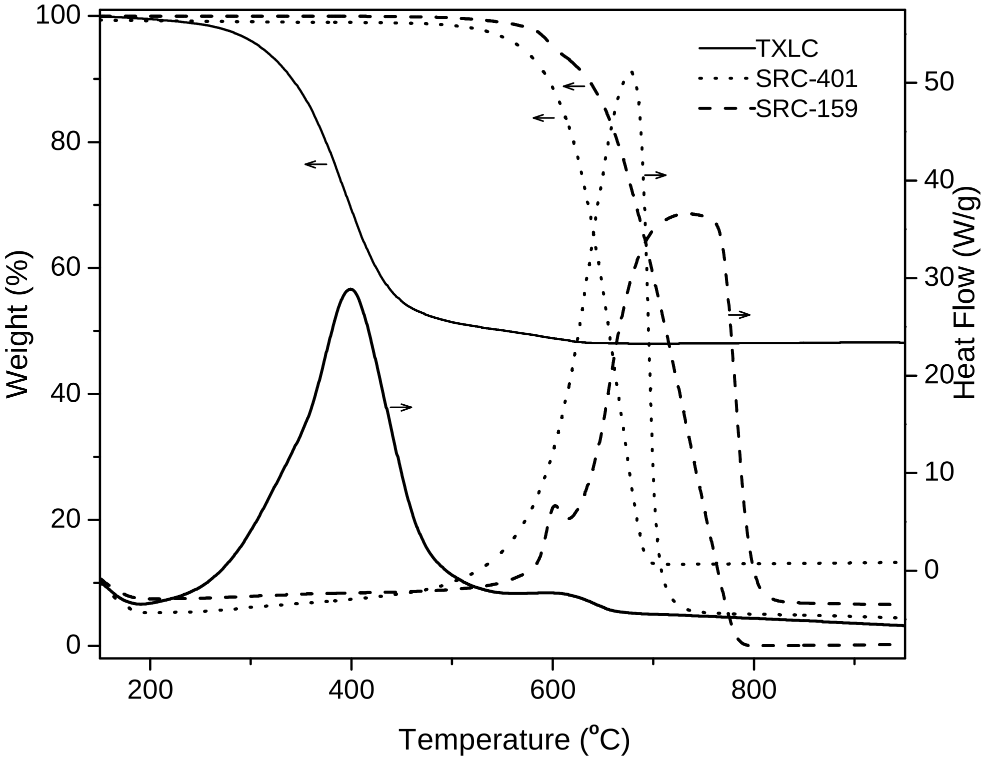

Figure 3.6.Thermal analysis (TGA and DSC) curves for TXLC, SRC-401 and SRC-159 samples.

The results are shown in Figure 3.6 and Table 3.6. The TXLC sample shows the lowest ignition temperature, T_{sh} **(**the temperature at which the sample begins to lose weight)[25,26] compared to the others, owing to the higher content of volatile matter which represent 44.2% of its dry weight. The volatile matter normally burns quickly at a lower temperature with a net effect of widening the combustion interval, t_{ci} (the time interval between T_{sh} and T_{ec}, the end of the combustion regime) and reducing the burning intensity, I (the intensity of instantaneous heat release calculated by dividing the peak height, H, the distance vertical to the temperature axis, between the base line and the peak tip in the DSC curve by W, the time interval at half height of the DSC peak).[26] It is clearly seen here that graphitization and HNO_3 treatment (SRC-159 sample) has rendered it the most un-reactive for combustion. As shown in Table 3.6, the SRC-159 sample shows highest values for the T_{sh}, T_{ec} parameters and the lowest value for I.

Table 3.6 Parameters from Simultaneous TGA and DSC Analyses of Untreated TXLC and SRC-401 Samples [a]

Sample	H/(W/g)	W(min)	T_{sh}(℃)	T_{ec}(℃)	t_{ci}(min)	I/(W/g.min)
TXLC	29	4	340	450	4	7.2
SRC-401	52	3	531	705	3.5	17.3
SRC-159	37	6	579	797	8	6.2

[a] Refer to Figure 3.6 and the text.

The results for the acid pre-treated TXLC samples are shown in Figure 3.7 and Table 3.7. The highest mass change % (i.e., the ratio of mass loss during the course of coal combustion), which corresponds to the demineralization ability of the acid, was found to be for the $HClO_4$ case (HP-TXLC). This behavior corroborates the results shown earlier in Figure 3.1 and explains the longer polarization time in this case compared to the H_2SO_4 case (HS-TXLC). The HNO_3 acid pre-treatment (HN-TXLC) results in almost the same percent mass change but the demineralization ability is accompanied by complete oxidation of the dissolved mineral matrix. The introduction of oxygen functional groups on the coal surface as a result of the oxidizing acid pre-treatment manifests here as an additional inflection which appears prior to the sharp one that corresponds to complete coal combustion. This initial inflection in the TGA curve, which is clear in all cases except the TXLC curve (untreated sample), is due to the combustion of volatile matter which normally takes place at lower temperature. In other words, the introduction of volatile matter due to acid pre-treatment has lowered the TXLC ignition temperature and elevated the end of combustion temperature and the combustion interval. Again for comparative purposes, the effect of acid pre-treatment on the thermal reactivity of SRC-401 was also studied and the results are shown in Figure 3.8. The introduction of oxygen functional groups on the carbon black surface has clearly lowered the ignition temperature (T_{sh}) and the burning intensity (I) and has widened the combustion interval (t_{ci}) compared to the untreated SRC-401 sample. This modification in the thermal behavior reflects more resistance to combustion. It is worth noting here that the change in the thermal parameters specially the combustion interval and the burning intensity, follows the same trend as the galvanostatic behavior, with the HNO_3-treated sample (HN-SRC-401) showing the lowest burning intensity

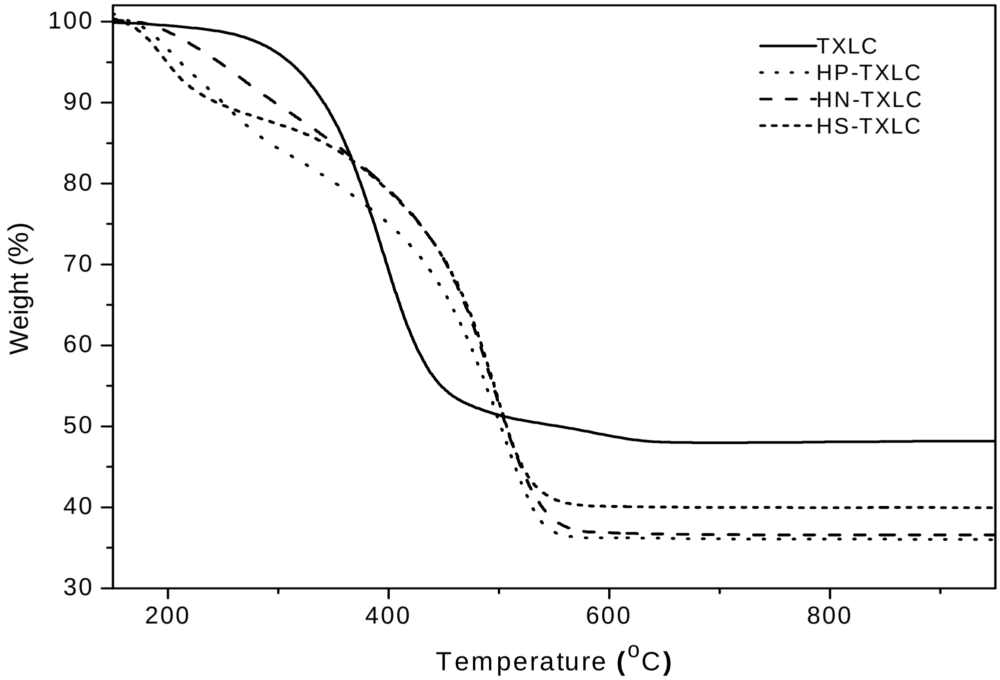

Figure 3.7. Thermal analysis (TGA) curves for TXLC before and after treatment with different 1 M acids.

and the longest combustion interval, followed by the $HClO_4$-treated sample (HP-SRC-401) and then the H_2SO_4-treated sample (HS-SRC-401).

Table 3.7 Effect of Acid Pre-treatment on the TGA Parameters for TXLC [a]

Coal sample	Mass change %	T_{sh}(℃)	T_{ec}(℃)	t_{ci}(min)
TXLC	46	340	450	4
HN-TXLC	63	210	540	16
HS-TXLC	60	180	530	17
HP-TXLC	65	200	540	16

[a] Refer to Figure 3.7 and the text.

3.3.3 *Peroxide pre-treatment of coal and carbon black*

3.3.3.1 Rationale

The main idea is that H_2O_2 can act as an oxidizing and a reducing agent. As an oxidizing agent, it has a high standard reduction potential (E° = 1.76 V vs. SHE), which means that it is a powerful oxidizing agent.

$$H_2O_2 + 2H^+ + 2e \rightarrow 2H_2O$$

Accordingly, treating the coal samples with H_2O_2 prior to galvanostatic polarization experiments should change their electrochemical behavior (i.e., decrease their electrolytic oxidation susceptibility) compared to the untreated samples. Such behavior change may give some insights into the mechanism and the elusive nature of the functional groups which are involved in coal chemical or electrochemical oxidation. As a powerful oxidizing agent, H_2O_2 will be able to oxidize both the inorganic (e.g., Fe (II) and S^{2-}) as well as the organic content of coal. As a (less potent) reducing agent, H_2O_2 can be easily oxidized at the anode surface (E° = 0.69 V vs. SHE):

$$H_2O_2 \rightarrow O_2 + 2H^+ + 2e$$

3.3.3.2 Galvanostatic Polarization Experiments

Figure 3.9 contains results from these experiments (constant current: 50 mA, i.e.

current density = 4.5 mA/cm^2) for a blank solution (a) and three test suspensions (b, c and d) containing DECS21, DECS10 and TXLC, respectively. The blank run consisted of 30 mM of H_2O_2 in 1 M $HClO_4$ and showed the longest polarization time, as all the initially-added H_2O_2 was available for the electrode reaction. Upon addition of coal, a redox (galvanic) reaction between coal (organic and inorganic content) and H_2O_2 took place, decreasing the amount of H_2O_2 available for electrode reaction.

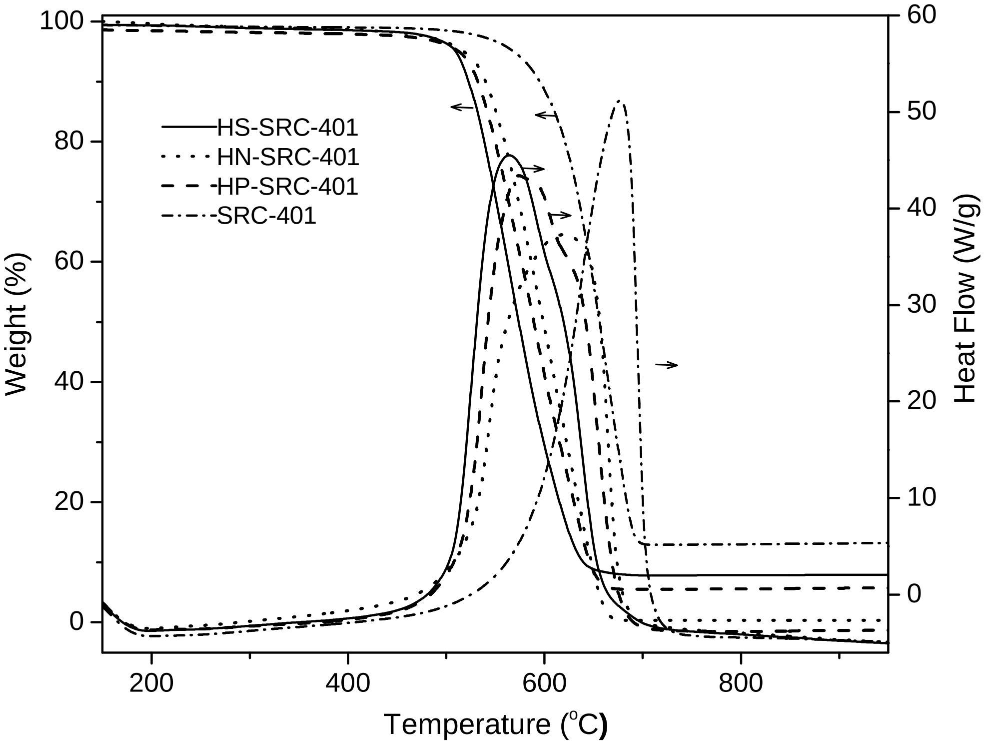

Figure 3.8. Thermal analysis (TGA and DSC) curves for SRC-401 before and after treatment with different 1 M acids.

Depending on how facile this redox reaction was, there would be a concomitant reduction in the polarization time. It should be emphasized here that these galvanostatic polarization runs were not aimed at probing hydrogen generation; H_2O_2 was used here instead as a probe for coal reactivity. As shown in Figure 3.9, the greatest reduction in polarization time (77 %) and hence the best reactivity was observed with TXLC samples (curve d). This was followed by the DECS10 sample (curve c) and then DECS21 sample (curve b) which showed reductions of 28 % and 14 %, respectively.

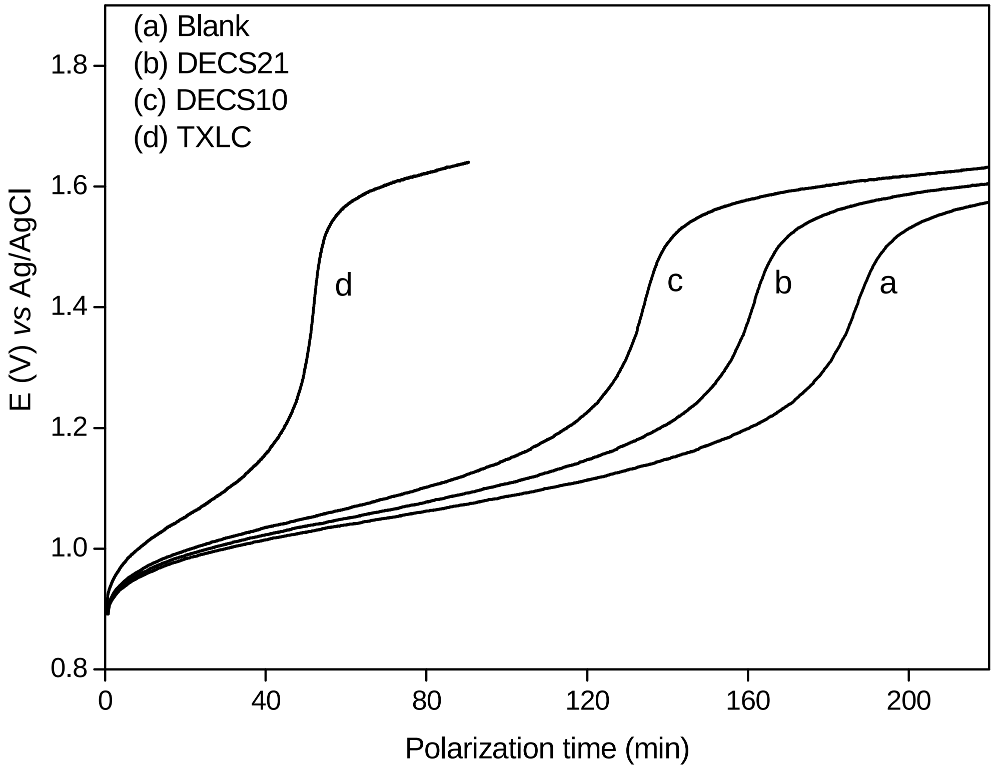

Figure 3.9. Galvanostatic polarization profiles for blank solution and slurries in 30 mM H_2O_2.

The difference in reactivity between the three samples cannot be attributed to their fixed carbon content. Actually, DECS21 sample, the least reactive coal, has the highest fixed carbon content (refer to Table 3.2), while TXLC, the most reactive one, has the lowest fixed carbon content. Instead, the availability of susceptible organic groups can be the underlying cause for the difference in reactivity with H_2O_2. The most susceptible organic moieties to chemical oxidation are the methylene groups which act as a cross linkers in the coal macromolecular matrix. Methylene groups can be oxidized to carbonyl groups upon H_2O_2 pre-treatment.[53] Low rank coals, such as TXLC, usually have higher aliphatic content than the higher rank coal samples,[52] rendering them more susceptible to chemical oxidation. The breakdown of the cross linker groups upon H_2O_2 treatment will expose more surface functional groups and at the same time will improve the pore network in the coal macromolecules

Based on these results, we decided to use H_2O_2 in a different way, aiming at enhancing the amount of hydrogen that can be generated at the cathode in an iron-mediated electrolysis cell. In the new experiments, the three coal samples and a carbon black sample (SRC-410) and MWCNTs (Table 3.1) were pre-treated with H_2O_2 overnight (refer to the experimental section) and then mixed with the iron redox mediator under the same experimental conditions described for the acid pre-treatment part of this study. Table 3.8 shows the results. Blank 1 and 2 experiments were described before in the acid pre-treatment section above.

Table 3.8 Effect of H_2O_2 Pre-treatment on the Galvanostatic Polarization Behavior of Coal and Carbon Black Slurries

Pretreatment	Polarization time(min)			
	TXLC	DECS10	DECS21	SRC-410
None (Blank 1)	70			
None (Blank 2)	90	100	100	115
35% H_2O_2	100	97	97	107

The comparison between the various samples in the Blank 2 experiments shows how the fixed carbon content of untreated samples positively affected the polarization time. The SRC-410 sample, with a fixed carbon content of more than 99 % showed the largest increase (64 %) in polarization time. On the other hand, the TXLC sample with the lowest fixed carbon content (44.2 %) shows the least improvement of polarization time (28 %). The polarization time improved only for the TXLC sample upon H_2O_2 pre-treatment, while for the other samples, this parameter was almost the same (DECS10, DECS 21) or even shorter (SRC-410). It should be noted that the H_2O_2 pre-treatment increased the amount of oxygen functional groups on the

TXLC surface with a consequent improvement in the reactivity with either the redox mediator or the anode surface. Note also that Fe (II) species no longer play a role here; almost all such oxidizable inorganic species should have been consumed during the pre-treatment step. This leads to an important comparison between the effect of H_2O_2 vs. HNO_3 (the most commonly used oxidizing agents in coal industry) on the galvanostatic polarization behavior of TXLC. Both treatments are able to increase the oxygen functional groups on the TXLC surface and deactivate any oxidizable inorganic content in the sample. On the other hand, only the HNO_3 pre-treatment further appears to convert these groups to volatile products, rendering the TXLC surface less amenable to oxidation (refer to Figure 3.5).

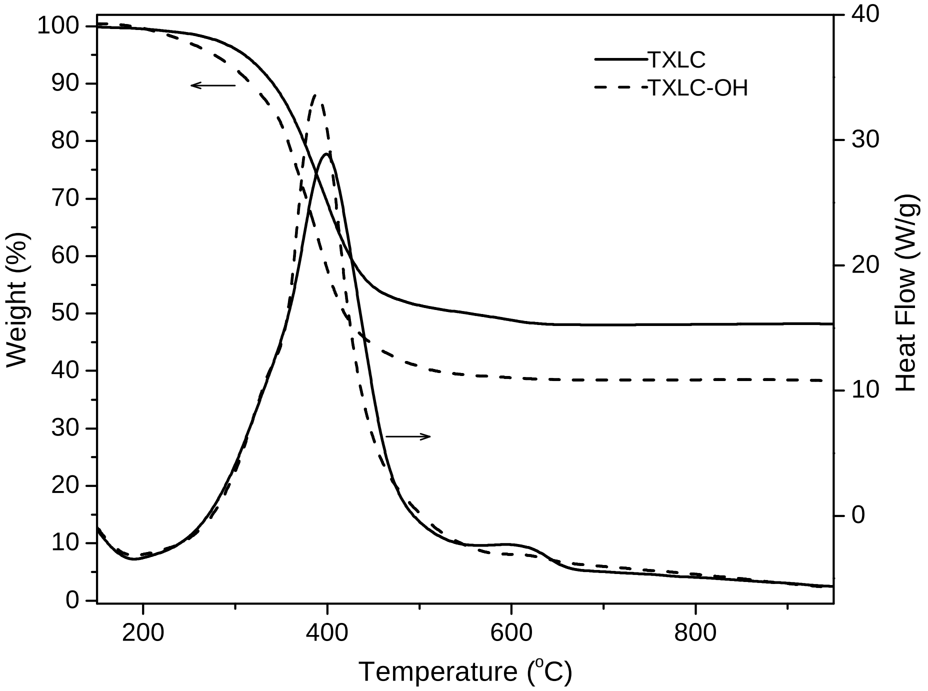

Figure 3.10.Thermal analysis (TGA and DSC) curves for TXLC before and after treatment with H_2O_2.

3.3.3.3 TGA and DSC Experiments

TGA and DSC characterization of TXLC sample before and after H_2O_2 pre-treatment

(TXLC-OH) was carried out and the results are shown in Figure 3.10. H_2O_2 pre-treatment obviously decreased the ash content of TXLC and hence increased the effective carbon content. This can be considered as an additional factor that contributed to the improvement in the galvanostatic polarization behavior of TXLC-OH sample discussed in the preceding section. The introduction of oxygen functional groups upon H_2O_2 pre-treatment is marked by the decrease in the ignition temperature, T_{sh}, widening the combustion interval, t_{ci} and lowering the burn intensity, I.

3.3.4 Mechanistic aspects of coal and carbon black electrolysis

3.3.4.1 Chemical vs. Electrochemical Reactivity of TXLC and Carbon Blacks

The reactions taking place on the anode side of the electrochemical cell are two types. The first type is an electrochemical (direct oxidation) reaction that involves an electron transfer between the anode and a chemical species in solution. The chemical species available for anode reaction are the iron(II) ions and the carbonaceous material particles. The electrochemical oxidation of iron(II) on platinum electrode is known to be reversible or quasi reversible and hence taking place quickly. On the otherhand , the oxidation of the carbonaceous material particles is known to be irreversible[54] and varies according the coal rank. The second type is a sloution chemical reaction (indirect) where the reactive sites on the coal paritcle surface are getting oxidized by iron(III) ions. Different sites on the coal particle surface can react at different rates[55].

3.3.4.2 Galvanostatic Polarization Experiments

The contribution of each of the aforementioned reactions to the total polarization time in a glvanostatic run is shown in Figure 3.11. The contribution of the redox mediator to the total polarization time is simply obtained by running a reagent blank (solution of redox mediator in 1 M H_2SO_4) experiment (Figure 3.11B). This experiment was run at a fixed current of 50 mA as the kinetics are very fast. The same high current (50 mA) was also applied for the coal-mediator experiment (Figure 3.11C) but can not be attained when a coal slurry(without any externally added iron) is used as an anode depolarizer (Figure 3.11A). Instead, a smaller current of 3 mA was used. It is worth noted here that this experiment accounts for any contributions from the coal particles itself, any dissolved iron or oxidizable organic compounds leached out of the coal matrix. For the sake of comparing the three experiments (A, B and C), the x-axis was conveted into charge (Q) rather than a time (t) axis.

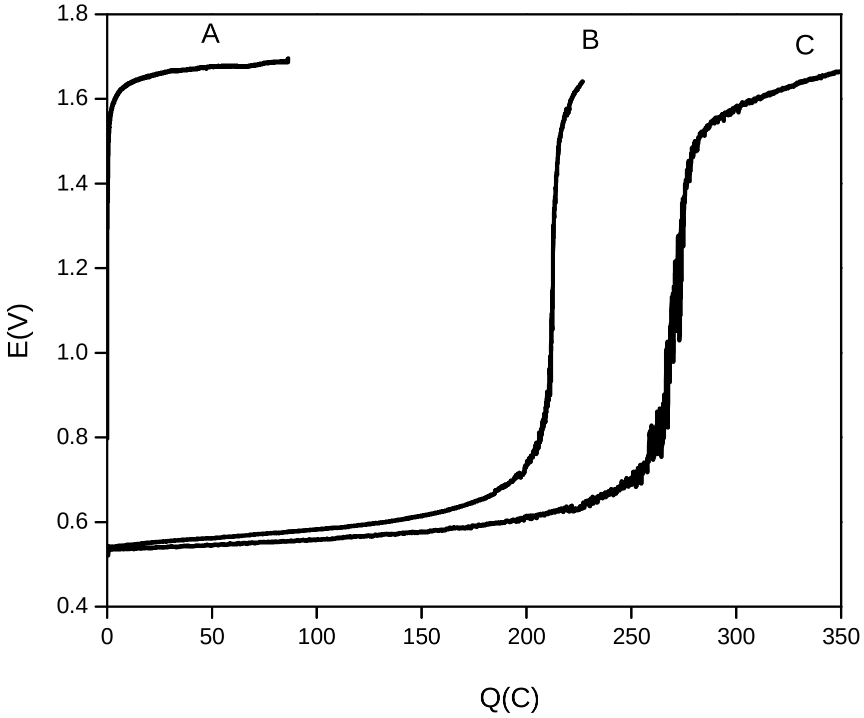

Figure 3.11 Galvanostatic polarization profiles for blank solution (refer to text) and TXLC suspension with and without externally added iron redox mediator.

As shown in Figure 3.11 A, part of the charge consumed during the electrochemical process is due to oxidation of coal particle surface groups as well as any inherent oxidizable ions in the coal matrix on the anode. Actually this electrode reaction did not start until the cell potential have reached a value of 1.4 V. Although the amount of charge consumed in this electrochemical reaction is very small compared to the charge involved in the redox process of the mediator (Figure 3.11B), it is still an obvious evidence of coal particle oxidation on the anode surface and even an indication to how difficult it is to electrochemically oxidize the coal particles. Figure 3.11C showed an amount of a charge that is not a simple addition of the amount of charges involved in Figures 3.11A and 3.11B. The value of charge is actually too much higher than the simple addition value. Since Figure 3.11C is representing an experiment run at a polarization current of 50 mA which can not be supported by the direct redox reaction of coal particle surface, the amount of charge expressed represent a vlaue that is completely due to the redox mediator and the indirect (chemical) reaction between iron(III) ions and coal surface groups. This cleary indicate that the main process responsible for enhancement of polarization time is the chemical reaction between coal and iron(III).

It should be clarified here that there is no controversy between the amenability of coal particles surface for oxidation with iron(III) ions and their resistance to oxidation on the anode surface. The standard reduction potential of iron(III) ions is 0.76 V while the anodic oxidation of coal particles did not start untill the cell potential reached 1.4 V (Figure 3.11A). This is explained by the high overpotential required to bring the suspended coal particles (which lack any electric conductivity) to the electrode surface. On the other hand the iron(III) ions are freely moving in solution and their adsorption on the coal particle surface is a preliminary step for the redox reaction.[9]

The same set of experiments were repeated with SRC-401 slurry and the results are shown in Figure 3.12. In this case a reasonable amount of charge was attributed to direct oxidation of the carbon black on the electrode surface but the glavnostatic behaviour was still dominated by the the chemical reaction between iron(III) ions and carbon black surface groups.The charge transfer took place at relatively lower potential compared to the TXLC case marking the readiness of the direct electrochemical oxidation of carbon black.

Both TXLC and SRC-401 were subjected to oxidation with H_2O_2. This pre-treatment has resulted in enhancement of polarization time in the galvanostatic polarization experiments of TXLC rather than SRC-401 sample. Here we are explain the consequences

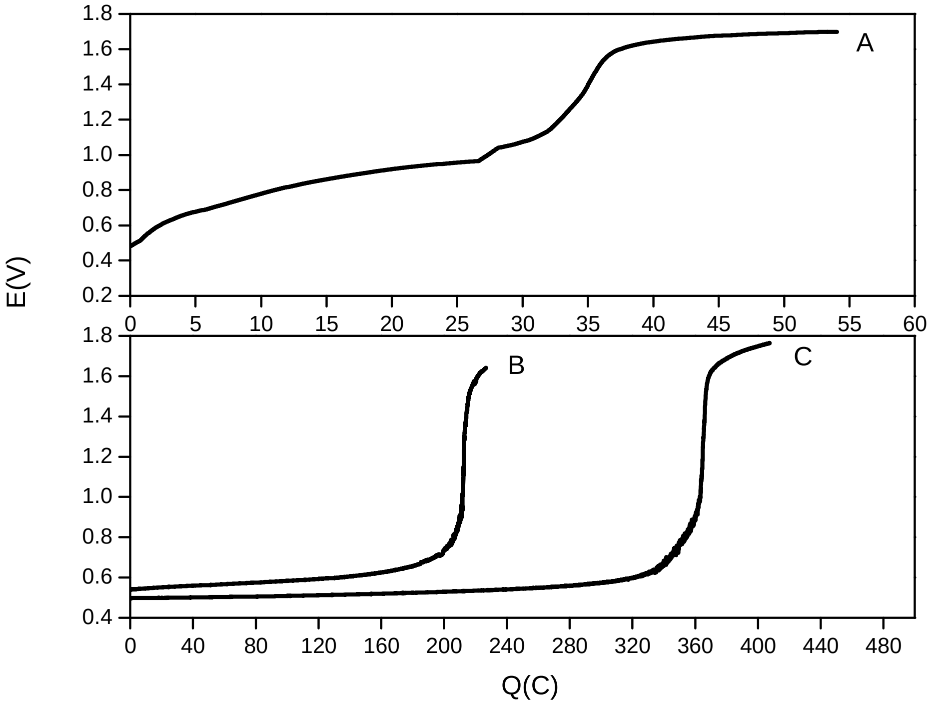

Figure 3.12 Galvanostatic polarization profiles for blank solution and TXLC suspension with and without externally added iron redox mediator.

of such treatment on the chemical and electrochemical reactivity of the studied samples separately. The SRC-401 sample did not show any change in the galvanostatic behaviour[56]. The polarization time remained unaffected. Both the chemical and electrochemical reactivity stayed the same as before treatment. The resistance of carbon black sample (SRC-401) to chemical pretreatment has been previously explained.[56] Figure 3.13 shows the change in the different reactivities of the studied TXLC sample following oxidation treatment. The introduction of surface oxygen function groups on the TXLC surface as a result of H_2O_2 pretretment was expected to make the surface more hydrophilic and to improve the direct electrochemical reaction. However, the electrochemical reactivity of TXLC did not change following H_2O_2 pretretment as shown in Figure 3.13A. The quantity of charge transferred to the TXLC particles before water oxidation starts (at 1.6 V) is the same as in Figure 3.11A. The enhancement of the amount of charge transferred during TXLC electrolysis shown in Figure 3.13B (compared to Figure 3.11C) can then be attributed to the improvement of the chemical reactivity of TXLC with the redox mediator. Note that the contribution of the redox mediator itself to the amount of charge should stay unchanged before and after H_2O_2 pretreatment.

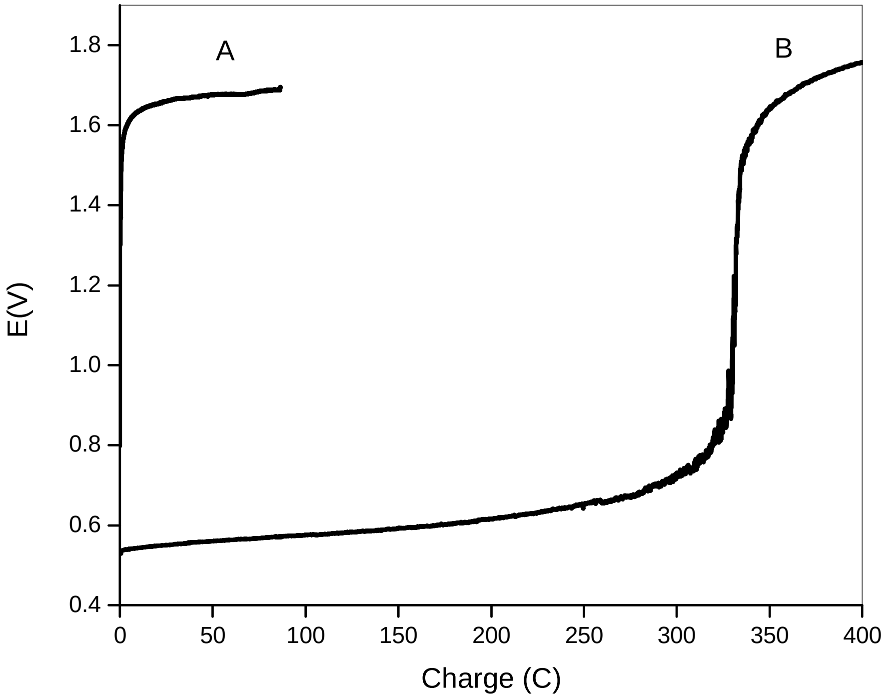

Figure 3.13 Galvanostatic polarization profiles for oxidized TXLC suspension with and without externally added iron redox mediator.

The change in the surface and the bulk chemsitry of TXLC particles following the treatment was monitored by XPS and FTIR experiments, respectively to relate this improvement of chemical reactivity to specific functional groups.

3.3.4.3 XPS Data of Bare and Oxidized TXLC

XPS analysis can provide information about chemical bonding on the surface of particles. XPS was performed on both as received (TXLC) and H_2O_2 treated (TXLC-OH) samples to show the effect of such treatment on the surface elemental composition. The XPS spectra are shown in Figures 3.14 and 3.15. For the TXLC sample (Figure 3.14), the C 1s main peak was scanned at high resolution. Figure 3.14 gives a typical carbon 1s peak envelope from the untreated TXLC. In the peak deconvolution, the overall peak in the range of 280–287 eV can be fitted by a superposition of two peaks. The main peak (282.21 eV) is attributed to the C 1s, while the other peak (284.09 eV) is assigned to the C–O bond.[57] The spectrum of the TXLC-OH sample is shown in Figure 3.15. In addition to the above two mentioned peaks, another peak at (286.35 eV) appeared and is assigned to the –C=O bond. The semi-quantitative

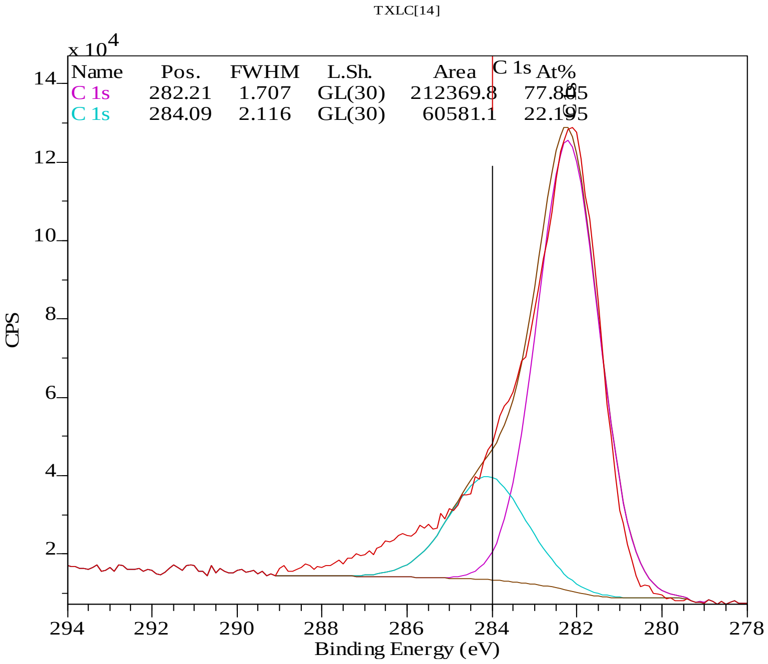

Figure 3.14 Deconvoluted X-ray photoelectron spectrum of as received TXLC.

analysis of TXLC-OH sample shows the relative concentration of surface carbon

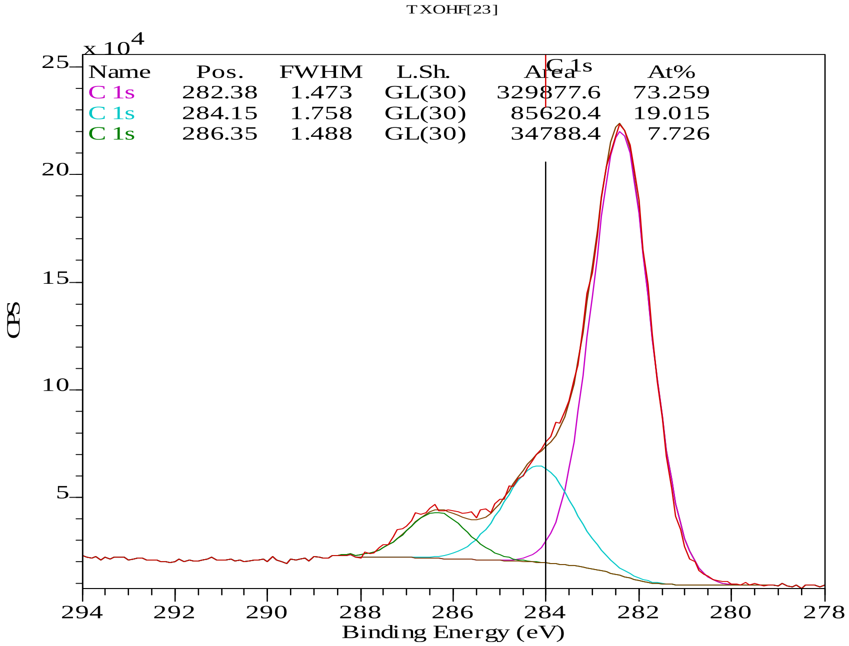

Figure 3.15 Deconvoluted X-ray photoelectron spectrum of TXLC after oxidation with H_2O_2.

atoms that have been functionalized compared to the as received TXLC sample. (Table 3.9). An overall increase in atomic % of carbon atoms bonded to oxygen (27% in TXLC-OH compared to 22% in TXLC) is observed and about 8% is assigned to -C=O bonds. This surface increase in the carbonyl group functionalities may or may not be accompanied by a corresponding increase in their bulk concentration and must be confirmed by FTIR spectroscopy .

3.3.4.4 FTIR Spectra of Bare and Oxidized TXLC

The FTIR spectra of TXLC and TXLC-H samples are shown in Figure 3.16. A well defined peak with a maximum at 1710 cm^{-1} was observed. This peak is much less defined for the untreated TXLC compared to TXLC-H sample and is attributed to carbonyl (C=O) groups. Both XPS and FTIR data confirm the increase of carbonyl groups on TXLC particles following the H_2O_2 treatment and clearly confirm the crucial rule of such functional groups in improving the chemical reactivity of coal particles in iron mediated coal electrolysis.

Table 3.9 Semi-quantitative Analysis of Surface Groups in TXLC before and after Oxidation with H_2O_2

Peak	TXLC		TXLC-OH	
	Position (eV)	Atomic conc.(%)	Position (eV)	Atomic conc.(%)
C 1s	282.21	77.89	282.38	73.25
-C-OH	284.09	22.11	284.15	19.02
-C=O	-	-	286.35	7.73

3.3.4.5 Thermodynamics and Kinetics of Spontaneous Reduction of Fe(III)

The spontaneous reduction of Fe(III) on TXLC particle surface is driven by the difference between the standard reduction potential (SRP) of Fe(III) /Fe(II) pair and the SRP of TXLC.

$$\Delta E = E_{Fe(II)/Fe(III)} - E_{Reduced\text{-}TXLC/Oxidized\text{-}TXLC} > 0$$

The standard electrode potential of coal redox reaction was calculated to be 0.228 V vs NHE.[58] The $Fe(H_2O)_6^{3+/2+}$ couple has an SRP of 0.76 V and exhibits kinetics strongly dependent on the presence of surface oxides, particularly carbonyl groups[59]. Introduction of more surface carbonyl groups on the coal surface would make the chemical reaction with Fe(III) ions faster. This would release more Fe(II) ions into the solution phase and extend the galvanostatic polarization time. Similar reasoning can account for the improved chemical reactivity of carbon black (SRC-401) compared to TXLC (Figure 3.11C vs Figure 3.12C). Carbon blacks are known to have both quinone and hydroquinone groups on their surface.[55] The estimated concentration of both groups was found to be 0.002-0.26% and 0.016-0.47%, respectively.[58] In order to confirm or exclude any contribution of the hydroquinone groups to the improved chemical reactivity, another set of experiments were performed with carbons of well defined surface structure and chemical stability, namley, MWCNTs. More harsh chemical oxidation with $KMnO_4$

was used in addition to H_2O_2 oxidation to ensure sufficient oxidation of the nanotubes.

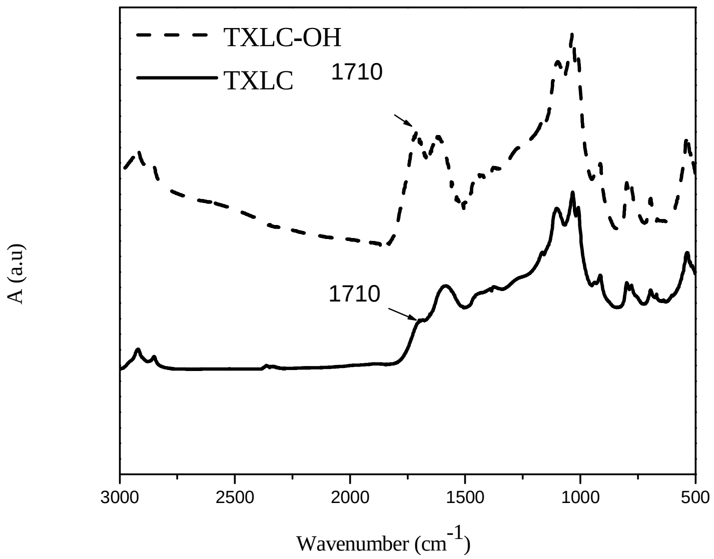

Figure 3.16 FTIR spectra of as-received (TXLC) and oxidized (TXLC-OH) coal.

3.3.4.6 Raman Spectra of Bare and Oxidized MWCNTs

Raman spectroscopy is a very efficient tool for characterizing carbon-based nanostructures.[36] The Raman spectra of CNTs usually exhibit four to five characteristic bands (Figure 3.17 A) : the G mode (1500–1600 cm^{-1}) which originates from the stretching vibrations of the carbon–carbon bonds within the graphene sheets, the D mode (1350 cm^{-1}) which is a measure of amorphous or disordered carbon in the CNT samples and most likely stems from added functional groups or missing carbon atoms in the wall,[60] the G` mode (2600-2700 cm^{-1}), the second overtone of the defect-induced D mode and finally, the radial breathing modes (RBMs) (100–400 cm^{-1}) which is sensitive to the diameter of SWCNT and rarely found in the spectra of MWCNTs.[36] The oxidation of MWCNTs was previously used to determine the best conditions to remove amorphous carbon, introduce defects and functionalize their surface.[36] The ratio of Raman intensities, R, of the D and G bands (I_D/I_G) of the as-received and chemically oxidized MWCNTs (Table 3.10) was used to quantify the density of structural defects

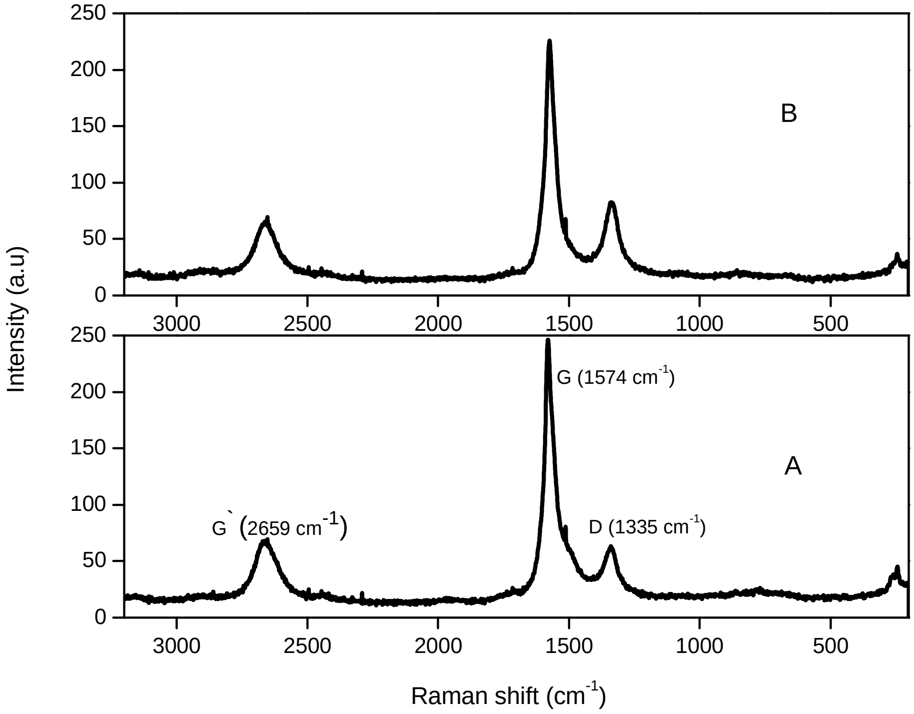

Figure 3.17. Raman spectra of as received MWCNTs (A) and MWCNTs oxidized with H_2O_2 (B).

created by such pre-treatment. The R value increased sharply in the case of $KMnO_4$ treatment (0.25 to 0.56) compared to H_2O_2 (0.25-0.36) (compare Figures 3.17B and 3.18B). The increase in disorder indicated by the increase in Raman R value (i.e. from 0.25 to 0.56 in MWCNT-K) may be due to

Table 3.10 Raman Spectrum Parameters of the As received and Oxidized MWCNTs

Sample	D band (cm^{-1})	G band (cm^{-1})	G' band (cm^{-1})	R
MWCNT	1339	1578	2665	25
MWCNT-K	1339	1573	2665	56
MWCNT-H	1335	1574	2660	36

disruption of surface graphene planes by hydroxylation. This oxidation changes the chemical make-up of the reactive edge of the tips and perhaps even the outer (and the inner) layer of the nanotube. XPS was used to study chemical modification of the surface and indicated that about 20% of the carbon constituting the nanotubes (MWCNT-K) is bound to oxygen atoms (Figure 3.19). This indicates that not only the reactive tube edges have been modified but also the surface of the outer layer was affected.

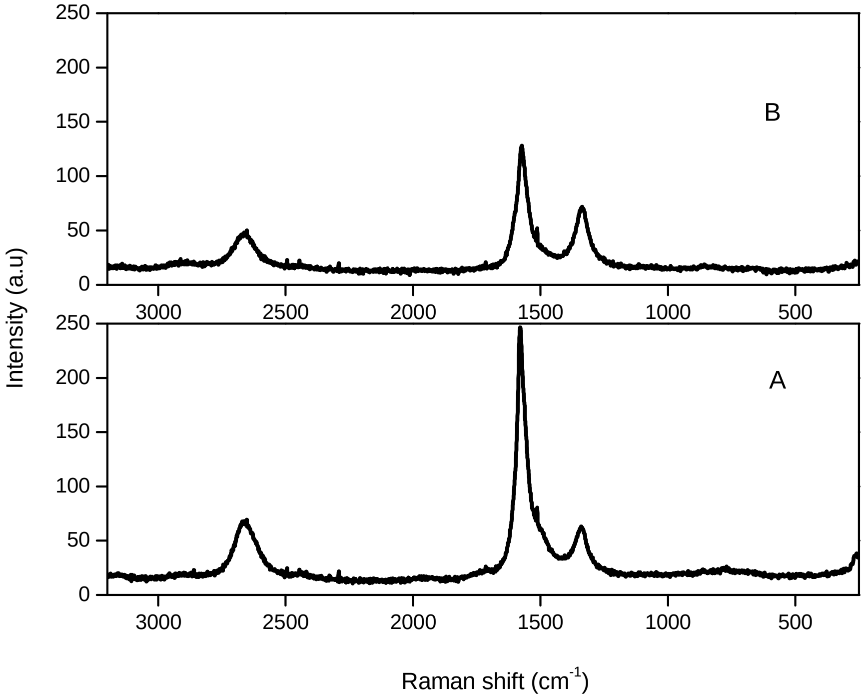

Figure 3.18 Raman spectra of as received MWCNTs (A) and MWCNTs after oxidation with $KMnO_4$ (B).

3.3.4.7 FTIR Spectra of Bare and Oxidized MWCNT

The FTIR spectrum of $KMnO_4$- oxidized sample (MWCNT-K) is shown in Figure 3.20. The $KMnO_4$ treatment has mainly introduced hydroxyl group functionalities as confirmed by the well defined peaks at 3500 and 1150 cm^{-1}. The same iron-mediated galvanostatic polarization experiments (at constant current of 3mA) was carried out for both MWCNT and MWCNT-K samples (after being washed free of $KMnO_4$) to separately elucidate the effect of OH functionalities on both the chemical and electrochemical reactivity of MWCNT. Both samples failed to extend the polarization time to any extent beyond the redox mediator supported time.

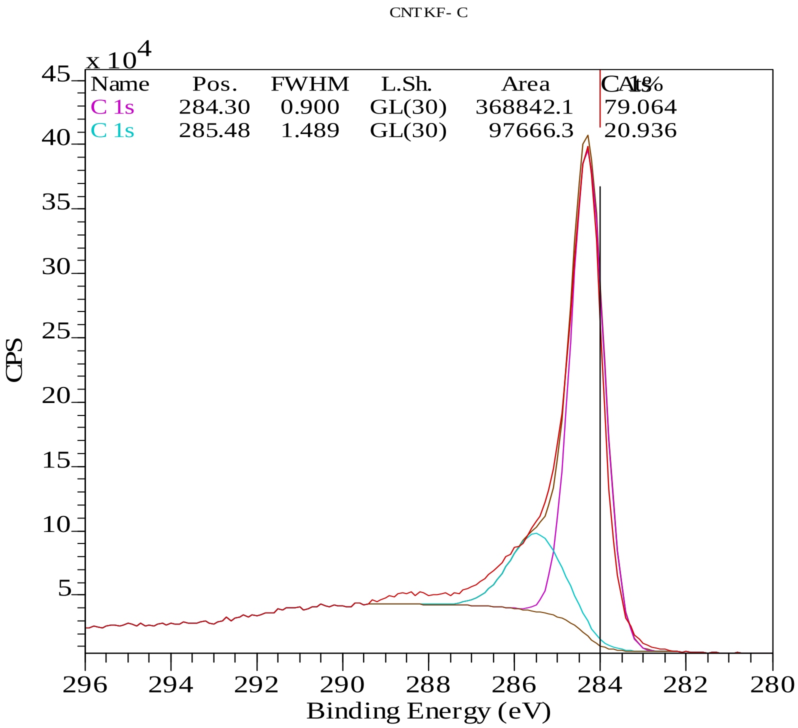

Figure 3.19 Deconvoluted XPS spectrum of MWCNTs after oxidation with $KMnO_4$.

3.4 Conclusion

This study was designed to shed further light on the many factors underlying the reactivity of coal in an electrolytic oxidation environment. The consequences of pre-treatment with strong acids or aq. H_2O_2 on electrochemical and thermal reactivity were probed for this purpose and compared with the corresponding behavior of carbon black. The better performance of low rank coal (TXLC) following pre-treatment, involving acid digestion and oxidation with H_2O_2 can be correlated with the modification of oxygen functional groups on the coal surface as well as the increase in surface area which leads to better accessibility of surface groups to chemical and electrochemical reactions. Nitric acid had a different effect associated with its own redox behavior. Conversely the adverse effect of chemical pre-treatment, specifically H_2O_2 pre-treatment, on the carbon blacks, medium, and high rank coals

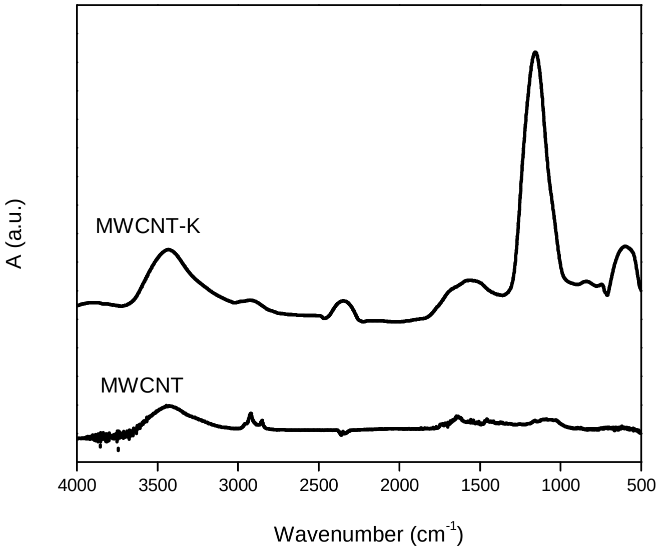

Figure 3.20 FTIR spectrum of MWCNTs before and after oxidation with $KMnO_4$.

was attributed to the lower content of aliphatic structures and higher resistance to oxidation of these samples.

Further investigations on the mechanistic aspects of iron mediated coal electrolysis revealed that the introduction of oxygen functional groups, especially carbonyl groups, on the coal surface selectively improved the chemical reactivity of coal and hence facilitated electron transfer between coal and iron (III) ions. The modification of MWCNT surface with hydroxyl groups following $KMnO_4$ treatment did not result in any improvement in their chemical or electrochemical reactivity in iron-mediated electrolysis and ruled out any significant effect of hydroxyl groups on their reactivity.

CHAPTER 4

ECONOMIC ANALYSIS OF HYDROGEN PRODUCTION BY COAL ELECTROLYSIS

In this part, the commercially applicable techniques for hydrogen production are briefly discussed with emphasis on their economic aspects. Following this, a model allowing the analysis of the economics of hydrogen production by coal (dark and photo) electrolysis is developed. A sensitivity analysis study that addresses the influence of variation of main system components (e.g., electricity price, operating potential and process efficiency) on the hydrogen production cost by electrolysis is then presented. Finally, the cost of hydrogen production according to the proposed model is compared to that of the closely related and commercially applicable hydrogen production technologies, namely, water electrolysis, biomass and coal gasification. The aim is to identify the economic barriers (if any) associated with the commercial application of coal (dark and photo) electrolysis for hydrogen production. The stepwise approach to the economic analysis model is summarized as follows:

I. Designing a process scheme for the production of hydrogen.
II. Determining the optimal hydrogen production through testing various simulation cases.
III. Analyzing the simulation results to determine technical and economic feasibility.

4.1 Hydrogen Production Technologies

Although USA is the 3rd largest oil producer in the world, the amount of imported petroleum is expected to increase to 60% by 2025. Hence, an increasing interest in developing alternative fuels to power our society and to increase energy and economic security is obvious and becomes more critical with the substantial political uncertainty in the world today, particularly in the Middle East. In addition, an increased demand from developing countries (Brazil, India, China) has contributed to the problem and increased the cost of oil substantially in the past few years. Cost is not the only main concern but there are significant environmental concerns with petroleum usage as well.[61]

Hydrogen is expected to play a crucial role as a potential solution to the current concerns with energy supply. In fact, hydrogen was excluded as a solution to the aforementioned concerns when gasoline was priced at 1 $/gallon.[62] As an energy carrier, hydrogen has many advantages. Besides being an inexhaustible resource, hydrogen has zero contribution to environmental pollution. Water vapor is the product of hydrogen combustion and electricity generation in fuel cells. Hydrogen has several production paths summarized in Table 4.1. Two factors play a crucial role in all of these processes. They are namely the cost of the energy input and the efficiency of energy conversion.[63]

Table 4.1 Commercial Processes Currently in Use for Hydrogen Production[61]

Technology	Feedstock	Efficiency
Biomass gasification	Biomass	35-50%[a]
Alkaline electrolyzer	H_2O+ electricity	50-60%[b]
Partial oxidation	Hydrocarbons	60-75%[a]
Steam reforming	Hydrocarbons	70-85%[a]
Biomass gasification	Hydrocarbons	60-65%[c]

[a] Thermal efficiency calculated based on higher heating values (HHV)

[b] Lower heating value(LHV) of hydrogen produced divided by the electrical energy supplied

[c] Dry coal to syngas, LHV, not counting electric input

The majority of hydrogen produced currently depends on non-renewable sources such as oil, natural gas and coal. In other words, fossil fuel based processes are used to produce about 95% of global hydrogen. Only 5% is generated from water using electricity and biomass. Table 4.1 describes the techniques that are commercially used for hydrogen production. Each technique will be discussed in more detail in what follows.

4.1.1 Hydrogen from Biomass

Wood is the oldest form of energy used by mankind. As a biomass energy source, wood has been subjected to direct combustion to release its stored energy. Biomass comprises all the living matter present on earth.[64] Other sources of biomass include algae, trees, agricultural crops and their byproducts, animal manure and food processing waste.[65] The organic matter constituting the majority of biomass consists of carbon, hydrogen, oxygen and nitrogen with the solar energy stored in chemical bonds. Some biomass is composed of an appreciable amount of inorganic species.[66]

Biomass can offer the most efficient renewable substitute to petroleum. Biomass and biomass derived fuels can provide a sustainable pathway for hydrogen production. The net amount of CO_2 released during biomass gasification does not contribute to CO_2 emissions as it was originally absorbed from the atmosphere and fixed by the plants in the photosynthesis process.[65] Biomass can be converted into hydrogen rich gas by two routes, namely, biomass gasification and biochemical/biological conversion. Biomass gasification is a mature process and commercially applicable for hydrogen production.

During this thermal process, biomass is partially oxidized in a pure stream of oxygen at high temperatures, typically 800-900 ℃, and is converted completely into H_2 and CO. Under these conditions, biomass gasification produces large amount of tar in the product gas and Ni based catalysts are needed to reduce tar formation and to upgrade the product gas.[67] An oxygen separation unit is also needed to supply the required amount of pure oxygen for the oxidation process. This unit is too costly especially for small-scale plants. Pure oxygen can be replaced with air as an oxidant but the product gas will be more dilute and contaminated with NO_x. Large scale production can reduce the final cost of hydrogen production but requires massive amounts of feedstock. In all the cases, a gas separation process is necessary to produce a pure stream of hydrogen, which adds to the entire cost of hydrogen production. Biomass gasification can achieve 35-50% efficiency but the cost effectiveness of the process is largely affected by the logistic costs which limit the spread of efficient distributed gasification plants.

The price of hydrogen produced by biomass gasification is almost three times higher than that for hydrogen produced by steam methane reforming (SMR). Although commercially applicable, hydrogen production from biomass still has major challenges. The main challenge is the low yield of hydrogen, as the hydrogen content of the feedstock is low (6 % vs. 25 % for methane). The energy content of the feedstock is low as well due to the high oxygen content (40 wt %) which limits the efficiency of the process.

4.1.2 Hydrogen from water

Splitting water into hydrogen and oxygen has been a hot topic for research for a long time and dates back to the 1890s. There are three main processes that can be used to effect water splitting, namely, electrolysis, thermolysis, and photoelectrolysis.

4.1.2.1 Electrolysis

Electrolysis is the simplest way of splitting water and involves the application of an electric current between two electrodes to break water into its elemental components. The electrical energy is simply converted into chemical energy with efficiencies ranging from 50-60% (Table 4.1). Alkaline electrolyzers are mostly used compared to polymer exchange membrane (PEM) or solid oxide electrolysis (SOEC) cells. They are lower in capital cost and have typical efficiencies of 50-60% based on the lower heating values.

The overall reactions taking place at the cathode and the anode are:

At the anode:

$$4\ OH^- \rightarrow O_2 + 2H_2O$$

At the cathode:

$$2H_2O + 2e \rightarrow H_2 + 2\ OH^-$$

Overall reaction:

$$H_2O \rightarrow H_2 + 2\ OH^-$$

Water is decomposed at the cathode into H_2 and OH^-. OH^- ions travel to the anode where O_2 is formed. The H_2 produced must be separated from the alkaline solution using a gas liquid separator.

Electrolyzers have several advantages for hydrogen production. They are capable of producing hydrogen in high purity. They can be operated under high pressure to eliminate the need for expensive hydrogen compressors and are easily fitted to on-site production to avoid shipping costs. When the energy supply is mechanical (hydropower or wind turbines), or photovoltaic from sunlight, there is virtually no pollution or toxic byproducts, and the feed sources are fully renewable, so the importance of electrolysis is increasing as human population and pollution increase. Electrolysis will become more economically competitive as non-renewable resources (carbon-based compounds) dwindle and as government removes subsidies on carbon-based energies.[68]

4.1.2.2 Photoelectrochemical Water Splitting

Sunlight in presence of semiconductor materials is used to decompose water into hydrogen and oxygen. In photoelectrochemical cells (PECs), a photocathode (p-type semiconductor having excess holes) or a photoanode (n-type semiconductor having excess electrons) is immersed in an aqueous electrolyte to split water into the constituting elements. For a photoanode based system, the process may be described as follows:

1. When a photon with a greater energy than the semiconductor band gap energy (E_g) strikes the photoanode surface, an electron-hole pair is created.
2. The holes are used to decompose water into O_2 and H^+ ions on the photoanode side, while the electrons are used to reduce H^+ ions into H_2 on the cathode side.
3. A semi-permeable membrane is commonly used between the anode and the cathode compartments to keep the two gases separated.

The performance of PECs depends mainly on the photoelectrode material and the semiconductor. Imperfections in the crystalline structure, bulk and surface properties of the photoelectodes usually limits the hydrogen production efficiency. An ideal photoelectrode should be able to resist corrosion caused by aqueous electrolytes and at the same time retain the ability to drive the water decomposition reaction. This ability depends mainly on the perfect matching of the energetic of the electrochemical reaction and the absorbed solar radiation. Improper matching we will mostly lead to corrosion or development of blocking layers on the photoelectrode surface.[69] In general an ideal photoelectrode should have the following characteristics:

1. A band gap that straddle the redox potential of H_2 and O_2 half reactions.
2. Maximum absorption of the solar spectrum.
3. High quantum yield ($>$ 80%) across the absorption band.

The target efficiency of PECs is $>$ 16% solar energy to H_2. Current water splitting photoelectrodes have low efficiency and on-going research is targeting development of electron transfer catalysts and surface enhancements to improve their performance.

4.1.3 Hydrogen from Hydrocarbons

4.1.3.1 Steam Methane Reforming (SMR)

Hydrogen generation from natural gas is the most commonly used method with approximately 80% efficiency[70–72]. This process releases greenhouse gases. Since the production is concentrated in one facility, it is possible to separate the gases and dispose of them properly, for example by injecting them in an oil or gas reservoir.

The steam-methane reforming (SMR) process is illustrated in Figure 4.1.[73] The basic steps leading from the natural gas, to the high purity hydrogen product are:

1. Pretreatment of the raw feedstock:

First, the catalytic nature of the reforming reaction renders it very sensitive to catalyst poisons. The catalysts employed are normally poisoned by even trace amounts of sulfur.[70–72] Hence, for economical operation, sulfur compounds need to be removed through the feedstock pretreatment. Second, reforming is a reaction between methane and steam, so non-methane hydrocarbons must be converted to methane.

2. Reforming to synthesis gas:

Commercial bulk hydrogen is usually produced by the steam reforming of natural gas. At high temperatures (700–1100 ℃), steam (H_2O) reacts with methane (CH_4) to yield syngas.

$$CH_4 + H_2O \rightarrow CO + 3\ H_2$$

Essentially, the oxygen (O) atom is stripped from the water (steam) to oxidize the carbon (C), liberating the hydrogen formerly bound to the carbon and oxygen. The heat required to drive the process is generally supplied by burning some portion of the methane.

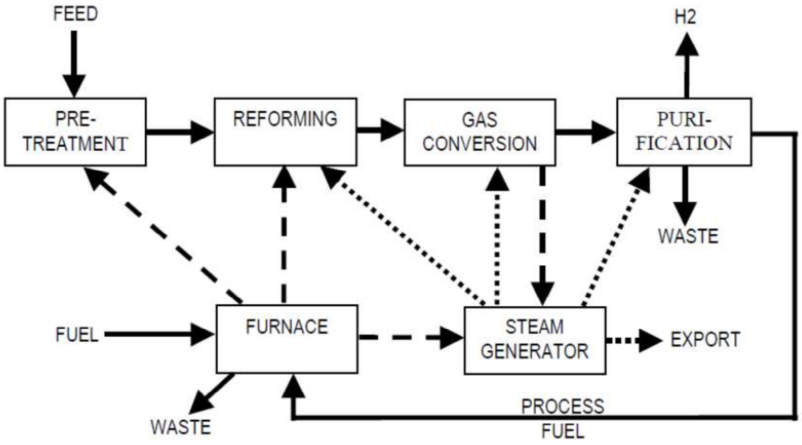

Figure 4.1 Schematic of SMR process.

3. Conversion to a hydrogen-rich gas:

The syngas from the reformer is rich in H_2 and in CO. Additional hydrogen can be recovered from carbon monoxide (CO) through the lower-temperature *water gas shift reaction*:

$$CO + H_2O \rightarrow CO_2 + H_2$$

Low reaction temperatures are favorable to achieve equilibrium, but high temperature is required to achieve a practical reaction rate. This is normally overcome through the use of a two stage shift system.

In the first stage, a high temperature, typically 350 °C, is required. A low cost iron-based catalyst is used to promote the reaction and to reduce the CO concentration to a few percent. In the second stage of shift, a lower temperature (190 - 210 °C) in the presence of a more expensive, copper-based catalyst is used to increase the equilibrium concentration of H_2. at a reasonable rate.

4. Purification to hydrogen product specifications:

The shifted syngas has a high concentration of H_2, but is still contaminated with a high concentration of CO_2 and H_2O, as well as residual methane and small amounts of carbon monoxide and nitrogen. The gas is purified by removal of CO_2, removal of moisture by condensation and drying, and removal of other contaminants in a pressure swing adsorption unit.

At present, SMR dominates the market for hydrogen production and to assess the economics of hydrogen production as currently practiced, a typical facility providing 120,500 kg/d of hydrogen is considered.[73] Different factors such as: the direct capital cost, the prices of natural gas, catalysts and solvents and operating costs are taken into account according to the model. The Total Plant Investment is $82 million. Assuming an availability of 95% and operating with an efficiency of 78%, the cost for the production of H_2 comes to $0.83/kg with 1366 tons CO_2/d emitted Purchase of natural gas accounts for 55% of this price, capital equipment charges, operating and maintenance accounts for 45% of costs. The cost for the production of H_2 with CO_2 capture is increased by 35% and becomes $1.12/kg.

4.1.3.2 Coal Gasification

Coal gasification is a clean coal technology that avoids the conventional coal burning process by converting coal into a gas.[77,78] In this way, sulfur and nitrogen compounds and particulates are removed before the fuel is burned, making it almost equally clean as natural gas. Coal was first used in gas production during the late 18th century. Early production was used primarily for lighting, but as gasification techniques improved, applications grew wider. By the 19th century the conversion of coal to gas was a well-established commercial process. Gasification technology is particularly suitable for low-rank coals because of their higher reactivity for gasification than high-rank coals.[79] Focusing only on the coal carbon content, coal gasification can be represented by the well-known steam carbon reaction:

$$C + H_2O \rightarrow CO + H_2$$

This reaction is strongly endothermic and its equilibrium is highly unfavorable at ordinary temperatures. Coal is gasified in practice by treating it with a mixture containing both steam and oxygen:

$$C + O_2 \rightarrow CO_2$$

In this manner a part of the coal is burnt and the heat released by the combustion reaction provides the thermal energy required by the steam carbon reaction. The detailed chemistry and technology of coal gasification is complex and involve different side reactions such as reactions between CO_2 and coal, between CO and H_2O, and between O_2 and CO. The complex gaseous product from coal gasification must be cleaned to remove impurities such as tars, ash, carbon dioxide, and sulfur compounds. The hydrogen and carbon monoxide contents of this gas are often further adjusted by means of the water-gas shift reaction to provide the required CO/H_2 ratio.

Coal gasification requires extreme conditions of temperature and pressure (>1000 psig and temperatures of 800 °C) which raise process and hydrogen production costs. In addition, the coal gasification process is not completely clean and air contamination by the released CO_x, NO_x, SO_x and Hg should be dealt with.[80]

4.1.3.3 Coal Electrolysis

Coal electrolysis has re-appeared as a possible technology to produce hydrogen due to its advantages of operating at low temperature (<100 °C) and atmospheric pressure. Additionally, a pure stream of H_2 can be obtained, problems with H_2 storage are lacking with distributed production, and products of the process (CO_2 and H_2) are free of tar and sulfur compounds. A literature review of coal electrolysis has been previously discussed at the introductory chapter of this dissertation. Since coal electrolysis as a technological pathway for hydrogen production is not a commercial process and still under development, we present a model below for its economic evaluation. The model will basically depend on the experimental parameters and results from chapters 2 and 3 of this dissertation.

4.2 Coal Electrolysis Economic Analysis Model

4.2.1 Key assumptions in building the model

Using a comprehensive H_2 cost analysis report developed by Center for Transportation Research Energy Systems Division Argonne National Laboratory(ANL)[81] as a starting point, the coal electrolysis model was built. The report provides an analysis of potential hydrogen demand, production and cost by region from 2010 to 2050.In addition to addressing the hydrogen production cost the report also monitors how the hydrogen demand will grow with time and takes into account the relative availability of resources such as coal, natural gas or renewables. Also the likelihood of each resource being used to produce hydrogen is taken into account. Table 4.2 shows the costs of the input energy used for hydrogen production on a national average.

Table 4.2 Prices for the Different Input Energy Sources for Hydrogen Production

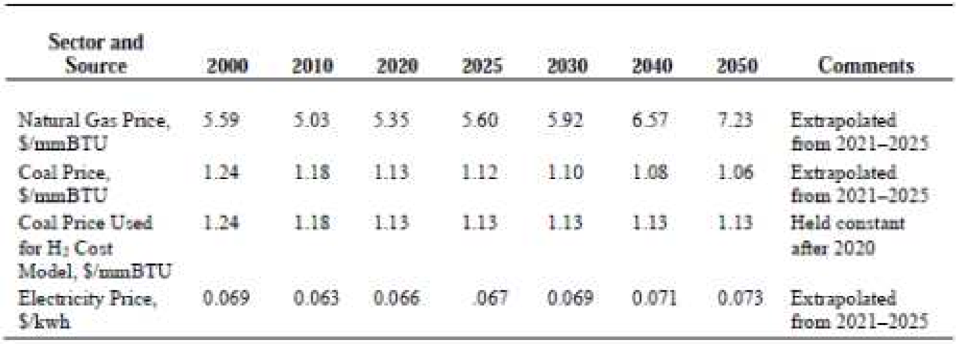

Sector and Source	2000	2010	2020	2025	2030	2040	2050	Comments
Natural Gas Price, \$/mmBTU	5.59	5.03	5.35	5.60	5.92	6.57	7.23	Extrapolated from 2021–2025
Coal Price, \$/mmBTU	1.24	1.18	1.13	1.12	1.10	1.08	1.06	Extrapolated from 2021–2025
Coal Price Used for H_2 Cost Model, \$/mmBTU	1.24	1.18	1.13	1.13	1.13	1.13	1.13	Held constant after 2020
Electricity Price, \$/kwh	0.069	0.063	0.066	.067	0.069	0.071	0.073	Extrapolated from 2021–2025

mm BTU: one million British Thermal Units
1BTU= 1.055 kJ

Coal and electricity prices for 2010 will be used for the cost analysis .The same coal price will be used for both coal electrolysis and coal gasification cost analysis. The electricity used for water as well as coal electrolysis is assumed to be generated from renewable sources. The cost for each centralized production case is based on a capacity of 150,000 kg H_2/day. The coal gasifiers used in the ANL report and with which we are comparing are assumed to operate at 64% efficiency (dry coal to syngas, LHV, not counting electric inputs). The commercialization of H_2 production and distribution systems is known to be highly capital intensive. Therefore, the sensitivity study will be limited to process efficiency and input energy (feedstock) cost. Detailed economic analysis of the coal electrolysis process that covers capital investment, fixed and variable costs and return on investment is beyond the scope of this study. However this preliminary economic analysis will show how the electrolysis process may be used as a competitive technology for hydrogen production.

It is worth mentioning here the coal electrolysis is not a sustainable hydrogen production pathway. Even if it is driven by energy sources that do not contribute to greenhouse gas emissions, it still depends on consuming materials (coal and chemicals) other than water.

4.2.2 Demonstration system description and optimization

4.2.2.1 Dark Electrolysis of Coal

The demonstration setup indicated here (Figure 4.2) is previously described in the beginning of Chapter 2 and 3 of this dissertation. Very few modifications are introduced here to reduce the input energy consumed during the acid pretreatment step. The modification involves the use of solar heat energy to boil the coal acid slurry prior to electrolysis.

A non-concentrating solar collector is assumed to provide sufficient heat energy to cover the specific heat as well as the heat of vaporization of water over the 30 min boiling period.[82] Both the 1 M acid and the catalyst may be filtered off and separated from the coal slurry and reused. The catalyst solution will then contain iron(III) ions only which are known to have a catalytic effect on coal electrolysis.[83] Coal itself may be reactivated by heating at 250 °C and repeatedly reused[5] with minimum contribution to the total cost. Instead of the grid electricity source used during experiments, a renewable electricity source such as solar cells can be used to reduce the contribution of the process to greenhouse gas emissions.

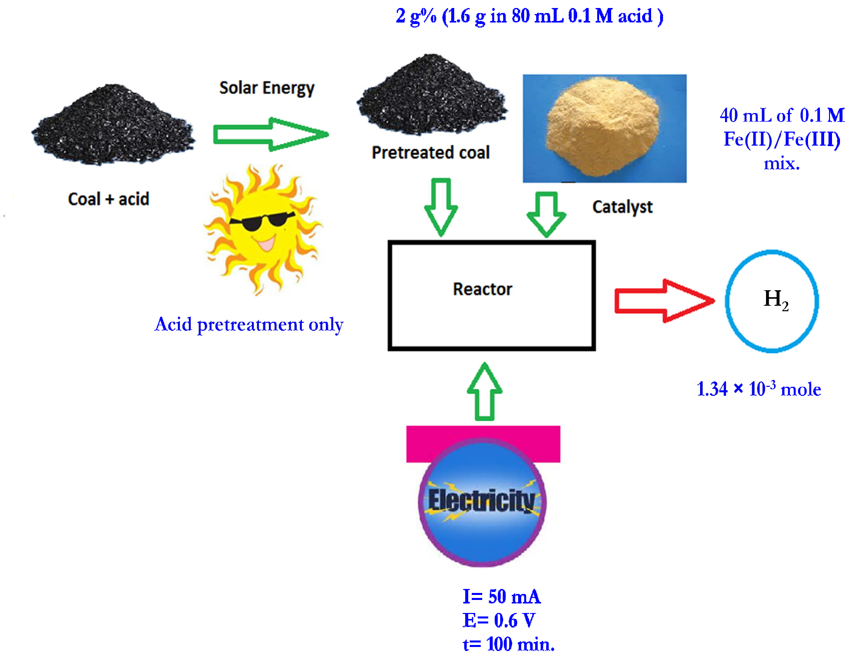

Figure 4.2 Demonstration setup for hydrogen production by dark coal electrolysis.

The price of electricity used in the cost estimates of hydrogen production will adhere to the same prices shown in Table 4.2. An average electrolysis time of 100 min at 50 mA and hydrogen evolution rate of 0.301 mL/min is assumed for the calculations. It is applicable to both acid treatment as well as the hydrogen peroxide pretreatment cases.

4.2.2.2 Photoelectrolysis of Coal

Similar modifications to that explained above for dark coal electrolysis apply here. In addition, the Xe arc lamp used to provide the required UV light will be replaced with a non- concentrating solar collector. This type of collector is specifically used due to its high ability to collect both direct and diffuse sunlight.

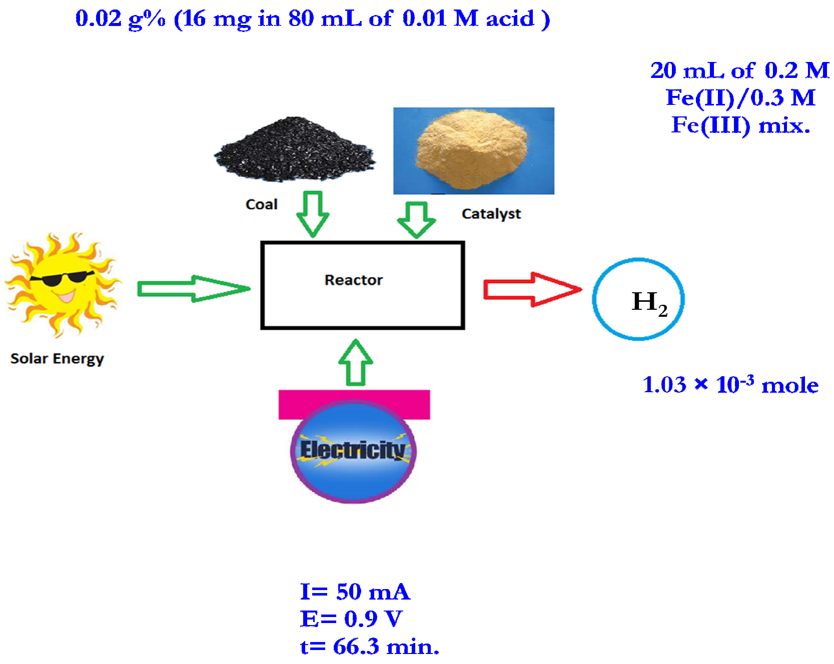

Figure 4.3 Demonstration setup for hydrogen production by coal photoelectrolysis.

4.2.3 Sensitivity study

The cost estimation of hydrogen production was made using currently available experimental data from the previous chapters and mainly based on custom-made assumptions. The sensitivity analysis addresses the influence of variation of main system components (e.g., electricity price, operating potential, and process efficiency) on the hydrogen production cost.

4.2.3.1 Electricity Price

Electricity prices have proven to be the major contributor to the overall hydrogen production cost in all electrolytic hydrogen production technologies such as alkaline water electrolysis.[84] Since the coal electrolysis process depends mainly on using the electric energy and the energy stored in the coal feedstock to produce hydrogen, electricity prices are expected to play a major role in determining the hydrogen production cost. The electricity prices shown in Table 4.2 will be used to calculate the hydrogen production cost in 2010 US dollars assuming 90% and 85% efficiency for the dark and photoelectrolysis processes, respectively. A separate analysis of the effect of the process efficiency on the hydrogen production cost will be given in the following discussion.

Figure 4.4 shows a linear increase in the hydrogen production cost with the electricity price as expected. The lower hydrogen prices with dark electrolysis compared to photoelectrolysis is related to the difference in the process efficiency (90% and 85 % for dark and photoelectrolysis, respectively) which pins the cost at $ 2.40 and 3.60 /kg H_2 for dark and photoelectrolysis respectively.

An overall, compression, storage, and dispensing (CSD) costs are expected to total about $1.90 per kilogram of hydrogen dispensed[85]. This increases the hydrogen production cost to US $ 4.30 and 5.50 per kilogram of hydrogen dispensed for dark and photoelectrolysis, respectively. A slight increase in the electricity price from the currently used value ($ 0.063/kWh) to $ 0.10/kWh would increase the cost to US $ 5.20 and 7.90 per kilogram of hydrogen dispensed for dark and photoelectrolysis, respectively. The cost of electricity then is considered as one of the biggest obstacles for large scale electrolytic hydrogen production. It must be emphasized that the foregoing economic analysis is very approximate.

An overall, compression, storage, and dispensing (CSD) costs are expected to total about $1.90 per kilogram of hydrogen dispensed[85]. This increases the hydrogen production cost to US $ 4.30 and 5.50 per kilogram of hydrogen dispensed for dark and photoelectrolysis, respectively. A slight increase in the electricity price from the currently used value ($ 0.063/kWh) to $ 0.10/kWh would increase the cost to US $ 5.20 and 7.90 per kilogram of hydrogen dispensed for dark and photoelectrolysis, respectively.

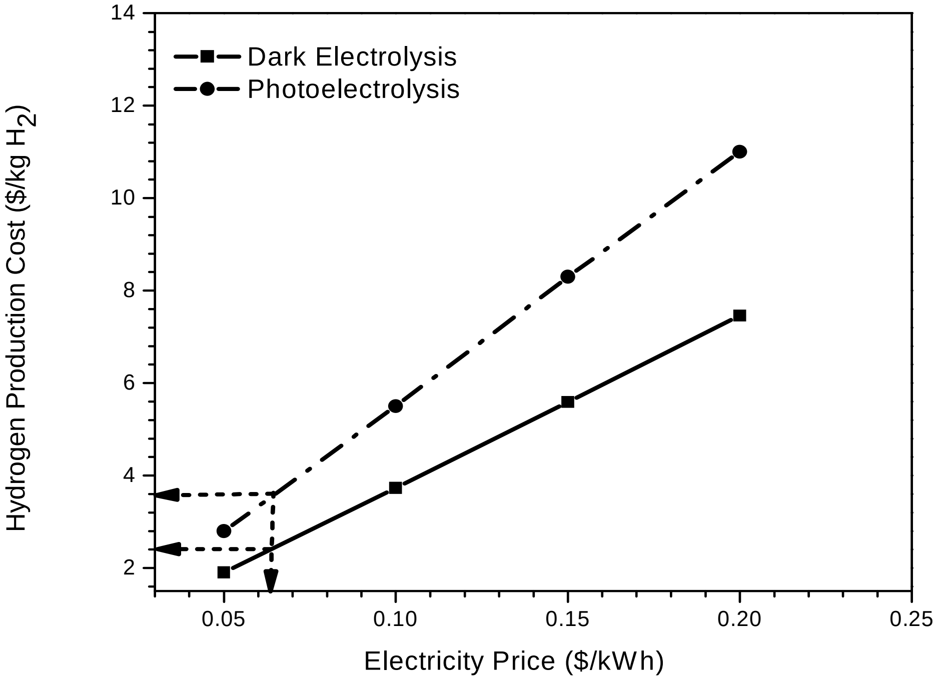

Figure 4.4 Effect of electricity prices on the hydrogen production cost by dark and photoelectrolysis of coal.

The cost of electricity then is considered as one of the biggest obstacles for large scale electrolytic hydrogen production. It must be emphasized that the foregoing economic analysis is very approximate.

4.2.3.2 Cell Voltage

One of the biggest improvement introduced by using coal instead of water as an anode depolarizer in electrolytic hydrogen generation was the reduction of operating cell voltage from 1.7 V to about 0.8 V.[86] The operating cell voltage is dependent upon several factors such as the cell design which directly affects the mass transfer during the process, the catalyst used, the electrolyte and the electrode material. Technological modifications involving the above mentioned factors can result in further reduction in the cell voltage and subsequent improvement of the process efficiency and economics.

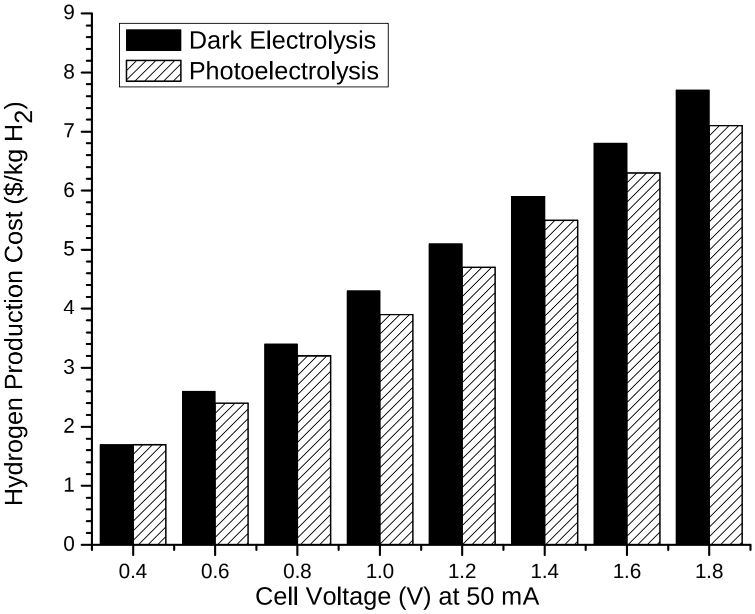

Figure 4.5 Effect of operating cell potential on the hydrogen production cost by dark and photoelectrolysis of coal.

Figure 4.5 shows the effect of operating cell voltage on the hydrogen production cost. The dark electrolysis is still showing more favorable economics as it can be carried out at an operating voltage of 0.6 V compared to 0.9 V for the photoelectrolysis process. The operating cell voltage also affects the energy return over energy input (EROEI) value of the process as shown in Figures 4.6 and 4.7. The energy input is simply calculated from the power supplied all over the electrolysis reaction time and expressed in Wh (Watt. hour) units. The energy output on the other hand is calculated using the number of moles of hydrogen obtained from Faraday's law (assuming 90% and 85% efficiency for the dark and photoelectrolysis reactions, respectively) and the enthalpy of combustion of hydrogen (−286 kJ/mol).The EROEI value was found to be 2.22 and 1.40 for dark and photoelectrolysis, respectively.

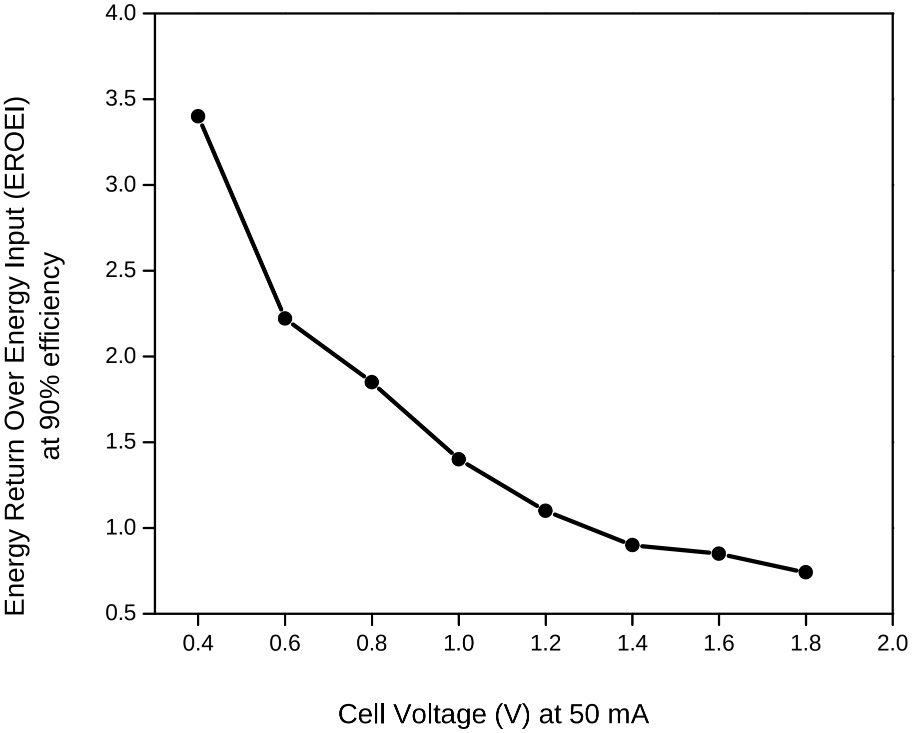

Figure 4.6 Variation of EROEI values with cell voltage during dark coal electrolysis.

Keeping the process efficiency constant and reducing the operating cell voltage from 0.6 to 0.4 V would increase the EROEI value of dark electrolysis to 3.4. Similar exponential increase in the EROEI value of photoelectrolysis to 2.1 can be attained at an operating cell voltage of 0.6 V.

4.2.3.3 Process Efficiency

The efficiency stated here describes the energy efficiency of the process; i.e., the ratio of the process energy output to input. Since the energy inputs shown do not include any energy used upstream of the process, e.g., to extract fossil fuels, to build the cell, or to make the chemicals, the energy efficiency is almost reduced to a Faradaic efficiency. Faradic efficiency describes the efficiency with which the electrons are transferred in a system facilitating an electrochemical reaction.[87] In this coal electrolysis reaction, it is calculated from the ratio of the amount of hydrogen collected to the theoretical amount from Faraday's law.

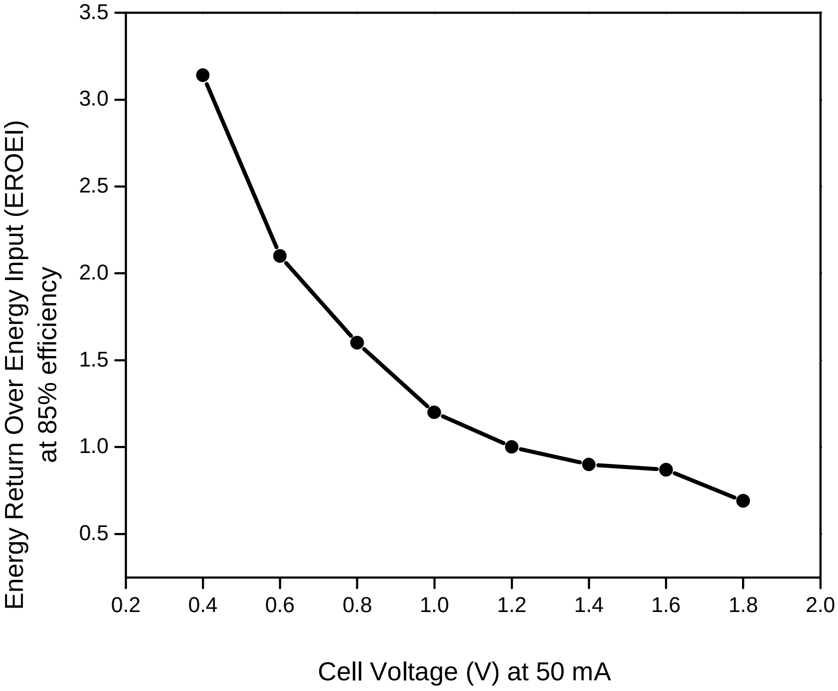

Figure 4.7 Variation of EROEI values with cell voltage during coal photoelectrolysis.

Figure 4.8 shows the reduction in the hydrogen production cost as the process efficiency is improved. The Faradic efficiency may be improved in different ways; e.g., by reducing the overvoltage associated with the limited mass transfer of coal particles and catalyst ions to the electrode surface and reducing the losses during hydrogen collection and measurement. A 10 % increase in the Faradic efficiency (from 90-100% for dark electrolysis) can reduce the hydrogen production cost from US $ 4.50 to 4.30 per kilogram of hydrogen dispensed.

Table 4.3 shows the final distributed cost of hydrogen produced by commercially available technologies in 2010 US $. In principle, coal electrolysis shows favorable economics for hydrogen production although tremendous scale effects should be considered when comparing the cost by different processes. It is clearly evident that the rough economic analysis.

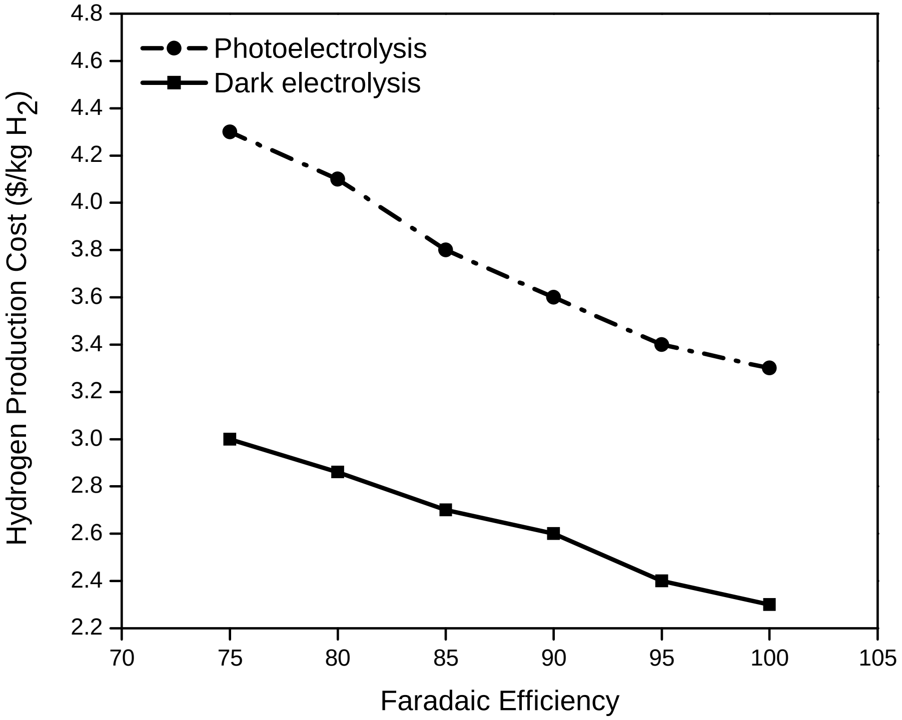

Figure 4.8 Effect of Faradic efficiency on the hydrogen production cost by dark and photoelectrolysis of coal.

Table 4.3 Final Delivered Hydrogen Production Cost by Commercially Available Technologies[81]

Technology	Natural Gas	Water Electrolysis	Coal Gasification	Biomass Gasification	Coal Electrolysis	Coal Photoelectrolysis
Price 2010 US $/GGE*	4.11	12.4	4.60	4.51	4.30	5.50

* Gasoline gas equivalent = 0.997 kg H_2

set above is dependent on large scale production which would keep the electricity costs at the lowest rate. For small or on-site production, coal electrolysis may compete better with the other processes in general as processes such as SMR would become prohibitively expensive on small scale.

4.3 Conclusion

Coal electrolysis will fit well with distributed hydrogen production sites where other commercial processes could prove to be very expensive. The energy requirements as well as the very mild reaction conditions render coal electrolysis applicable to small hydrogen generators in residential areas. In addition, coal electrolyzers can be readily integrated with renewable energy sources. The technical advances expected in the future can result in more reduction of the hydrogen production costs through developing better catalysts, more effective and cheaper electrode materials.

CHAPTER 5

SUMMARY AND CONCLUSIONS

This dissertation study was designed to shed further light on the many factors underlying the reactivity of Texas lignite coal (TXLC) and carbon blacks in an electrolytic oxidation environment and to evaluate the feasibility of this process as a commercial pathway for hydrogen generation.

In the first part of the study, UV light has been used as a mechanistic probe for coal and carbon black photoelectrolysis. The (oxidizable) lignite coal or carbon black particles were able to scavenge (intercept) the free radicals generated by the photo-Fenton-like mechanism before they can oxidize the Fe(II) species to Fe(III) species with a net effect of anodic current enhancement. Factors like the amount of the (oxidizable) carbon content and the surface area of the particles were found to play a crucial role in the reactivity of coal and the two different carbon blacks. The highest plateau current was obtained with SRC-401carbon black sample compared to lignite coal and SRC-159and was rationalized on the basis of both the much higher (oxidizable) carbon content of the black (compared to both coal and SRC-159) and the higher surface area relative to the (low grade) coal. The higher current observed for SRC-401 relative to SRC-159(graphitized) was due to its lower susceptibility toward oxidation as a result of graphitization. By extrapolation, the conclusion is inevitable that surface area differences alone cannot account for the (electron transfer) reactivity differences between the lignite coal and the two carbon black samples.

In the second part, the consequences of pre-treatment with acids or aq. H_2O_2 on electrochemical and thermal reactivity of coal (TXLC) were probed and compared with the corresponding behavior of carbon black. The higher susceptibility of TXLC to oxidation facilitated the modification of oxygen functional groups on the particle surface and increased the surface area. This modification lead to better accessibility of surface groups to chemical and electrochemical reactions and underlined the better TXLC reactivity following both treatments. Conversely the adverse effect of chemical pre-treatment, specifically H_2O_2 pre-treatment, on the carbon blacks, medium, and high rank coals was attributed to the lower content of aliphatic structures and higher resistance to oxidation of these samples. Further investigations on the mechanistic aspects of iron mediated coal electrolysis revealed that the introduction of oxygen functional groups, especially the carbonyl groups, on the coal surface have selectively improved the chemical reactivity of coal and hence facilitates the electron transfer between coal and iron (III) ions. Modification of MWCNT surface with hydroxyl groups following $KMnO_4$ treatment did not result in any improvement in their chemical or electrochemical reactivity in iron-mediated electrolysis and ruled out any effect of hydroxyl groups on their reactivity.

Finally, an economic analysis of hydrogen production by coal (dark and photo) electrolysis was performed. The analysis aimed at carrying out a sensitivity analysis that addresses the influence of variation of main system components (e.g., electricity price, operating voltage and process efficiency) on the hydrogen production cost. Coal electrolysis will fit well with distributed hydrogen production sites where other commercial processes would be very expensive. The energy requirements as wells as the very mild reaction conditions render coal electrolysis applicable to small hydrogen generators in residential areas. In addition, coal electrolyzers can be readily integrated with renewable energy sources. The technical advances expected in the future can result in more reduction of the hydrogen production costs through developing better catalysts, more effective and cheaper electrode materials.

REFERENCES

(1) Cormos, C.-C. *International Journal of Hydrogen Energy* **2011**, *36*, 5960–5971.

(2) Dufour, J.; Serrano, D. P.; Jose, L. G.; Moreno, J.; Gonz, A.; Rey, U.; Carlos, J. *Energy & Fuels* **2011**, 2194–2202.

(3) Coughlin, R. W.; Farooque, M. *Nature* **1979**, *279*, 301–303.

(4) Coughlin, R. W.; Farooque, M. *Industrial & Engineering Chemistry Process Design and Development* **1982**, *21*, 559–564.

(5) Coughlin, R. W.; Farooque, M. *Industrial & Engineering Chemistry Process Design and Development* **1980**, *19*, 211–219.

(6) Clarke, R. L.; Foller, P. C.; Wasson, a. R. *Journal of Applied Electrochemistry* **1988**, *18*, 546–554.

(7) Seehra, M. S.; Ranganathan, S.; Manivannan, A. *Applied Physics Letters* **2007**, *90*, 044104(1–3).

(8) Yin, R.; Ji, X.; Zhang, L.; Lu, S.; Cao, W.; Fan, Q. **2007**, 637–641.

(9) Jin, X.; Botte, G. G. *Journal of Power Sources* **2010**, *195*, 4935–4942.

(10) Clemens, T.; Gong, D.; Pearce, S. *International Journal of Coal Geology* **2006**, *65*, 235–242.

(11) Murphy, O. J.; Bockris, J. O.; Later, D. W. *International Journal of Hydrogen Energy* **1985**, *10*, 453–474.

(12) Farooque, M.; Coughlin, R. W. *Fuel* **1979**, *58*, 705–712.

(13) Dhooge, P. M. *Journal of The Electrochemical Society* **1983**, *130*, 1539–1542.

(14) Park, S.-M. *Journal of The Electrochemical Society* **1984**, *131*, 363C–373C.

(15) Morooka, S.; Murakami, A.; Kusakabe, K.; Kato, Y.; Kusunoki, K. *Fuel* **1984**, *63*, 947–951.

(16) Taylor, N.; Gibson, C.; Bartle, K. D.; Mills, D. G.; Richards, D. G. *Fuel* **1985**, *64*, 415–419.

(17) Okada, G. *Journal of The Electrochemical Society* **1981**, *128*, 2097–2102.

(18) Baldwin, R.; Jones, K.; Joseph, J.; Wong, J. *Fuel* **1981**, *60*, 739–743.

(19) Santos, L. M.; Baldwin, R. P. *Journal of Applied Electrochemistry* **1986**, *16*, 203–212.

(20) Thomas, G.; Chettiar, M.; Birss, V. I. *Journal of Applied Electrochemistry* **1990**, *20*, 941–950.

(21) Demoz, A.; Khulbe, C.; Fairbridge, C.; Petrovic, S. *Journal of Applied Electrochemistry* **2008**, *38*, 845–851.

(22) Thomas, G. *Journal of The Electrochemical Society* **1990**, *137*, 3104–3108.

(23) Li, F.; Fan, L.-S. *Energy & Environmental Science* **2008**, *1*, 248–267.

(24) Navarro, R. M.; Sanchez-Sanchez, M. C.; Alvarez-Galvan, M. C.; Valle, F. del; Fierro, J. L. G. *Energy & Environmental Science* **2009**, *2*, 35–54.

(25) Levine, D. G.; Schlosberg, R. H.; Silbernagel, B. G. *Proceedings of the National Academy of Sciences* **1982**, *79*, 3365–3370.

(26) Whitehurst D, D. In *Organic Chemistry of Coal*; American Chemical Society, 1978; Vol. 71, pp. 1–35.

(27) Types of Coal http://www.ket.org/trips/coal/agsmm/agsmmtypes.html (accessed Aug 28, 2012).

(28) Haenel, M. W. *Fuel* **1992**, *71*, 1211–1223.

(29) Demoz, a.; Khulbe, C.; Fairbridge, C.; Petrovic, S. *Journal of Applied Electrochemistry* **2008**, *38*, 845–851.

(30) Dhooge, P. M., Park, S.-M. *Journal of The Electrochemical Society* **1983**, *130*, 1029–1036.

(31) Bott, A. W. *Current Separations* **2000**, *4*, 125–127.

(32) Hatakeyama, T.; Quinn, F. X. *Thermal Analysis: Fundamentals and Applications to Polymer Science*; John Wiley & Sons, Inc., 1999.

(33) Stuart, B. H. *Infrared Spectroscopy: Fundamentals and Applications*; David J. Ando, Ed.; John Wiley & Sons, Ltd, 2004.

(34) Smith, E.; Dent, G. *Modern Raman Spectroscopy - A Practical Approach*; John Wiley & Sons, Ltd, 2004; Vol. 5.

(35) Datsyuk, V.; Kalyva, M.; Papagelis, K.; Parthenios, J.; Tasis, D.; Siokou, A.; Kallitsis, I.; Galiotis, C. *Carbon* **2008**, *46*, 833–840.

(36) Osswald, S.; Havel, M.; Gogotsi, Y. *Journal of Raman Spectroscopy* **2007**, *38*, 728–736.

(37) Musfeldt, J. L. *Handbook of Applied Solid State Spectroscopy*; Vij, D. R., Ed.; Springer, 2007; Vol. 129.

(38) Neyens, E.; Baeyens, J. *Journal of Hazardous Materials* **2003**, *98*, 33–50.

(39) Venkatadri, R.; Peters, R. W. *Hazardous Waste and Hazardous Materials* **1993**, *10*, 107–149.

(40) Walling, C. *Accounts of Chemical Research* **1975**, *8*, 125–131.

(41) Faust, B. C.; Hoigné, J. *Atmospheric Environment. Part A. General Topics* **1990**, *24*, 79–89.

(42) Kawai, T.; Sakata, T. *Nature* **1979**, *282*, 283–284.

(43) Sato, S.; White, J. M. *The Journal of Physical Chemistry* **1981**, *85*, 336–341.

(44) Sato, S.; White, J. M. *Journal of the American Chemical Society* **1980**, *102*, 7206–7210.

(45) Chen, X.; Rajeshwar, K.; Timmons, R. B.; Chen, J.-J.; Chyan, O. M. R. *Chemistry of Materials* **1996**, *8*, 1067–1077.

(46) Sathe, N.; Botte, G. G. *Journal of Power Sources* **2006**, *161*, 513–523.

(47) G.Thomas, M Chettiar, V. I. B. *Journal of Applied Electrochemistry* **1990**, *20*, 941–950.

(48) Johnson, K. E.; Verdet, L. *Canadian Journal of Chemistry* **1986**, *64*, 419–423.

(49) Soler, L.; Macanas, J.; Munoz, M.; Casado, J. *International Journal of Hydrogen Energy* **2006**, *31*, 129–139.

(50) Aboushabana, M.; De Tacconi, N. R.; Rajeshwar, K. *Electrochemical and Solid-State Letters* **2011**, *14*, E31–E33.

(51) Okada, G. *Journal of The Electrochemical Society* **1981**, *128*, 2097.

(52) Alcañiz-Monge, J.; Pérez-Cadenas, M.; Lozano-Castelló, D. *Energy & Fuels* **2010**, *24*, 3385–3393.

(53) Kreysa, G.; Kochanek, W. *Nature* **1985**, *316*, 714–716.

(54) Thomas, G.; Whitcombe, S.; Farebrother, M. D.; Birss, V. I. *Journal of The Electrochemical Society* **1990**, *137*, 3104–3108.

(55) Anthony, K. E.; Linge, H. G. *Journal of The Electrochemical Society* **1983**, *130*, 2217–2219.

(56) Aboushabana, M.; De Tacconi, N. R.; Rajeshwar, K. *Journal of The Electrochemical Society* **2012**, *159*, B695–B701.

(57) Zhang, N.; Xie, J.; Varadan, V. K. *Smart Mater. Struct.* **2002**, *11*, 962–965.

(58) Park, S. *Journal of The Electrochemical Society* **1984**, *131*, 363–373.

(59) McCreery, R. L. *Chemical Reviews* **2008**, *108*, 2646–2687.

(60) Kim, U. J.; Furtado, C. A.; Liu, X.; Chen, G.; Eklund, P. C. *Journal of the American Chemical Society* **2005**, *127*, 15437–15445.

(61) Holladay, J. D.; Hu, J.; King, D. L.; Wang, Y. *Catalysis Today* **2009**, *139*, 244–260.

(62) Bockris, J. O.; Veziroglu, T. N. *International Journal of Hydrogen Energy* **2007**, *32*, 1605–1610.

(63) Monteverde, M.; Magistri, L. *International Journal of Hydrogen Energy* **2012**, *37*, 5452–5460.

(64) Kalinci, Y.; Hepbasli, A.; Dincer, I. *International Journal of Hydrogen Energy* **2009**, *34*, 8799–8817.

(65) Balat, H.; Kırtay, E. *International Journal of Hydrogen Energy* **2010**, *35*, 7416–7426.

(66) Boyle, G. *Renewable Energy: Power for a Sustainable Future*; Oxford University Press, USA.

(67) Asadullah, M.; Ito, S.; Kunimori, K.; Yamada, M.; Tomishige, K. *Environmental Science & Technology* **2002**, *36*, 4476–4481.

(68) Koroneos, C.; Dompros, A.; Roumbas, G.; Moussiopoulos, N. *International Journal of Hydrogen Energy* **2004**, *29*, 1443–1450.

(69) Minggu, L. J.; Wan Daud, W. R.; Kassim, M. B. *International Journal of Hydrogen Energy* **2010**, *35*, 5233–5244.

(70) Achenbach, E.; Riensche, E. *Journal of Power Sources* **1994**, *52*, 283–288.

(71) Arzamendi, G.; Diéguez, P. M.; Montes, M.; Odriozola, J. A.; Sousa-Aguiar, E. F.; Gandía, L. M. *Chemical Engineering Journal* **2009**, *154*, 168–173.

(72) Hou, K.; Hughes, R. *Chemical Engineering Journal* **2001**, *82*, 311–328.

(73) Molburg, J. C.; Doctor, R. D. *Hydrogen from Steam-Methane Reforming with CO2 Capture*; Argonne National Laboratory, 2003.

(74) Zhai, X.; Ding, S.; Liu, Z.; Jin, Y.; Cheng, Y. *International Journal of Hydrogen Energy* **2011**, *36*, 482–489.

(75) Maluf, S. S.; Assaf, E. M. *Fuel* **2009**, *88*, 1547–1553.

(76) Kim, H.-W.; Kang, K.-M.; Kwak, H.-Y.; Kim, J. H. *Chemical Engineering Journal* **2011**, *168*, 775–783.

(77) Bhutto, A. W.; Bazmi, A. A.; Zahedi, G. *Progress in Energy and Combustion Science* **2013**, *39*, 189–214.

(78) Öztürk, M.; Özek, N.; Yüksel, Y. E. *Energy Conversion and Management* **2012**, *56*, 157–165.

(79) Kajitani, S.; Tay, H.-L.; Zhang, S.; Li, C.-Z. *Fuel* **2013**, *103*, 7–13.

(80) De Abreu, Y.; Patil, P.; Marquez, A. I.; Botte, G. G. *Fuel* **2007**, *86*, 573–584.

(81) Singh, M.; Moore, J.; William, S. *Hydrogen Demand , Production and Cost by Region to 2050*; Center for Transportation Research Energy Systems Division Argonne National Laboratory and TA Engineering, Inc., 2005.

(82) Parra, S. Malato, S., Blanco, J., Péringer, P. and Pulgarin, C. *Water Science & Technology* **2001**, *44*, 219–227.

(83) Jin, X.; Botte, G. G. *Journal of Power Sources* **2007**, *171*, 826–834.

(84) Yilmaz, C.; Kanoglu, M.; Bolatturk, A.; Gadalla, M. *International Journal of Hydrogen Energy* **2012**, *37*, 2058–2069.

(85) Ramsden, T.; Steward, D.; Zuboy, J. *Analyzing the Levelized Cost of Centralized and Distributed Hydrogen Production Using the H2A Production Model*; National Renewable Energy laboratory, NREL/TP-560-46267, 2005.

(86) Patil, P.; De Abreu, Y.; Botte, G. G. *Journal of Power Sources* **2006**, *158*, 368–377.

(87) Kaneco, S.; Iiba, K.; Hiei, N.; Ohta, K.; Mizuno, T.; Suzuki, T. *Electrochimica Acta* **1999**, *44*, 4701–4706.

BIOGRAPHICAL INFORMATION

Moustafa Reda Aboushabana received his Ph.D in Chemistry and Biochemistry from The University of Texas at Arlington in December 2012. He obtained his Master of Science (with specialization in Pharmaceutical Analytical Chemistry) degree from Mansoura University, Mansoura, Egypt in November 2005, and Bachelor of Pharmaceutical Sciences degree from Mansoura University, Mansoura, Egypt in May 1997.